UC San Diego

UC San Diego Electronic Theses and Dissertations

Title

Correlations as causation : optical properties of strongly correlated matter

Permalink

https://escholarship.org/uc/item/00x2m38h

Author

Schafgans, Alexander Anthony

Publication Date

2011

Peer reviewed|Thesis/dissertation

eScholarship.org Powered by the California Digital Library
University of California

UNIVERSITY OF CALIFORNIA, SAN DIEGO

Correlations as Causation:
Optical Properties of Strongly Correlated Matter

A dissertation submitted in partial satisfaction of the
requirements for the degree
Doctor of Philosophy

in

Physics

by

Alexander Anthony Schafgans

Committee in charge:

Professor Dimitri Basov, Chair
Professor Prabhakar Bandaru
Professor Jorge Hirsch
Professor Clifford Kubiak
Professor Congjun Wu

2011

Copyright
Alexander Anthony Schafgans, 2011
All rights reserved.

The dissertation of Alexander Anthony Schafgans is approved, and it is acceptable in quality and form for publication on microfilm and electronically:

_____

_____

_____

_____

_____

Chair

University of California, San Diego

2011

DEDICATION

To my parents. All of them.

EPIGRAPH

Any good poet, in our age at least, must begin with the scientific view of the world;
and any scientist worth listening to must be something of a poet,
must possess the ability to communicate to the rest of us
his sense of love and wonder at what his work discovers.
—Edward Paul Abbey

TABLE OF CONTENTS

Signature Page iii

Dedication iv

Epigraph v

Table of Contents vi

List of Figures viii

List of Tables xiv

Acknowledgements xv

Vita and Publications xvii

Abstract of the Dissertation xix

Chapter 1 Introduction 1

Chapter 2 Towards a two-dimensional superconducting state of $La_{2-x}Sr_xCuO_4$ in a moderate external magnetic field 10
2.1 Introduction 10
2.2 Experiment 11
2.3 Theoretical Modeling and Discussion 15
2.4 Acknowledgements 18

Chapter 3 Breakdown of the universal Josephson relation in spin ordered cuprate superconductors 20
3.1 Introduction 20
3.2 Experiment 21
3.3 Breakdown of the Josephson relation 24
3.4 Acknowledgements 29

Chapter 4 Electronic correlations and unconventional spectral weight transfer in $BaFe_{2-x}Co_xAs_2$ 30
4.1 Introduction 30
4.2 Determination of electronic correlations 31
4.3 Spectral weight transfer 36
4.4 Appendix 40
4.4.1 Samples and Experiment 40
4.4.2 Determination of kinetic energy 44

4.4.3 Spectral weight transfer in the cuprates 47
4.4.4 Comparison with *ARPES* 48
4.5 Acknowledgements 49

Chapter 5 Phonon splitting and anomalous enhancement of infrared-active modes in $BaFe_2As_2$ 50
5.1 Introduction 50
5.2 Experiment 51
5.3 Phonon asymmetry and the Fano model 56
5.4 Phonon enhancement due to Hund's coupling 56
5.5 Acknowledgements 58

Chapter 6 Landau levels in the three dimensional topological insulator $Bi_{1-x}Sb_x$ 59
6.1 Introduction 59
6.2 Zero-field results 60
6.2.1 Loss function and inhomogeneity 62
6.2.2 Location and size of Fermi Surface 64
6.3 In-field reflectance data and modeling 66
6.4 dR/dH contours and observed Landau levels 69
6.5 Landau levels in magnetic field 71
6.6 Discussion 76
6.7 Acknowledgements 80

LIST OF FIGURES

Figure 1.1: Graphical representation of the text in chapter 2. The relative size of the word correlates with the frequency of word use in chapter 2. 2
Figure 1.2: Graphical representation of the text in chapter 3. The relative size of the word correlates with the frequency of word use in chapter 3. 3
Figure 1.3: Graphical representation of the text in chapter 4. The relative size of the word correlates with the frequency of word use in chapter 4. 5
Figure 1.4: Graphical representation of the text in chapter 5. The relative size of the word correlates with the frequency of word use in chapter 5. 7
Figure 1.5: Graphical representation of the text in chapter 6. The relative size of the word correlates with the frequency of word use in chapter 5. 9

Figure 2.1: (a) Far-infrared reflectance of x=0.1 La214 showing the evolution of the JPR at T=8 K in magnetic field. By 8 T, the reflectance is restored to the normal state value within the signal to noise of our experiment. The JPR is the only feature in the spectra that is sensitive to the field. Dashed lines are extrapolations. Inset: the superconducting phase diagram of La214 for various Sr content. (b) Loss function at T=8 K for x=0.1 La214, further described in Fig. 2. (c) Superconducting phase diagram for La214 x=0.1, showing the decoupling field $H_D(T)$ (red circles) with magneto-resistance data reproduced from Ref.(12); white circles show the solid-to-liquid vortex phase transition, thick white line (our emphasis) is a constant contour of resistivity near the T_c value. Josephson coupling vanishes with increasing field in the green region, the width determined by the uncertainty in H_D. This region signifies the crossover from 3D to 2D superconductivity. 13

Figure 2.2: Field dependence of the normalized loss function ($-Im[1/\epsilon(\omega)]/-Im[1/\epsilon(\omega_{p0})]$) for the four dopings studied at T=8 K. Thick lines are range of extrapolation independent results. Insets: Normalized superfluid density $\rho_s(H,T)/\rho_{s0}(T)$ vs. applied field at T=8 K. Solid black lines represent the VW model predictions (eqn. 2.2), and become a dashed guide to the eye at the vortex solid-to-liquid phase transition. Horizontal grey line is the minimum in Josephson coupling allowed by the VW model while values in the grey hashed region are not allowed. In the x=0.1 and 0.125 insets, the blue line is of the form in eqn. 2.6 with A = 1, 1.6 for x= 0.1 and 0.125, respectively. The size of the superfluid data points represents the uncertainty due to the form of the low frequency extrapolations. The VW model predicts decoupling fields for x=0.1, 0.125, 0.15, 0.17 of $H_w(T)$=9.6T, 9.1T, 21 T and 34 T. 15

Figure 3.1: *Bottom*: The universal Josephson relation for the interlayer response of cuprate high T_c superconductors $\rho_s^c \propto \sigma_{DC}^c(T_c)$ (grey line). This relation breaks down as the result of applied field (LSCO, points A-D) and doping (Nd-LSCO, points 1-5 and LBCO, points $\alpha - \gamma$). The grey box at the bottom displays the lower limit of detectable superfluid density utilizing infrared optical techniques. *Inset*: Schematic of the normal state conductivity at T_c (green curve) and the superconducting state conductivity (blue curve). The orange hashed region represents the spectral weight that is transferred from finite frequencies into a dissipationless superconducting delta peak (orange arrow) at zero frequency. In materials with weakly frequency dependent normal state conductivities, the DC conductivity provides an accurate estimate of the superfluid density. *Top*: The in-plane universal relation holds in the samples where the c axis Josephson relation breaks down. 22

Figure 3.2: Evolution of the Josephson plasma resonance with applied field and doping in a series of La-based single crystals. All data were taken at T=8 K, except where specified. The Nd-LSCO data are replotted from (4), however we measured the x=0.15 LSCO T_c curve on a separate crystal, shown here for reference. LBCO spectra shown for three dopings, demonstrating the absence of c axis coherence in the x = 0.125 sample. Insets: Normalized c axis superfluid density as a function of applied field and Nd-content. 23

Figure 3.3: Phase diagrams showing magnetic field and doping induced loss of interlayer Josephson coupling, in a number of La214 based materials. Here, the green regions labeled 3D represent parameter space of bulk superconductivity with prominent interlayer Josephson coupling. The yellow 2D regions represent the loss of interlayer Josephson coupling while in-plane superconductivity remains. In Fig. 3.3a, the black line is a constant contour of magneto-resistance near the T_c value (12) and the blue region represents error of the measured decoupling field. In Fig. 3.3c, the spin-stripe ordering transition temperature T_{spin}=40K (grey region) proceeds a Kosterlitz-Thouless transition to two-dimentional superconductivity T_{KT}=16K (hashed bar), where the anisotropy of c axis to ab plane resistivity becomes infinite, within experimental uncertainty. At $T_{3D} \approx 4$ K (yellow region) there is the existence of a bulk Meissner state, while Josephson coupling has not been observed. 26

Figure 4.1: Real part of the optical conductivity σ_1 in Ba122 (Top) in the PM ($T = 150K$) and SDW ($T = 50K$) state and Co-Ba122 (Bottom) in the PM normal state and superconducting state ($T = 7K$). For Ba122, we illustrate the necessary integration cutoffs Ω = 777, 969, and 2000 cm^{-1} in order to recover the predicted LDA, LDA+DMFT, and experimentally observed PM state kinetic energy values, respectively. The third cutoff demonstrates that the spectral weight transfer due to the SDW gaps extends to 2000 cm^{-1} and not above. 32

Figure 4.2: Panels A-C: The kinetic energy ratio $K_{exp}(\Omega)/K_{LDA}$ in Ba122 and Co-Ba122, as a function of integration cutoff value Ω (Eq. 1). The ratio for Ba122 in the PM (panel a) and SDW (panel b) states, and for Co-Ba122 in the normal PM state (panel c). The numbers and arrows indicate the results of the four methods for determining the kinetic energy integration cutoff, described in the Appendix. Panel D: The temperature averaged results of the kinetic energy ratio $K_{exp}(\Omega)/K_{theory}$ in the PM and SDW states, compared with both LDA and LDA+DMFT results, including the theoretical kinetic energy values. The triangles show the value of the ratio of the two theoretical kinetic energies determined via LDA and LDA+DMFT in the PM and SDW state. The values from theory are: K^{PM}_{LDA}= (21133 cm-1)^2, K^{SDW}_{LDA}= (6937 cm-1)^2, K^{PM}_{DMFT}= (12905 cm-1)^2, and K^{SDW}_{DMFT}= (8147 cm-1)^2. 35

Figure 4.3: Ratio of the integrated conductivity $K_{exp}(T,\Omega)/K_{exp}(295K,\Omega)$ as a function of cutoff value Ω and temperature over the entire measured frequency range in Ba122 (top panel) and Co-Ba122 (bottom panel). The ratios are taken with respect to the $T = 295$K data in order to display the temperature evolution of the PM and SDW SW transfer. The two vertical dashed bars show the energy scale below which all of the SW transfer takes place, for both the PM and SDW states. The energy scale of SW transfer in the PM state is ≈ 8000 cm^{-1} and in the SDW state is ≈ 2000 cm^{-1}. Inset: Temperature dependence of the kinetic energy of the Drude response, normalized to the room temperature value, at a cut-off Ω=1450cm^{-1}. 37

Figure 4.4: Temperature dependent reflectance of the parent compound $BaFe_2As_2$ (top panel) and the x=0.16 Co-doped superconducting compound $BaFe_{1.84}Co_{0.16}As_2$ (bottom panel). Also shown are fits to the data using the Hagen-Rubens relation for reflectivity in metals (Eq. 4.2). Insets: Reflectance extending to $\approx 45,000$ cm^{-1}, the form above $\approx 12,000$ cm^{-1} is calculated from ellipsometry. 41

Figure 4.5: Real and imaginary parts of the optical conductivity $\sigma_1(\omega)$ (top panel) and $\sigma_2(\omega)$ (bottom panel), respectively. Two representative temperatures are shown in the parent compound Ba122 to exemplify the differences between the PM and SDW states. The SDW gaps were determined by measuring the local minima in $\sigma_2(\omega)$, shown here with vertical bars. 43

Figure 4.6: Real part of the optical conductivity σ_1 at $T = 23$K in Co-Ba122 with the modeled interband contribution. The IB model was subtracted from the σ_1 data in order to determine σ_1 due solely to the Drude response. 46

Figure 5.1: Temperature dependence of the real part of the optical conductivity $\sigma_1(\omega)$ in Ba122, focused on the far-infrared frequency range. 52

Figure 5.2: The real part of the optical conductivity $\sigma_1(\omega)$, focusing on the phonon modes in Ba122 near 95 cm^{-1} (Ba-Ba, panel a) and 257 cm^{-1} (Fe-As, panels b and c). We observe both phonon modes to split upon the transition from the HTT to LTO phases. Panels a and b show Lorenzian fits to the data, while panel c shows fits of the Fano form (Eq. 5.1) to the phonon at 257 cm^{-1}. The fit parameters are shown graphically in panel d (oscillator frequency position, ω_0) and panel e (oscillator strength, ω_p). Table 5.1 summarizes the results of our fits. 53

Figure 5.3: Temperature evolution of the 257 cm^{-1} phonon mode in Ba122. We find this mode to evolve monotonically with temperature and to be just above the noise floor of our measurement for temperatures at 200K and below. 57

Figure 6.1: **Top**. Reflectance vs. wavenumber in the far-infrared as a function of temperature, showing the Drude plasma frequency. The screened plasma frequency $\tilde{\omega_p}(10K)$ is shown with an arrow. **Bottom**. The real part of the optical conductivity $\sigma_1(\omega)$ as a function of temperature, illustrating the decreasing Drude response at lowered temperature. The optical gap $E_g + 2E_f$ is shown with an arrow, and the conductivity rapidly increases at frequencies above the optical gap. **Bottom, inset**. The Drude plasma frequency $\omega_p(T)$ obtained from modeling the Drude response (see SM). The strong temperature dependence of $\omega_p(T)$ is likely the consequence of thermal activation. 61

Figure 6.2: The loss function $\mathrm{Im}[1/\tilde{\epsilon}(\omega)]$ normalized to the value at the screened plasma frequency $\tilde{\omega}_p$. 63

Figure 6.3: A cartoon showing the bulk L bands, the Fermi energy E_f defined from the bottom of the conduction band, the surface states formed when the surface Dirac bands cross E_f, and the necessary photon energy $E_g + 2E_f$ to create an interband transition. 65

Figure 6.4: Reflectance vs. wavenumber and applied field H || C1 || k, at T = 10K (top) and 100K (bottom). Each curve represents 0.1T increment in applied field, going from 0-3T at 10K and 0-2T at 100K. 67

Figure 6.5: Reflectance at T=10K in 0.1T increments, overlaid with the corresponding model (red line) from RefFIT. The arrow illustrates the value of the largest resonance observed in the raw reflectance. 68

Figure 6.6: dR/dH surface contour showing the relative intensity of the LL transitions observed. The larger the feature in the dR/dH spectra, the larger the spectral weight involved in the LL. 70

Figure 6.7: dR/dH contour illustrating the three CR modes extracted from fitting the field dependent reflectivity. The white circles correspond to the largest CR mode (as illustrated by the arrow in Fig. 6.5). The black circles show two additional modes that were converged upon by the fitting routine. The one higher in frequency likely also corresponds to the bulk CR mode, while the one lowest in energy behaves anomalously. 72

Figure 6.8: Contour plots showing the derivative of the reflectance with respect to magnetic field, dR/dH, at T = 10K (top) and 100K (bottom). LLs show up as peaks that disperse to higher wavenumber with applied field. 73
Figure 6.9: Single particle LLs as a function of frequency for the bulk (top) and SSs (bottom). The green horizontal line illustrates the location of the Fermi energy with respect to the single particle LLs (E_f= 45 cm^{-1}). The bulk LLs are spin-split, with the size of splitting determined primarily by the strength of spin-orbit coupling, which bears on the value of g_0. The red (blue) lines are spin up (down) LLs. Values used to determine the LLs are, for the bulk states: m_c=0.0073m_e, E_g=385 cm^{-1}, g_0=0.5/m_c. For the SSs, we used: m=1, g_s=80, v_f=8.5x10^5 m/s. 75
Figure 6.10: Theoretical LL transitions of the form in eq.6.2 overlaid on the data at 10K. We have included three different Fermi velocities in order to explain all of the observed LLs. As labeled, v_f^1 = 8.5x10^{5}m/s, v_f^2 = 6x10^{5}m/s and v_f^3 = 5x10^{5}m/s and the 0-1 (blue lines), 1-2:2-1 (black lines), and 2-3:3-2 (red lines) transitions are given. We did not correct for the Drude effective mass (m=1) and used a very moderate g-factor of the surface states (g_s=120). 78
Figure 6.11: The theoretical magnetic field dependence, plotted as a dR/dH contour, of a plasma edge of a metallic semi-conductor similar to what we observe in $Bi_{1-x}Sb_x$. The quantitative similarity with the data is suggestive. 79

LIST OF TABLES

Table 2.1: Superfluid density measured for $x = 0.1$ La214 at $T = 8$ K, with experimentally established upper/lower bounds for in-field suppression 14

Table 4.1: ω_p values used for Figure 4.2 of the main text, with the corresponding method we employed. ω_p under labels 1, 2, and 4 were determined by integrating the optical conductivity up to listed cut-off value, while values under label 3 were determined by subtracting the IB model from the optical conductivity and integrating the remaining spectra. 45

Table 4.2: Lorentzian oscillator parameters used to create the IB models shown in Fig. 4.6. All units in cm^{-1}. 47

Table 5.1: The oscillator position ω_0, oscillator strength ω_p, and oscillator width Γ, based on the models used to fit the optical spectra. The error for each fit value is listed in parentheses. For the Fano oscillators, the Fano parameter is listed in Figure 5.2c. 54

ACKNOWLEDGEMENTS

This work would not have been possible without the wisdom and guidance from my advisor, Dimitri Basov. It is from his example and with his direction that I, today, am a physicist.

I am indebted to the camaraderie and insight of my fellow lab-mates and colleagues. The landscape of my graduate career was formed by our countless discussions at the coffee cart, seemingly endless experiments, struggles through datasets, and adventures at conferences.

My close friends and family have provided an unending wellspring of love, support, and encouragement through times of great difficulty and celebration. To my Mom and Jon, my Dad and Ginny: this work is yours. I will forever carry the responsibility that comes from being so well loved. To Achim, Tyson, and Brandon: you are my greatest peers, from whom I draw my personal inspiration. Your character, intellect, and friendship fuel my passion for life.

To the people who have come and gone from my life: you have left an indelible impact.

Chapter 2, in full, is a reprint of the material as it appears in A. A. Schafgans, A. D. LaForge, S. V. Dordevic, M. M. Qazilbash, W. J. Padilla, K. S. Burch, Z. Q. Li, Seiki Komiya, Yoichi Ando, and D. N. Basov, "Towards a two-dimensional superconducting state of $La_{2-x}Sr_xCuO_4$ in a moderate external magnetic field", Physical Review Letters 104, 157002 (2010). The dissertation author was the primary investigator and author of this paper.

Chapter 3, in full, is a reprint of the material as it appears in A. A. Schafgans, C. C. Homes, G. D. Gu, Seiki Komiya, Yoichi Ando, and D. N. Basov, "Breakdown of the universal Josephson relation in spin-ordered cuprate superconductors", Physical Review B 82, 100505(R) (2010). The dissertation author was the primary investigator and author of this paper.

Chapter 4, in full, has been submitted for publication of the material as it may appear in A. A. Schafgans, B. C. Pursley, S. V. Dordevic, S. J. Moon, A. D. LaForge, M. M. Qazilbash, A. S. Sefat, D. Mandrus, K. Haule, G. Kotliar, and D. N. Basov, "Electronic correlations and unconventional spectral weight transfer

in $BaFe_{2-x}Co_xAs_2$", Physical Review Letters. The dissertation author was the primary investigator and author of this paper.

Chapter 5, in full, is a reprint of the material as it appears in A. A. Schafgans, B. C. Pursley, A. D. LaForge, A. S. Sefat, D. Mandrus, and D. N. Basov, "Phonon splitting and anomalous enhancement of infrared-active modes in $BaFe_2As_2$", Physical Review B 84, 052501 (2011). The dissertation author was the primary investigator and author of this paper.

Chapter 6, in part, is currently being prepared for submission for publication of the material, A. A. Schafgans, A. A. Taskin, Yoichi Ando, B. C. Chapler, K. W. Post, and D. N. Basov, "Landau levels due to massless Dirac fermions in the topological insulator $Bi_{0.91}Sb_{0.09}$ via magneto-optics".

VITA

2005	B. S. in Physics, University of California, San Diego
2005-2011	Graduate Student Researcher, University of California, San Diego
2011	Ph. D. in Physics, University of California, San Diego

PUBLICATIONS

A. A. Schafgans, A. A. Taskin, Yoichi Ando, B. C. Chapler, K. W. Post, and D. N. Basov, "Landau levels due to massless Dirac fermions in the topological insulator $Bi_{0.91}Sb_{0.09}$ via magneto-optics", in preparation.

A. A. Schafgans, B. C. Pursley, S. V. Dordevic, S. J. Moon, A. D. LaForge, M. M. Qazilbash, A. S. Sefat, D. Mandrus, K. Haule, G. Kotliar, and D. N. Basov, "Electronic correlations and unconventional spectral weight transfer in $BaFe_{2-x}Co_xAs_2$", submitted to Physical Review Letters.

S. J. Moon, A. A. Schafgans, S. Kasahara, Y. Matsuda, M. A. Tatatar, R. Prozorov, A. S. Sefat, D. Mandrus, and D. N. Basov, "Infrared pseudogap in P- and Co-doped $BaFe_2As_2$ high temperature superconductors", submitted to Nature Physics.

A. A. Schafgans, B. C. Pursley, A. D. LaForge, A. S. Sefat, D. Mandrus, and D. N. Basov, "Phonon splitting and anomalous enhancement of infrared-active modes in $BaFe_2As_2$", Physical Review B 84, 052501 (2011).

M. M. Qazilbash, A. Tripathi, A. A. Schafgans, Bong-Jun Kim, Hyun-Tak Kim, Zhonghou Cai, M. V. Holt, J. M. Maser, F. Keilmann, O. G. Shpyrko, and D. N. Basov, "Nano-imaging of the electronic and structural transitions in vanadium dioxide", Physical Review B 83, 165108 (2011).

A. Dubroka, M. Roessle, K. W. Kim, V. K. Malik, D. Munzar, D. N. Basov, A. A. Schafgans, S. J. Moon, C. T. Lin, D. Haug, V. Hinkov, B. Keimer, Th. Wolf, J. G. Storey, J. L. Tallon, and C. Bernhard, "Evidence of a precursor superconducting phase at temperatures as high as 180 K in $RBa_2Cu_3O_{7-\delta}$ (R=Y,Gd,Eu) superconducting crystals from infrared spectroscopy", Physical Review Letters 106, 047006 (2011).

A. A. Schafgans, C. C. Homes, G. D. Gu, Seiki Komiya, Yoichi Ando, and D. N. Basov, "Breakdown of the universal Josephson relation in spin-ordered cuprate superconductors", Physical Review B 82, 100505(R) (2010).

A. A. Schafgans, A. D. LaForge, S. V. Dordevic, M. M. Qazilbash, W. J. Padilla, K. S. Burch, Z. Q. Li, Seiki Komiya, Yoichi Ando, and D. N. Basov, "Towards a two-dimensional superconducting state of $La_{2-x}Sr_xCuO_4$ in a moderate external magnetic field", Physical Review Letters 104, 157002 (2010).

J. M. Tranquada, D. N. Basov, A. D. LaForge, and A. A. Schafgans, "Interpreting quantum oscillation experiments on underdoped $YBa_2Cu_3O_{6+x}$", Physical Review B 81, 060506(R) (2010).

A. D. LaForge, A. A. Schafgans, S. V. Dordevic, W. J. Padilla, K. S. Burch, Z. Q. Li, Kouji Segawa, Seiki Komiya, Yoichi Ando, J. M. Tranquada, and D. N. Basov, "Possibility of magnetic-field-induced reconstruction of the Fermi surface in underdoped cuprates: Constraints from infrared magneto-optics", Physical Review B 81, 064510 (2010).

A. D. LaForge, W. J. Padilla, K. S. Burch, Z. Q. Li, A. A. Schafgans, Kouji Segawa, Yoichi Ando, and D. N. Basov, "Magnetic field induced modification of superuid density and interplane spectral weight in $YBa_2Cu_3O_y$", Physical Review B 79, 104516 (2009).

M. K. Stewart, K. B. Chetry, B. Chapler, M. M. Qazilbash, A. A. Schafgans, A. Gupta, T. E. Tiwald, and D. N. Basov, "Ellipsometric study of the electronic band structure of CrO_2 across the ferromagnetic transition", Physical Review B 79, 144414 (2009).

A. D. LaForge, W.J. Padilla, K.S. Burch, Z.Q. Li, A. A. Schafgans, Kouji Segawa, Yoichi Ando, and D.N. Basov, "Sum rules and interlayer infrared response of the high temperature $YBa_2Cu_3O_y$ superconductor in an external magnetic field", Physical Review Letters 101, 097008 (2008).

M. M. Qazilbash, A. A. Schafgans, K. S. Burch, S. J. Yun, B. G. Chae, B. J. Kim, H. T. Kim, and D. N. Basov, "Electrodynamics of the vanadium oxides VO_2 and V_2O_3", Physical Review B 77, 115121 (2008).

K. S. Burch, A. A. Schafgans, N. P. Butch, T. A. Sayles, M. B. Maple, B. C. Sales, D. Mandrus, and D. N. Basov, "Optical Study of Interactions in a d-Electron Kondo Lattice with Ferromagnetism", Physical Review Letters 95, 046401 (2005).

ABSTRACT OF THE DISSERTATION

Correlations as Causation:
Optical Properties of Strongly Correlated Matter

by

Alexander Anthony Schafgans

Doctor of Philosophy in Physics

University of California, San Diego, 2011

Professor Dimitri Basov, Chair

This dissertation presents infrared and magneto-optical spectroscopy experiments that probe emergent phenomena in various correlated and complex electronic materials. By examining the frequency dependent optical constants as a function of temperature, magnetic field, and chemical doping, we draw conclusions about the nature of the physical processes that govern the materials. We predominately explore the vast phase-space of the two currently known families of high-critical temperature superconductors, the cuprates and the pnictides, before turning to a magneto-optical study of Landau levels in a newly discovered three dimensional topological insulator. We present detailed magneto-optical results in the superconducting state of $La_{2-x}Sr_xCuO_4$ and demonstrate that in-plane magnetic

order, present only in the underdoped samples, quenches interplane Josephson coupling. We then generalize these results and show that, for spin ordered cuprates, the universal Josephson relation breaks down. Turning to the 122-family of pnictides, we demonstrate that electronic correlations in $BaFe_{2-x}Co_xAs_2$ are doping independent and lead to spectral weight transfer as a function of temperature over an energy scale defined by Hund's rule coupling. By closely monitoring the infrared-active phonon modes across the structural phase transition, we show how Hund's coupling is evident in another observable: the low-temperature phonon oscillator strength enhancement. This previously anomalous phonon behavior results from reduced electronic screening driven by anisotropic in-plane conductivity as a consequence of the Pauli exclusion principle.

Chapter 1

Introduction

Infrared/optical spectroscopy is the utilization of light to probe the natural world. This dissertation is concerned with light over a broad energy range, from the very far infrared (2 meV = 16 cm^{-1}) into the ultraviolet (6 eV = 48,000 cm^{-1}). By examining the response of materials to this broad range of incident light, it is possible to gain insight into the fundamental physical process at work within. From low energy phenomena such as lattice vibrations, the free electron gas in metals, gaps or partial gaps in the electronic density of states due to superconducting, charge, and magnetic order to higher energy phenomena such as electronic interband transitions, broadband spectroscopy is particularly powerful because different physical processes are excited by different energies of light. By monitoring the spectral response of materials subjected to an external stimulus such as temperature and magnetic field or as a function of chemical substitution (doping), one can systematically explore the vast phase space to uncover the underlying physical laws. In the following five chapters, we present the results from experiments on the cuprate and iron-pnictide families of high-temperature superconductors as well as a recently identified topological insulator.

It is well established that the CuO_2 plane is the universal building block of the cuprate high-critical temperature (T_c) superconductors. Despite the strong anisotropy of electronic properties between the in-plane (a- and b-axes) and interplane (c-axis) directions, superconductivity in the cuprates is a three-dimensional phenomenon owing to strong interplane (Josephson) coupling. The issue of whether

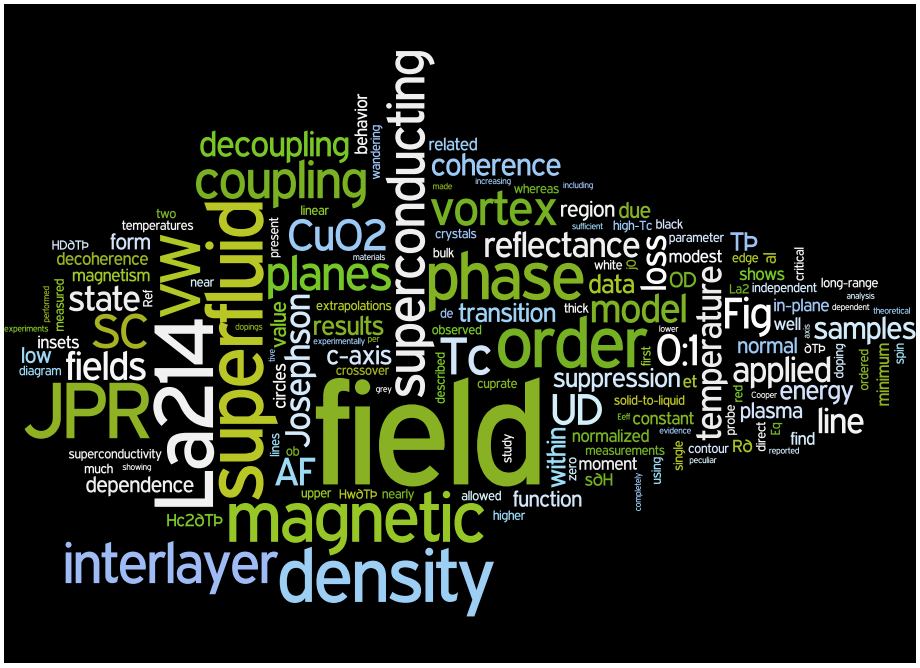

Figure 1.1: Graphical representation of the text in chapter 2. The relative size of the word correlates with the frequency of word use in chapter 2.

an isolated CuO_2 plane in a bulk single crystal can support superconductivity remains unsettled even though there have been numerous experimental attempts to resolve this fundamentally important question. It has proven difficult to realize an experiment in which only Josephson coupling is eliminated while in-plane superconductivity remains. This is precisely what we have accomplished in the magneto-optics experiments discussed in chapter 2.

We show that with a modest applied magnetic field, we were able to drive the bulk superconducting ground state of the prototypical cuprate superconductor $La_{2-x}Sr_xCuO_4$ (La214) into a peculiar 2D-supercondcuting state. By observing the Josephson plasma resonance (JPR) via infrared magneto-optics, we directly probed the strength of interlayer coupling. We found that for underdoped La214 crystals, the JPR can be quenched without noticeably impacting superconductivity

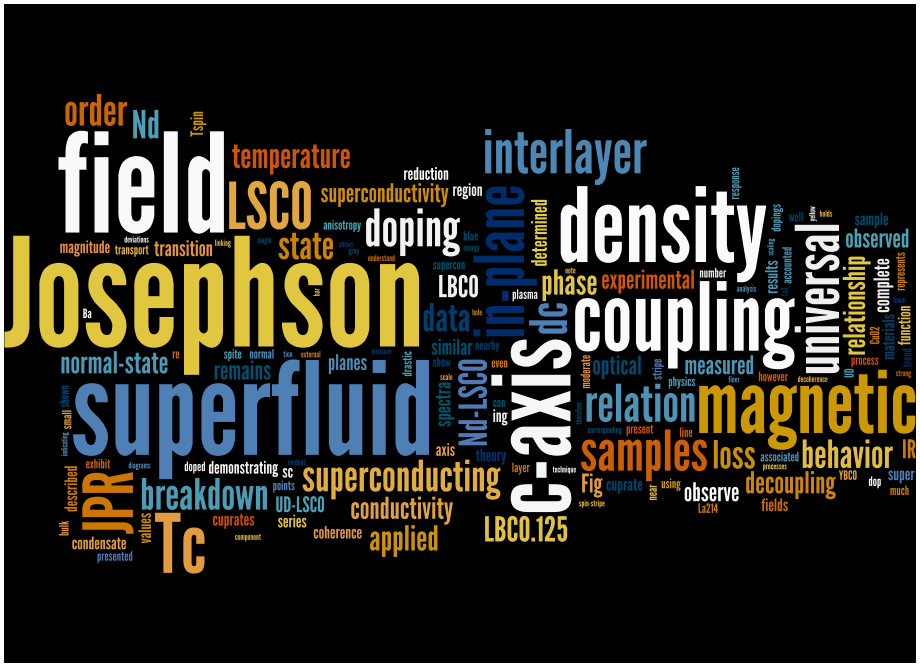

Figure 1.2: Graphical representation of the text in chapter 3. The relative size of the word correlates with the frequency of word use in chapter 3.

within the CuO_2 planes. Furthermore, our observations are directly related to field-induced antiferromagnetism discovered by Lake et. al. (12). We thereby introduce the notion that in-plane magnetic order causes interlayer phase decoherence and actually quenches interlayer coupling all together.

This experiment has not previously been performed due to the complexity of infrared studies in Voight geometry: the polarization of the incident electric field must be parallel with the externally applied magnetic field, which in turn must be directed along the crystallographic c-axis. The unexpected field-sensitivity of the interlayer coupling uncovers novel aspects of competing ground states in the high-T_c superconductors. Indeed, field-induced antiferromagnetism in the CuO_2 planes appears to be harmless for superconductivity but is drastically detrimental for the interplane coupling.

Chapter 3 builds on the experimental findings in the previous chapter and draws more general conclusions about an entire class of cuprate superconductors. Among the most significant contributions to the understanding of high-T_c cuprate superconductors are observations of behaviors that hold true for all cuprates. Universal behaviors offer a window to quantitative predictions with the ultimate goal of illuminating underlying physical principles that lead to a complete theoretical description. One such universal trend relates the normal state conductivity to the superfluid density in the superconducting state (36). In the specific case of the interlayer response, this universal trend can be viewed as an inescapable outcome of Josephson coupling between the two-dimensional CuO_2 planes. We refer to this generic effect as the universal Josephson relation. The novelty of chapter 3 is to explore dramatic departures from this universal trend in a number of Ba, Sr and Nd-doped cuprates of the La_2CuO_4 series. An exploration of the entirety of the data suggests that the breakdown of Josephson physics is uniquely linked with the development of magnetic order in the CuO_2 planes.

Chapter 3 combines experimental results for Ba-doped $La_{2-x}Ba_xCuO_4$ crystals and magneto-optics results for $La_{2-x}Sr_xCuO_4$ with previously reported data for $La_{1.85-y}Nd_ySr_{0.15}CuO_4$. The breakdown in an entire class of materials of a relationship that was previously thought to be universal calls for a close reexamination of the underlying physical descriptions. Indeed, the field- and doping-induced antiferromagnetism in the CuO_2 planes appears to be harmless for superconductivity within the planes but is drastically detrimental to the interplane coupling. Previously unexplored facets of the Josephson coupling in magnetically ordered layered systems that we report here put constraints on theoretical models and call for the systematic examination of interlayer effects in other classes of layered superconductors.

One pressing question in the field of high-T_c superconductivity is whether strong electronic correlations in general, and Mott physics specifically, are among necessary preconditions for the high-T_c phenomenon. Chapter 4 shows that both the cuprate and the iron-pnictide high-T_c superconductors are strongly correlated materials: that is, their electronic properties cannot be described with simple band

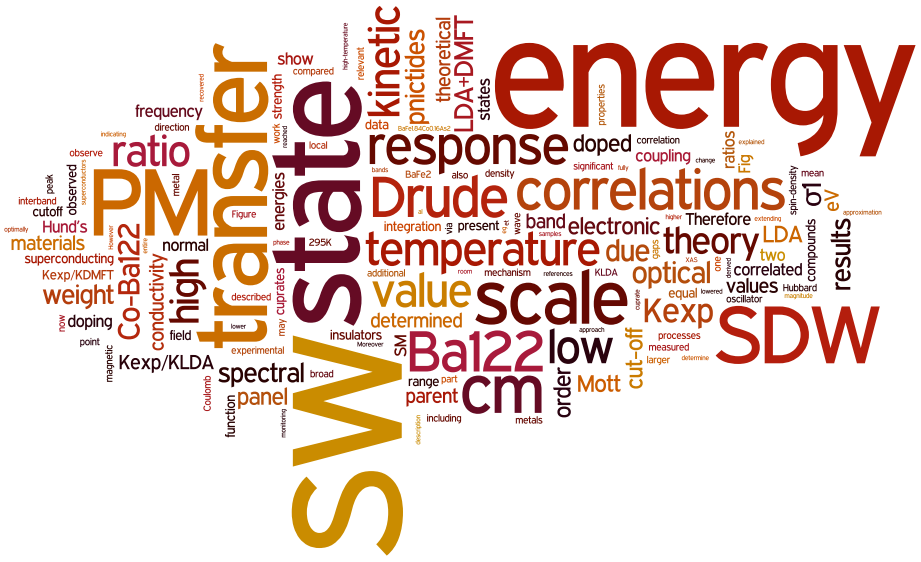

Figure 1.3: Graphical representation of the text in chapter 4. The relative size of the word correlates with the frequency of word use in chapter 4.

theory. By understanding the origin of the electronic correlations, one can gain access to the particular ground state in each family of materials. Such a privileged look behind the curtain of correlations will reveal the fundamental differences between the cuprate and pnictide high-T_c families.

Chapter 4 explores results from infrared spectroscopy to elucidate the electronic properties of the parent and optimally doped iron-pnictide $BaFe_{2-x}Co_xAs_2$. By comparing the optical conductivity with theoretical expectations, we show that the strength of correlations is unaffected by the magnetic phase transition from paramagnetic metal to spin-density wave metal. Neither does Co-doping into the superconducting phase change the strength of correlations. These results are unexpected in light of doped Mott-insulators such as the cuprates, where electronic correlations decrease linearly as the material is doped.

In addition to the strength of correlations, chapter 4 discusses the energy scale and direction of spectral weight transfer as a function of decreasing temperature. The energy scale of spectral weight transfer reveals information about the underlying physical interaction that gives rise to the strong correlations. This energy scale turns out to be much less than the strength of the Coulomb interaction. Furthermore, we observe spectral weight in the Drude response to decrease as temperature is lowered, in contrast to the cuprates and other metals derived from Mott insulators. As such, we are able to conclude that the Coulomb interaction is an unlikely source of correlations. Instead, we demonstrate that the electronic correlations in the pnictides are primarily due to Hund's coupling. The ground state of the pnictides is therefore fundamentally different than the cuprates.

The experimental techniques that came of age during the curprate era have been uniquely suited for studying the properties of the more novel iron-pnictide family of high-T_c materials. As such, the speed of experimental progress towards understanding the properties of the pnictides has been unprecedented. Yet, as chapter 5 discusses, certain properties that should be reasonably expected from theory have remained illusive. One such unfulfilled expectation is the changing lattice dynamics across the structural and magnetic phase transition in the pnictide parent compounds. Group theory predicts two doubly degenerate infrared-active in-plane phonon modes in the high temperature tetragonal phase. Once the material undergoes the structural transition into the low temperature orthorhombic phase, the degeneracy is expected to be broken and four phonons should be evident.

Of course, many experimental predictions go unverified in complex materials. However, previous infrared spectroscopic measurements found the infrared-active modes to experience a drastic oscillator strength enhancement in the orthorhombic phase. Due to the fact that phonon splitting remained unobserved, these reports could not definitively comment on the origin of the anomalous enhancement.

Chapter 5 discusses far-infrared spectroscopic measurements of the phonon modes in the pnictide parent compound $BaFe_2As_2$. We observe the same anoma-

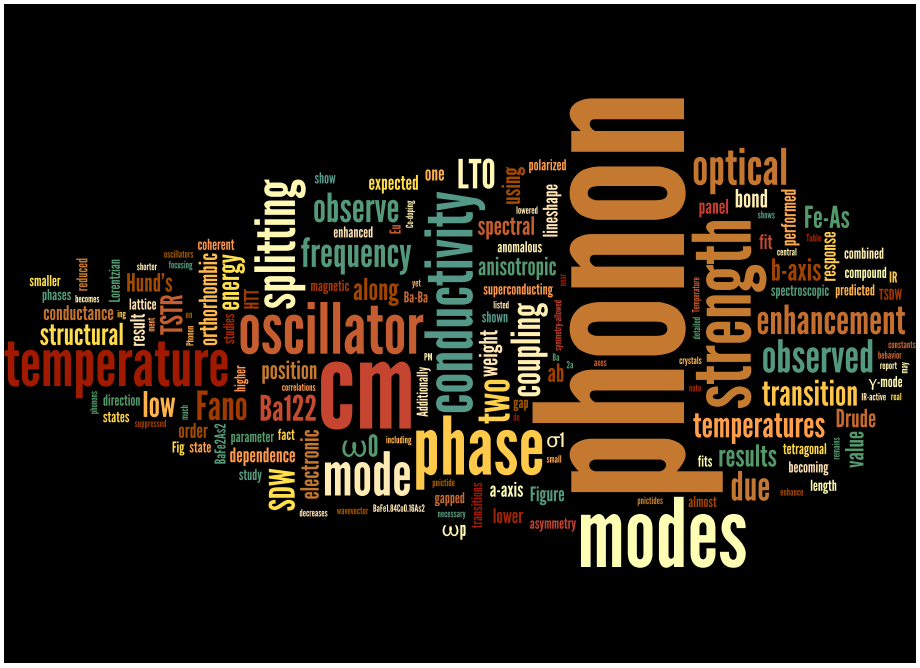

Figure 1.4: Graphical representation of the text in chapter 5. The relative size of the word correlates with the frequency of word use in chapter 5.

lous oscillator strength enhancement reported previously. Importantly, however, as the lattice degeneracy is lifted at low temperature, we provide the first observation of all four symmetry allowed infrared-active phonon modes. By quantitatively modeling the phonon lineshapes, we uncover a subtle asymmetry of the strongly enhanced phonon. Such asymmetry is due to coupling of the phonon to the continuum of electronic states. After carefully studying the quantitative properties of the four observed phonon modes, we draw conclusions about the origin of the anomalous phonon behavior. Namely, our observations have only one possible microscopic origin: anisotropic conductivity as a consequence of Hund's rules.

Finally, in chapter 6, we discuss a magneto-infrared study of the three dimensional topological insulator $Bi_{1-x}Sb_x$. The phenomenon of conducting edge or surface states existing in an insulating host material was, until recently, restricted to the (spin) quantum Hall effect. In 2D electron systems (2DEG), where a conducting electron gas exists in a dimensionally confined surface state, a sufficiently strong applied magnetic field can eliminate conduction paths through the 2DEG by binding electron to the magnetic field lines. However, as the applied field is increased, conduction paths exist at the edge of the material whenever a filled Landau level crosses the Fermi energy, giving rise to the familiar quantum Hall effect.

Three dimensional topological insulators (3DTI) are, conceptually, an extension of the (spin) quantum Hall effect. There are crucial differences, however, because in a 3DTI, conducting surface states exist only in the absence of an applied magnetic field. These states arise due to the specific nature of the Hamiltonian that describes inverted band semiconductors. Therefore, the surface states in 3DTIs are robust to any time-reversal invariant perturbation. Under the application of a time-reversal invariant magnetic field, the surface states can be gapped. For this reason, studying the properties of 3DTIs in magnetic field can yield specific information about the nature of the surface states. This is the object of our study presented in chapter 6, detailing the observation of Landau levels due to the Dirac bands which give rise to surface states in $Bi_{1-x}Sb_x$.

Figure 1.5: Graphical representation of the text in chapter 6. The relative size of the word correlates with the frequency of word use in chapter 5.

Chapter 2

Towards a two-dimensional superconducting state of $La_{2-x}Sr_xCuO_4$ in a moderate external magnetic field

Abstract

We report a novel aspect of the competition and coexistence between magnetism and superconductivity in the high-T_c cuprate $La_{2-x}Sr_xCuO_4$ (La214). With a modest magnetic field applied $H \parallel c$-axis, we monitored the infrared signature of pair tunneling between the CuO_2 planes and discovered the complete suppression of interlayer coupling in a series of underdoped La214 single crystals. We find that the in-plane superconducting properties remain intact, in spite of enhanced magnetism in the planes.

2.1 Introduction

Understanding the interplay between the magnetic and superconducting order parameters in the cuprate high transition temperature (T_c) materials has

presented a substantial experimental and theoretical challenge (1). Recent experiments focused on very low-T_c Ba-doped and Sr, Nd-co-doped La_2CuO_4 and have uncovered that the onset of charge and spin stripelike order leads to the loss of coherence in the superconducting condensate between neighboring CuO_2 planes, resulting in a peculiar two-dimensional (2D) superconducing state (2; 3; 4). In this letter, we show that moderate magnetic fields promote static spin-density wave (SDW) order, which competes with interlayer coherence and leads to a 2D-superconducting state.

2.2 Experiment

Our study focuses on the Josephson plasma resonance (JPR): a collective mode of Cooper pairs oscillating between the CuO_2 planes at $T < T_c$. The JPR is a signature of bulk 3D superconductivity (SC) in the cuprates (5; 6; 7), which can be envisioned as a stack of Josephson coupled CuO_2 planes, and thus is a sensitive probe of the interlayer phase coherence. The JPR is readily observed using infrared (IR) spectroscopy since it results in the formation of a characteristic plasma edge in far-IR reflectance (Fig. 2.1a) (8). By monitoring the JPR in the previously unexplored parameter space of temperature, doping and magnetic field, we are able to investigate the strength of the interlayer phase coherence, allowing us to draw insights into the interplay between magnetism and SC in the La214 system.

The samples in this study were single crystals between 4-6 mm in diameter and 2-3 mm thick with the *ac*-face oriented normal to the incident light. Fabrication and characterization of the samples have been described elsewhere (9). The magneto-optical measurements were performed in an 8 Tesla superconducting magnet at temperatures from 8 K to 295 K and the samples were cooled using He gas exchange (10). The field-dependent absolute reflectance $R(\omega)$ was measured over a range of 15 to 700 cm^{-1}. This was combined with zero-field, temperature dependent data ranging from 15 to 45,000 cm^{-1}, to which we applied a Kramers-Kronig analysis in order to extract the optical constants. Low-frequency extrapolations

were made using a two-fluid model whereas all high-frequency extrapolations were made assuming a linear regime of $R(\omega)$ eventually decaying as $R(\omega) \propto \omega^{-4}$.

We start by exploring the JPR in x=0.1 La214, well into the underdoped (UD) side of the phase diagram (Fig. 2.1a, inset). The low energy c-axis reflectance $R(\omega)$ in the normal state is insulatorlike, as characterized by a low magnitude and the absence of a metallic plasma edge. There are a series of IR-active phonons in the far-IR region (100-700 cm^{-1}), followed by a nearly constant reflectance in the mid-IR range (700-6000 cm^{-1}). As the sample is cooled below T_c, we observe a low-frequency plasma edge develop (the JPR) with a minimum at $\omega = \omega_p$, frequencies below which the reflectance approaches unity. With decreasing temperature below T_c, the JPR moves to higher energies as the superfluid density increases. This is because the JPR is directly related to the superfluid density (ρ_s) as,

$$\rho_s = \frac{c^2}{\lambda^2} = \omega_p^2 * \epsilon_\infty = \frac{4\pi e^2 n}{m^*} \tag{2.1}$$

where λ is the penetration depth, ω_p is the screened plasma frequency and is determined by the number density (n) and effective mass (m^*) of Cooper pairs contributing to the superconducting condensate and the high energy value of the dielectric constant (ϵ_∞).

When a magnetic field is applied $H \parallel c$-axis, the JPR decreases in energy, corresponding to a decrease of the c-axis superfluid density. Figure 1a shows the field dependence of $R(\omega)$ of the x=0.1 sample at T=8 K. We find that an applied field of 8 T, well below the upper critical field $H_{c2}(T)$, is sufficient to nearly restore the reflectance to the insulating normal state value. Our observation of the extinction of the JPR in modest fields is an unprecedented and unexpected result (11). We define the magnetic field that is sufficient to quench the c-axis superfluid density below the sensitivity of our measurement to be the decoupling field $H_D(T)$.

The temperature dependence of $H_D(T)$ is plotted in Fig. 2.1c for x=0.1 (red circles). With increasing temperature, correspondingly smaller fields are needed to quench the JPR. It is instructive to analyze this decoupling line in conjunction with other characteristics of the vortex state; in Fig. 2.1c we reproduce magneto-resistance data presented by Lake, *et. al.* (12). White circles represent the solid-to-liquid vortex phase transition and we have emphasized the constant contour of

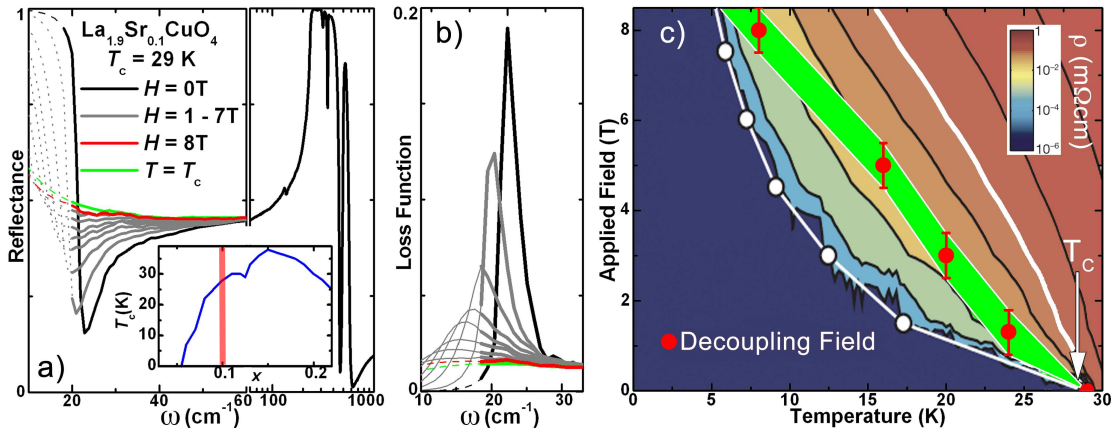

Figure 2.1: (a) Far-infrared reflectance of x=0.1 La214 showing the evolution of the JPR at T=8 K in magnetic field. By 8 T, the reflectance is restored to the normal state value within the signal to noise of our experiment. The JPR is the only feature in the spectra that is sensitive to the field. Dashed lines are extrapolations. Inset: the superconducting phase diagram of La214 for various Sr content. (b) Loss function at T=8 K for x=0.1 La214, further described in Fig. 2. (c) Superconducting phase diagram for La214 x=0.1, showing the decoupling field $H_D(T)$ (red circles) with magneto-resistance data reproduced from Ref.(12); white circles show the solid-to-liquid vortex phase transition, thick white line (our emphasis) is a constant contour of resistivity near the T_c value. Josephson coupling vanishes with increasing field in the green region, the width determined by the uncertainty in H_D. This region signifies the crossover from 3D to 2D superconductivity.

resistivity near the T_c value with a thick solid white line. This contour represents an estimate of the resistive critical field $H^{\rho}_{c2}(T)$ (13), which can be thought of as the loss of long range phase coherence within the CuO_2 planes. The resistive transition to the normal state is gradual. However, $H^{\rho}_{c2}(T)$ should be considered a lower bound on the mean-field pair-breaking field $H_{c2}(T)$ as Nernst effect measurements and specific heat data suggest $H_{c2}(T)$ is much higher and most likely remains temperature independent at low temperatures compared to T_c (14; 15). Figure 2.1c shows that the decoupling field is located in the vortex liquid region, well below the loss of long-range superconducting order and the pair-breaking field (13; 15; 16). In the following, we provide evidence that the decoupling line marks a crossover from 3D SC with prominent Josephson coupling to 2D SC characterized by isolated CuO_2 planes.

In accord with the latter statement, we performed a-axis polarized reflection measurements and observed only slight degradation of the in-plane superfluid density in magnetic field by $H_D(T)$, within error (Table 2.1) (17). The anisotropy of the superfluid density (ρ^a_s/ρ^c_s) is dramatically enhanced, by at least a factor of 10, due to the depletion of the c-axis superfluid in magnetic field. We conclude that superconducting pairing within the CuO_2 planes is unharmed by the loss of interlayer coherence. An implication of these results is that an isolated CuO_2 plane in bulk La214 can maintain high-T_c SC.

Table 2.1: Superfluid density measured for $x = 0.1$ La214 at $T = 8$ K, with experimentally established upper/lower bounds for in-field suppression

H (Tesla)	$\frac{\rho^a_s(H)}{\rho^a_s(0)}$	λ_{ab} (nm)	$\frac{\rho^c_s(H)}{\rho^c_s(0)}$	$\lambda_c(\mu\text{m})$	$\frac{\rho^a_s}{\rho^c_s}$
0	1	406 ± 9	1	12.6 ± 0.4	10^3
8	≥ 0.70	≤ 485	≤ 0.07	≥ 48	$\geq 10^4$

To illustrate how the in-field behavior changes with doping, Fig. 2.1b and Fig. 2.2 present the c-axis loss function spectra ($-Im[1/\epsilon(\omega)]$). The loss function quantifies the response of longitudinal modes such as the JPR, which produces a sharp peak centered at $\omega = \omega_p$. For the UD samples ($x = 0.1, 0.125$), the peak in the loss function is quenched at low temperatures with only a modest applied magnetic field, while for the near optimally doped (OD) samples ($x = 0.15$ and

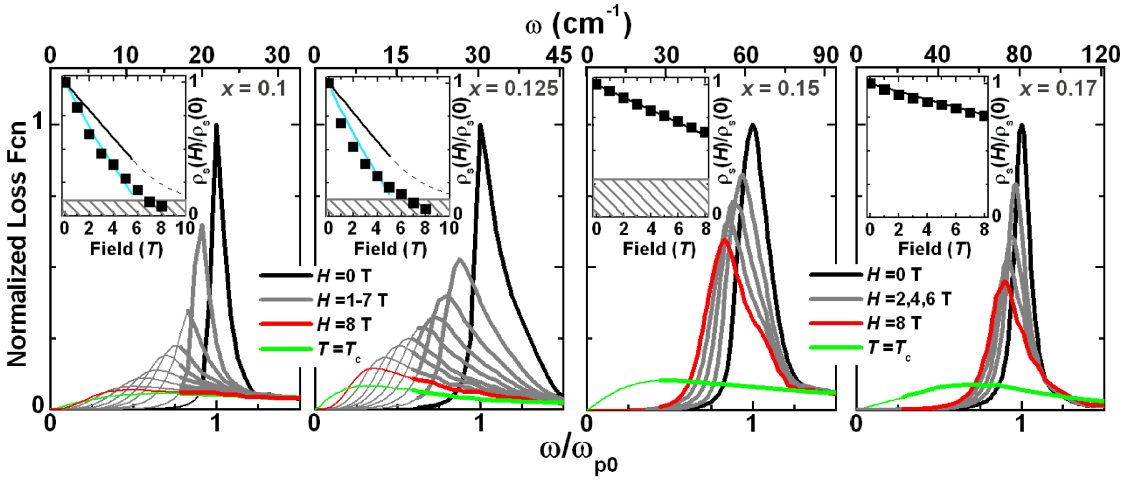

Figure 2.2: Field dependence of the normalized loss function $(-Im[1/\epsilon(\omega)]/-Im[1/\epsilon(\omega_{p0})])$ for the four dopings studied at T=8 K. Thick lines are range of extrapolation independent results. Insets: Normalized superfluid density $\rho_s(H,T)/\rho_{s0}(T)$ vs. applied field at T=8 K. Solid black lines represent the VW model predictions (eqn. 2.2), and become a dashed guide to the eye at the vortex solid-to-liquid phase transition. Horizontal grey line is the minimum in Josephson coupling allowed by the VW model while values in the grey hashed region are not allowed. In the x=0.1 and 0.125 insets, the blue line is of the form in eqn. 2.6 with A = 1, 1.6 for x= 0.1 and 0.125, respectively. The size of the superfluid data points represents the uncertainty due to the form of the low frequency extrapolations. The VW model predicts decoupling fields for x=0.1, 0.125, 0.15, 0.17 of $H_w(T)$=9.6T, 9.1T, 21 T and 34 T.

0.17), the suppression is much weaker. These distinctions between the UD and OD crystals are evident from the inspection of the insets to Fig. 2.2, where we plot the normalized superfluid density $(\rho_s(H,T)/\rho_{s0}(T))$ versus applied field. (We used a technique described in Ref. (18) to determine the extrapolation independent superfluid density from the imaginary part of the optical conductivity.) The functional form of $\rho_s(H,T)/\rho_{s0}(T)$ is markedly different between the two doping regimes: the UD behavior is sub-linear whereas the OD behavior is entirely linear.

2.3 Theoretical Modeling and Discussion

To explain the suppression of the superfluid density at fields much smaller than the pair-breaking field, we first look to the vortex wandering model (VW)

(7; 19; 20), which describes how the displacement of vortices between neighboring CuO_2 planes induces a phase difference in the superconducting order parameter. According to the VW model, the strength of the interlayer coupling energy $E_j^{eff}(H,T)$ can be related to the decoupling field due solely to vortex wandering $H_w(T)$ (21) as

$$\frac{E_j^{eff}(H,T)}{E_{j0}(T)} = 1 - \frac{H}{H_w(T)} \equiv v_w(H,T) \tag{2.2}$$

where $E_{j0}(T)$ is the zero-field coulpling energy and

$$H_w(T) \approx (E_{j0}(T) + E_{m0}(T))\phi_0/U_p. \tag{2.3}$$

$E_{m0}(T)$ is the zero-field magnetic coupling contribution, ϕ_0 is the magnetic flux quanta, and U_p is the pinning potential (19). Equation 2.2 is valid for fields below the vortex solid-to-liquid phase transition; for higher fields, the predicted suppression of the superfluid loses linearity and becomes $\propto 1/H$ (22), moving towards a predicted minimum in interlayer Josephson coupling:

$$\frac{E_{jmin}}{E_{j0}} = \frac{2\pi E_{j0}\xi^2}{U_p} \tag{2.4}$$

(where ξ is the in-plane coherence length). VW cannot drive the interlayer coupling energy to zero and for temperatures $T << T_c$, thermal fluctuations should not play a significant role. For all dopings in our study, $T = 8K << T_c$ satisfies this condition. The normalized superfluid density in magnetic field $\rho_s(H,T)/\rho_{s0}(T)$ is a direct probe of $E_j^{eff}(H,T)/E_{j0}(T)$ and can be related as $E_j^{eff}(H,T)/E_{j0}(T) = \rho_s(H,T)/\rho_{s0}(T)$. Therefore, our observation of the interlayer superfluid density is an informative probe of the vortex state.

The experimental results are plotted as the black squares in the insets to Fig. 2.2 and the VW model prediction is the solid black line in each panel. The VW model works well for x=0.15 and x=0.17. In UD La214, we find a striking deviation between the suppression of the superfluid density and the VW prediction, differing in two significant ways: first, the superfluid density falls with sub-linear dependence on field; second, the measured superfluid continues below the minimum allowed by VW, trending towards zero. This shows that the VW picture, while being completely adequate for OD samples, is insufficient to describe UD La214.

Data in Fig. 2.2 call for an additional mechanism that alters the linear law for $\rho_s(H,T)$ of the VW model and is capable of completely quenching interlayer Josephson coupling. A distinct property of UD La214 crystals is that an applied field can both stabilize fluctuating magnetism and lead to antiferromagnetic (AF) order extending over macroscopic length scales (12; 17; 23; 24; 25; 26). Lake, *et.al.*, demonstrated that the field dependence of the normalized ordered spin moment per copper site scales with the applied field as

$$\frac{\mu_B^2}{M^2} = \frac{H}{H_{c2}(T)} \ln \frac{H_{c2}(T)}{H} \tag{2.5}$$

where M is the magnetic moment per copper site and $H_{c2}(T)$ is the temperature dependent upper critical field (27). If interlayer phase decoherence is assisted by static antiferromagnetism, as suggested by experiment (4) and theory (28), then we expect to find a correlation between the field dependence of the in-plane ordered moment and $\rho_s(H,T)$. The blue line in the UD insets in Fig. 2.2 is of the form

$$\frac{\rho_s(H,T)}{\rho_{s0}(T)} \propto v_w(H,T) - A * \frac{\mu_B^2}{M^2} \tag{2.6}$$

This form assumes that interlayer phase decoherence is produced by a concerted action of vortex wandering (eqn. 2.2) and AF ordering (eqn. 2.5), with an adjustable fitting parameter A. Equation 2.6, while being phenomenological, is in remarkably good agreement with our observations and attests to the notion that AF order directly influences interlayer coupling. In UD La214, this happens in such a way that neighboring planes are driven out of phase. Unlike phase decoherence caused by VW, antiferromagnetically driven decoherence increases until the c-axis superfluid has been entirely quenched. Thus, field-induced AF order appears to be a viable mechanism responsible for complete decoupling of CuO_2 layers and ultimately is the primary cause of the peculiar 2D SC. We stress that field-induced AF order is specific for UD samples and is not found in OD La214, within currently achievable fields.

Our results have direct bearing on reports of the suppression of the JPR in closely related high-T_c materials, including Nd-doped La214 and $La_{2-1/8}Ba_{1/8}CuO_4$ (2; 3; 4; 29). These systems reveal the formation of stripelike charge-density wave

(CDW) order accompanied by stripelike AF order. In both compounds, not only is the JPR mode frustrated, but the key superconducting characteristics within the CuO_2 planes (including T_c and the superfluid density) are degraded. Detailed analysis of $La_{2-1/8}Ba_{1/8}CuO_4$ reported by Tranquada *et. al.* is suggestive of 2D SC in this compound, albeit with a strongly suppressed transition temperature (3). The novelty of the findings reported here is that modest magnetic fields eliminate the JPR in La214 while leaving in-plane SC nearly intact. We stress that in La214, no evidence of field-induced charge order has been identified. Therefore, a correlation between the properties of the JPR and the field-induced magnetic moment conclusively shows that AF spin order alone is the primary competitor of interplane Josephson coupling and is the ultimate reason for 2D SC in this compound.

The theoretical framework for AF-driven interlayer decoupling is developed in the work of Berg, *et. al.* (28) with an alternate perspective offered in Ref.(30). An unresolved issue is to experimentally determine the origin of the AF order; is the observed magnetism due to long-range order of vortex cores or due to large patches of AF stripes? Recent realization of scanning tunneling microscopy on La214 is encouraging in the context of resolving this pressing question through direct experiments (31). Finally, we remark that previous reports of Kosterlitz-Thouless (KT) behavior were confined to the vicinity of T_c (32; 33), whereas our current results extend to $T << T_c$ and may not be KT-like in nature. We present the first observations of a tunable crossover from 3D to 2D SC in a bulk single crystal of a prototypical cuprate. The present work suggests that the phenomenon of 2D SC may be a general characteristic of magnetically ordered cuprates.

2.4 Acknowledgements

We thank S.A. Kivelson, E. Fradkin, and L.N. Bulaevskii for great discussions and acknowledge funding from the NSF and AFOSR MURI. Y. Ando was supported by KAKENHI 19674002 and 20030004.

Chapter 2, in full, is a reprint of the material as it appears in A. A. Schaf-

gans, A. D. LaForge, S. V. Dordevic, M. M. Qazilbash, W. J. Padilla, K. S. Burch, Z. Q. Li, Seiki Komiya, Yoichi Ando, and D. N. Basov, "Towards a two-dimensional superconducting state of $La_{2-x}Sr_xCuO_4$ in a moderate external magnetic field", Physical Review Letters 104, 157002 (2010). The dissertation author was the primary investigator and author of this paper.

Chapter 3

Breakdown of the universal Josephson relation in spin ordered cuprate superconductors

Abstract

We present c axis infrared optical data on a number of Ba, Sr and Nd-doped cuprates of the La_2CuO_4 (La214) series in which we observe significant deviations from the universal Josephson relation linking the normal state transport (DC conductivity σ_{DC} measured at T_c) with the superfluid density (ρ_s): $\rho_s \propto \sigma_{DC}(T_c)$. We find the violation of Josephson scaling is associated with striking enhancement of the anisotropy in the superfluid density. The data allows us to link the breakdown of Josephson interlayer physics with the development of magnetic order in the CuO_2 planes.

3.1 Introduction

Two decades of research in high transition temperature (T_c) superconductivity have uncovered universal behaviors that hold true for all cuprates (18; 34; 35; 36; 37; 38). One example is a scaling relationship linking the normal state trans-

port measured at T_c ($\sigma_{DC}(T_c)$) with the superfluid density (ρ_s): $\rho_s \propto \sigma_{DC}(T_c)$ (18). This relationship is general and holds both for the in-plane and interplane response. The universal relation, defined for the c axis superfluid density and DC conductivity ($\rho_s^c \propto \sigma_{DC}^c(T_c)$) originates from the profound connection between the collective response of the condensate below T_c and single particle properties above T_c in a layered superconductor. Ultimately, the superconducting condensate is formed at the expense of the normal state conductivity at T_c. The amount of spectral weight available for the condensate formation is therefore predetermined by the magnitude of $\sigma_{DC}^c(T_c)$. This conjecture is particularly straightforward in those cases where the conductivity is weakly frequency dependent over the energy scale comparable to the superconducting gap (Fig. 3.1 inset): a situation relevant to cuprates in the underdoped regime. Despite the fact that $\sigma_{DC}^c(T_c)$ varies by 3-4 orders of magnitude between different families of cuprates, it allows for a remarkably reliable prediction of the magnitude of the c-axis superfluid density. In spite of this, small deviations from the $\rho_s^c \propto \sigma_{DC}^c(T_c)$ trend are apparent on the overdoped side of the cuprate phase diagram (18). These relatively minor departures can be accounted for by explicitly considering the energy scale involved in the condensate formation: $\rho_s^c \propto \sigma_{DC}^c(T_c) * T_c$ (36). With the addition of T_c, the universality of Josephson physics in cuprate superconductors has proven to be quite robust and therefore serious departures from this trend are significant. It is from this perspective that we present data demonstrating the unprecedented breakdown of this universal Josephson relationship in La214 materials.

3.2 Experiment

$La_{2-x}Ba_xCuO_4$ (LBCO) and $La_{2-x}Sr_xCuO_4$ (LSCO) samples in this study were grown using a traveling-solvent floating zone technique. The samples were taken from rods and the crystallographic axes were determined by Laue diffraction. The crystals were aligned to better than 1 degree on the Laue camera, then cut and polished with kerosene and diamond paste, with progressively finer and finer laps - the final lap is typically done with 0.1 micron diamond paste, yielding an

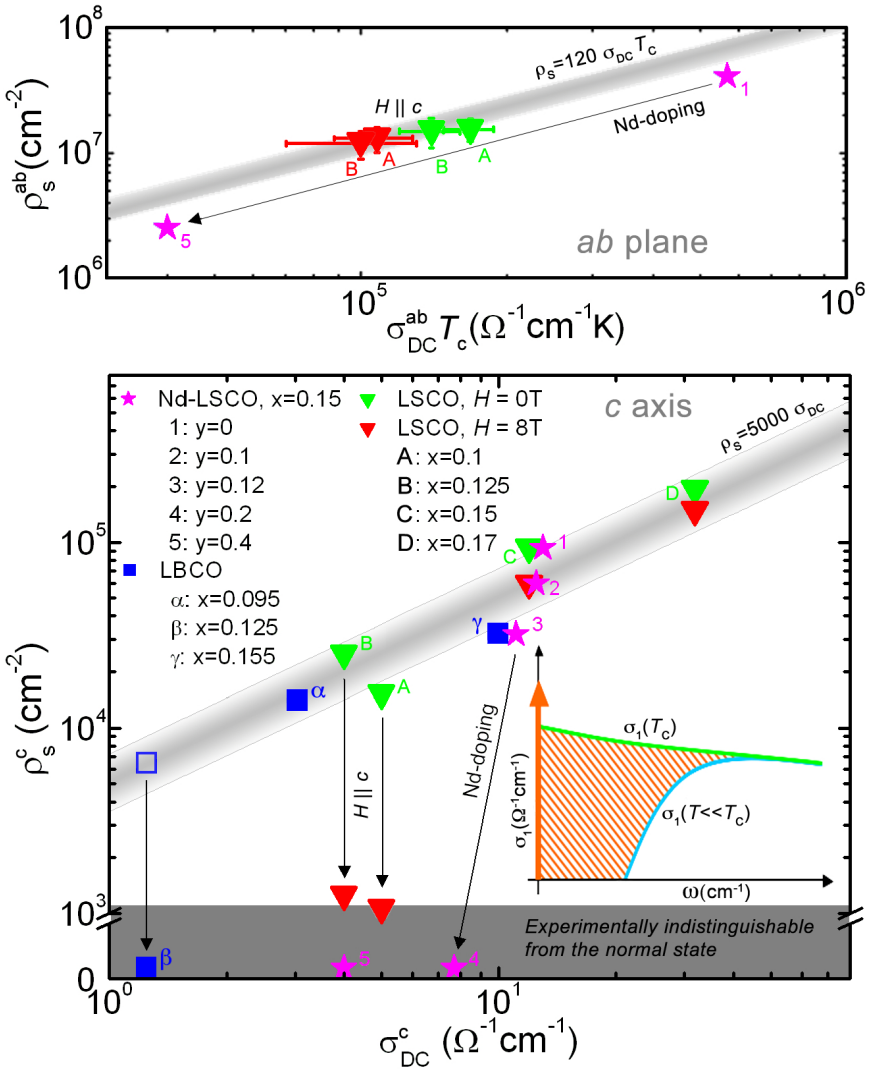

Figure 3.1: *Bottom*: The universal Josephson relation for the interlayer response of cuprate high T_c superconductors $\rho_s^c \propto \sigma_{DC}^c(T_c)$ (grey line). This relation breaks down as the result of applied field (LSCO, points A-D) and doping (Nd-LSCO, points 1-5 and LBCO, points $\alpha-\gamma$). The grey box at the bottom displays the lower limit of detectable superfluid density utilizing infrared optical techniques. *Inset*: Schematic of the normal state conductivity at T_c (green curve) and the superconducting state conductivity (blue curve). The orange hashed region represents the spectral weight that is transferred from finite frequencies into a dissipationless superconducting delta peak (orange arrow) at zero frequency. In materials with weakly frequency dependent normal state conductivities, the DC conductivity provides an accurate estimate of the superfluid density. *Top*: The in-plane universal relation holds in the samples where the c axis Josephson relation breaks down.

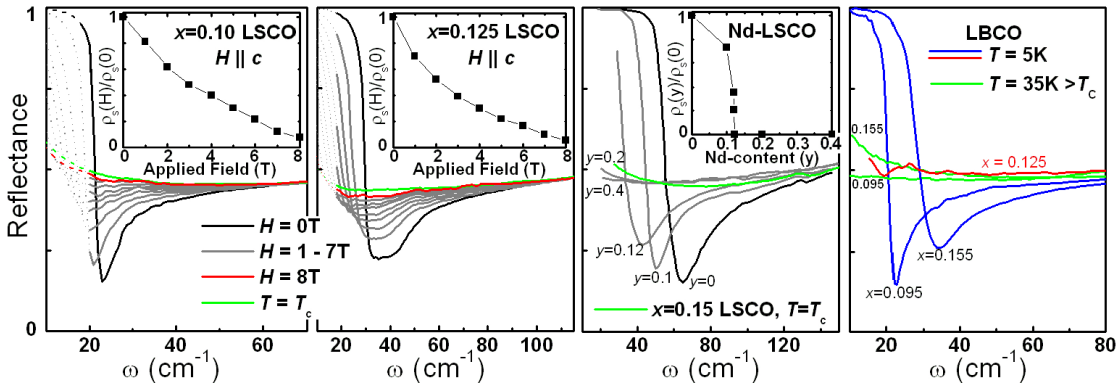

Figure 3.2: Evolution of the Josephson plasma resonance with applied field and doping in a series of La-based single crystals. All data were taken at T=8 K, except where specified. The Nd-LSCO data are replotted from (4), however we measured the x=0.15 LSCO T_c curve on a separate crystal, shown here for reference. LBCO spectra shown for three dopings, demonstrating the absence of c axis coherence in the $x = 0.125$ sample. Insets: Normalized c axis superfluid density as a function of applied field and Nd-content.

optically flat surface with a bright finish.

The magnitude of the interlayer superfluid density was determined using IR spectroscopy. IR spectra measured with the polarization of the electric field vector normal to the CuO_2 planes ($E \parallel c$ axis) (Fig. 3.2) allow one to register a collective plasma mode originating from Josephson coupling of the planes, (the Josephson plasma resonance (JPR)) (6; 37). The superfluid density of the LSCO samples (Insets, Fig. 3.2 a, b) was determined by using an extrapolation-independent technique relying on the imaginary part of the complex optical conductivity (σ_2), as determined through Kramers-Kronig analysis. In the superconducting state, σ_2 is composed of a regular background component and a superconducting component $\sigma_2 = \sigma_2^R + \sigma_2^S$. By taking into account the background contribution σ_2^R as described in Ref. (18), it is possible to accurately determine the superfluid density: $\rho_s = 4\ \pi\sigma_2^S\omega$. The model-independent analysis of the optical constants yields accurate values of ρ_s^c.

Because the c axis superfluid density is mediated by Josephson coupling, the JPR is sensitive to the phase relationship of the superconducting order parameter

between neighboring planes:

$$\rho_s(F,T) = \rho_s(0,T)\langle cos(\phi_{n,n+1})\rangle. \tag{3.1}$$

Here, $\langle cos(\phi_{n,n+1})\rangle$ represents the thermal and disorder average of the phase difference between layer n and n+1, and F is a process that alters the superconducting phase relationship. Any process which, on average, produces a phase difference between layers and suppresses the superfluid density should be evident in the JPR.

3.3 Breakdown of the Josephson relation

The breakdown of the universal relationship occurs upon the application of an external magnetic field or doping, exemplified by a series of LSCO, LBCO, and $La_{1.85-y}Nd_ySr_{0.15}CuO_4$ (Nd-LSCO) samples (Fig. 3.1, bottom). For low Nd content (stars 1-3), the interlayer superfluid density is reduced disproportionately faster compared to the universal trend. The complete breakdown of the universal relation is further evident once $y > 0.12$ (stars 4 and 5), in which any detectable sign of the c axis superfluid density has vanished (Fig. 3.2 insets). Underdoped (UD) LSCO (triangles A and B, Fig. 3.1) reveals similar behavior in a $H \parallel c$ axis applied magnetic field. The behavior of the JPR is very sensitive to field orientation and for $H \parallel ab$ plane, even field values up to 17T are insufficient to significantly impact the JPR (11; 39; 40). The c axis superfluid density drastically decreases in a $H \parallel c$ axis field such that by $H = 8$T, the c axis response is indistinguishable from the normal state just above T_c. The DC conductivity is not impacted by the same field, which results in the 8T data points falling away from the universal line. On the contrary, the optimally doped (OP) LSCO samples (triangles C and D, Fig. 3.1) remain well described by the universal relation. The small suppression of the superfluid density in the OP-LSCO samples is fully accounted for by considering the role of vortices (41). Importantly, for all fields and dopings discussed, the in-plane superfluid density remains well described by the universal relation (Fig. 3.1, top) (41; 45; 46; 47), indicating that the superfluid density anisotropy $\gamma = \rho_s^{ab}/\rho_s^c$ becomes divergent. Later, we discuss the case of LBCO in relation to Fig. 3.1.

To understand the physics responsible for the breakdown of the Josephson relationship, Figure 3.2 shows the JPR in a number of La214 compounds as a function of applied field (LSCO, Figs. 3.2a, b), Nd-doping (Fig. 3.2c), and Ba-doping (Fig. 3.2d). In UD-LSCO, we observe the JPR to be quenched in moderate magnetic fields oriented $H \parallel c$ axis. We define the magnetic field required to quench the JPR below our experimental limitations and restore the c axis IR spectra to the normal state values as the decoupling field H_D. The decoupling field corresponds to the vanishing of the superfluid density ρ_s^c extracted from the optical conductivity (41). Stripe-inducing co-doping (42; 43) can similarly quench the JPR. Results on a series of Nd-LSCO samples (4) and reproduced here (Fig. 3.2c), show that as Nd is added, the JPR is suppressed and moves to lower energies. Near a critical Nd-doping of y=0.12, the JPR is completely quenched and the c axis IR spectra return to the normal state values, indicating the c axis superfluid has vanished. We note that the behavior of the JPR in UD-LSCO in a c axis magnetic field is remarkably similar to what is observed in Nd-LSCO; however magnetic field provides the ability to continuously tune c axis Josephson coupling within the same sample. By observing the loss of the JPR in these materials, we conclude that both a moderate c axis magnetic field and stripe-inducing co-doping causes a drastic reduction of interlayer superconducting phase coherence.

Effects associated with the breakdown of Josephson coupling are further detailed in the phase diagrams shown in Figure 3.3. We plot the behavior of the decoupling field in x=0.10 LSCO as a function of temperature in Fig. 3.3a. We observe the decoupling field to be below the in-plane resistive critical field H_{c2} (black line) and our own in-plane optical measurements (not shown) indicate that the in-plane superfluid remains largely unaffected by the loss of Josephson coupling. The c axis magnetic field causes a drastic reduction in interlayer superconducting coherence as seen in the loss of the superfluid density (Fig. 3.2 insets), at rates much faster than can be accounted for with standard vortex models ((41) and references therein). Therefore, below the decoupling field, the sample is in a three dimensional (3D) superconducting state characterized by Josephson coupled CuO_2 planes while above this field, the sample has transitioned into a two

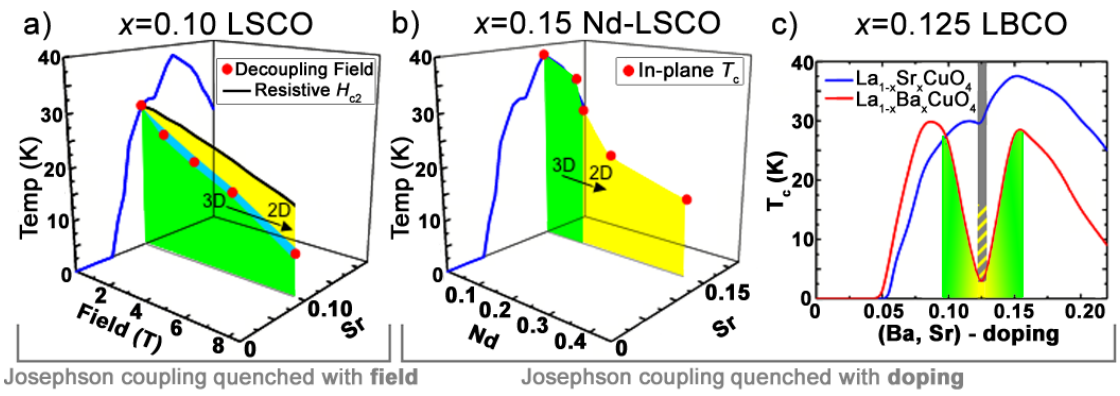

Figure 3.3: Phase diagrams showing magnetic field and doping induced loss of interlayer Josephson coupling, in a number of La214 based materials. Here, the green regions labeled 3D represent parameter space of bulk superconductivity with prominent interlayer Josephson coupling. The yellow 2D regions represent the loss of interlayer Josephson coupling while in-plane superconductivity remains. In Fig. 3.3a, the black line is a constant contour of magneto-resistance near the T_c value (12) and the blue region represents error of the measured decoupling field. In Fig. 3.3c, the spin-stripe ordering transition temperature T_{spin}=40K (grey region) proceeds a Kosterlitz-Thouless transition to two-dimentional superconductivity T_{KT}=16K (hashed bar), where the anisotropy of c axis to ab plane resistivity becomes infinite, within experimental uncertainty. At $T_{3D} \approx 4$ K (yellow region) there is the existence of a bulk Meissner state, while Josephson coupling has not been observed.

dimensional (2D) superconducting state. We obtained similar results for x=0.125 LSCO, whereas the optimal (x=0.15) and overdoped (x=0.17) samples did not exhibit this behavior, with Josephson coupling remaining for all fields measured.

Turning to Nd-LSCO, in Fig. 3.3b we replot T_c as a function of Nd-doping (4). Interestingly, T_c is observed to experience a much smaller suppression as a function of Nd-doping than the c axis superfluid density (Fig. 3.2 insets). This demonstrates that the in-plane superfluid remains intact inspite of the loss of Josephson coupling. Therefore, Nd-doping initiates a transition from the 3D superconducting state characterized by interlayer Josephson coupling to a 2D superconducting state where Josephson coupling is no longer observed. Even though the 3D-2D transition in UD-LSCO is more gradual than in Nd-LSCO, the net result is the same: the complete loss of interlayer Josephson coupling, in stark conflict with the expectations of the conventional theory of Josephson coupling.

Several attributes of the breakdown of the Josephson relationship are also apparent in $La_{1.875}Ba_{0.125}CuO_4$ (LBCO.125). Recently, Tranquada and Li (2; 3) showed striking experimental results for LBCO.125 in which bulk T_c is greatly suppressed from a similar doping $T_c(x = 0.095) = 32$ K to just $T_{3D}(x = 0.125) \approx 4$ K (44). Here, we show IR results demonstrating the behavior of the JPR through this doping range with suppressed T_c (Fig. 3.2d). LBCO samples at nearby dopings show strong JPR features and are in full agreement with the universal Josephson relationship (Fig 3.1, blue squares α, γ). Provided LBCO.125 complies with this universal relation, the expected value for the interlayer superfluid density can be inferred based on the c axis conductivity (open blue square, Fig. 3.1) (2; 3). However, no evidence of the strong JPR feature corresponding to $\rho_s^c = 7000 cm^{-2}$ is found in the IR data for this compound (Fig. 3.2d). Indeed, LBCO.125 at low temperatures is identical to the $T \gtrsim T_c$ spectra at nearby dopings.

These observations point to anomalously anisotropic superconductivity in LBCO.125, similar to Nd-LSCO and UD-LSCO in magnetic field. We have represented LBCO.125 data in Fig. 3.3c. The vertical bar at x=1/8 schematically shows the transport results where below the spin-stripe ordering transition temperature T_{spin}=40 K (grey region), LBCO.125 exhibits behavior reminiscent of the onset of in-plane superconductivity. At zero field, Li *et. al.* identified T_{spin}=40K as the most likely onset temperature of in-plane superconductivity (2), supported by angle-resoved photoemission data demonstrating the presence of a gap consistent with d-wave symmetry (31). For Fig. 3.1, T_{spin} is the temperature we used to determine σ_{DC}. Importantly, c axis resistivity becomes immeasurably small near T=10 K, yet below this temperature we do not observe Josephson coupling (29).

We note again that the in-plane behavior of the superfluid remains well described by the universal relation (Fig. 3.1, top) even when c axis Josephson coupling vanishes. Based on the sensitivity of our experimental setup and difficulty of infrared in-plane superfluid measurements in cuprates, we can bound the amount of remaining superfluid density: in UD-LSCO at T=8K, at least 70% of the in-plane superfluid remains at H=8T. Data available in the literature on Nd-LSCO (45) demonstrates that the in-plane superfluid can be determined by $\sigma_{DC}(T_c) * T_c$,

regardless of the loss of c-axis coherence.

What we observe in the cases presented here is the complete breakdown of Josephson interlayer coupling, induced by an applied magnetic field, Nd or Ba-doping. Ostensibly, these processes are very different. However, they do share one common attribute: all these processes are known to stabilize and enhance static, long-range magnetic order (12; 17; 23; 24; 25; 26; 31; 45; 48). Significantly, all three materials discussed here exhibit in-plane magnetic order that is otherwise not present at nearby doping levels or in the absence of an applied field. Here we underscore the notion that in-plane magnetic order preferentially alters collective pair tunneling along the c axis while the in-plane superfluid remains relatively unimpacted.

The bilayer cuprate $YBa_2Cu_3O_y$ (YBCO), subjected to an external magnetic field applied in the same manner as the LSCO samples presented here, does not display as drastic a loss of Josephson coupling as seen in LSCO (49; 50). There is nonetheless an appreciable reduction in the c axis superfluid density for an applied field for UD YBCO samples, however the rate of the reduction is in line with the vortex wandering model and does not exhibit any anomalous behavior from the standpoint of the universal Josephson relation. The measurements were performed on samples doped between y = 6.67 and 6.95, corresponding to hole concentrations between x = 0.12 and 0.18 (51). Yet even for samples doped near the 1/8 hole concentration where spin order is thought to exist (52), static magnetic order is not observed in YBCO until temperatures much below our measurements (53), implying that YBCO lacks the appropriate magnetic order to facilitate the suppression of c axis Josephson coupling.

Attempts to theoretically understand the breakdown of Josephson coupling have been presented by two groups (28; 30; 54; 55). Both scenarios posit that charge and spin-density wave (CDW and SDW) stripe order suppresses interlayer Josephson coupling. Based on the experimental discoveries discussed here, we can identify several additional aspects of a complete theory of dynamical layer decoupling. In addition to LBCO.125 and Nd-LSCO, the observation of magnetic-field induced phase decoherence in UD-LSCO creates a significantly more stringent set

of experimental constraints on such a theory. Namely, a complete theory cannot rely on commensurability and must be applicable to both the low temperature tetragonal and the low temperature orthorhombic structures of LSCO and LBCO. Since CDW order has not been experimentally observed in UD-LSCO, SDW stripe order appears to be more salient to interlayer decoherence. Additionally, effects only associated with doping and not moderate magnetic fields, such as a modified band structure, cannot be relied on as the sole mechanism of the Josephson breakdown. Finally, based on Fig. 3.1, we observe that the process of applying a magnetic field or doping only destroys pair tunneling and does not seem to impact the single particle properties of the normal state.

3.4 Acknowledgements

We thank S.A. Kivelson, E. Fradkin, J.M. Tranquada, and E. Berg for great discussions and acknowledge funding from the NSF and AFOSR MURI. Y. Ando was supported by KAKENHI 19674002 and 20030004.

Chapter 3, in full, is a reprint of the material as it appears in A. A. Schafgans, C. C. Homes, G. D. Gu, Seiki Komiya, Yoichi Ando, and D. N. Basov, "Breakdown of the universal Josephson relation in spin-ordered cuprate superconductors", Physical Review B 82, 100505(R) (2010). The dissertation author was the primary investigator and author of this paper.

Chapter 4

Electronic correlations and unconventional spectral weight transfer in $BaFe_{2-x}Co_xAs_2$

Abstract

We report an infrared optical study of the pnictide high-temperature superconductor $BaFe_{1.84}Co_{0.16}As_2$ and its parent compound $BaFe_2As_2$. We demonstrate that electronic correlations are moderately strong and do not change across the spin-density wave transition or with doping. By examining the energy scale and direction of spectral weight transfer, we argue that Hund's coupling J is the primary mechanism that gives rise to correlations.

4.1 Introduction

Strongly correlated materials present some of the most interesting challenges to both experimental and theoretical physicists alike. A profound experimental manifestation of correlations is the renormalization of electronic bands due to interactions that are not included in the standard band theory description (56; 57; 58). Correlations are well known to give rise to complex phase diagrams,

as evidenced by the long-standing problem of high-temperature superconductivity in cuprates (8; 59). Since the discovery of the iron-pnictide superconductors, one pressing question in this field is whether correlations in general, and Mott physics specifically, are among necessary preconditions for the high-T_c phenomenon. While both the cuprates and pnictides exhibit an antiferromagnetically ordered ground state in proximity with the superconducting phase ((60; 61) and references therein), the parent compounds of the iron-pnictide materials are metallic with striped spin-density wave order, unlike the antiferromagnetic Mott insulating cuprate parent compounds. As we will show for the 122 class of pnictides, the influence of magnetism via Hund's coupling is the predominant correlation mechanism and is crucial to the electronic properties of the paramagnetic normal and superconducting states.

We measured the optical reflectivity of the parent $BaFe_2As_2$ (Ba122) and optimally doped $BaFe_{1.84}Co_{0.16}As_2$ (Co-Ba122) compounds as a function of temperature over a broad spectral range and extracted the optical constants as described in the Appendix. The real part of the optical conductivity $\sigma_1(\omega)$ is plotted in Figure 4.1. The following discussion will distinguish properties of the spin-density wave (SDW) state, which applies only to the parent compound for $T < T_{SDW} \approx$140K, from properties of the paramagnetic normal state (PM), which applies to $T > T_{SDW}$ in Ba122 and $T > T_c$ in Co-Ba122. All of the $\sigma_1(\omega)$ spectra in the PM state involve a broad Drude response extending to at least 1500 cm^{-1}. In the SDW state, $\sigma_1(\omega)$ is dominated at low energy by the formation of the SDW gaps, exhibiting only a very narrow Drude response (62; 63). Doping does not seem to drastically alter $\sigma_1(\omega)$ in the PM state.

4.2 Determination of electronic correlations

The renormalization of electronic bands due to correlations has a significant effect on two specific observables in infrared spectroscopy: one is a reduced oscillator strength of the Drude response compared with band theory predictions and the other is the energy scale of spectral weight transfer. We now explore each

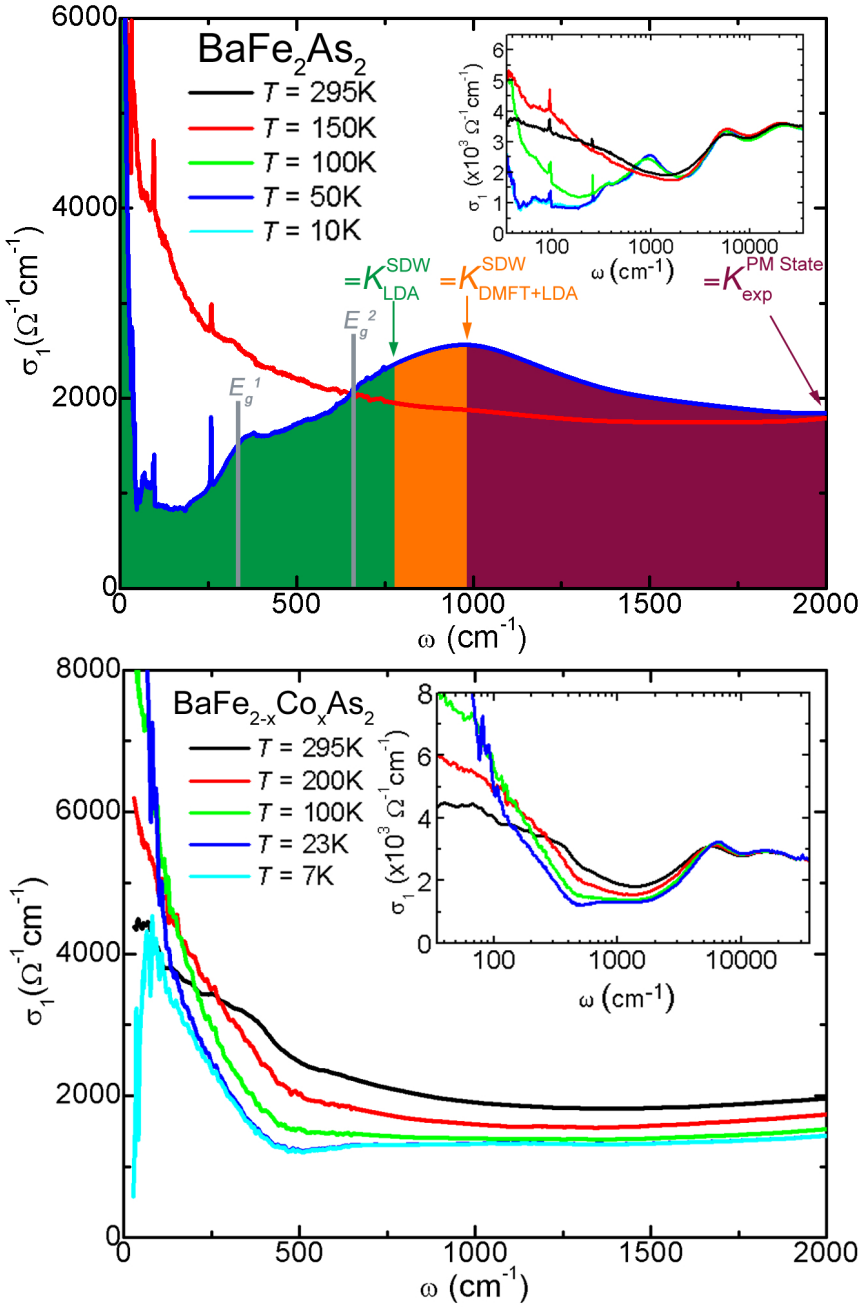

Figure 4.1: Real part of the optical conductivity σ_1 in Ba122 (Top) in the PM ($T = 150K$) and SDW ($T = 50K$) state and Co-Ba122 (Bottom) in the PM normal state and superconducting state ($T = 7K$). For Ba122, we illustrate the necessary integration cutoffs $\Omega = 777$, 969, and 2000 cm^{-1} in order to recover the predicted LDA, LDA+DMFT, and experimentally observed PM state kinetic energy values, respectively. The third cutoff demonstrates that the spectral weight transfer due to the SDW gaps extends to 2000 cm^{-1} and not above.

of these observables in turn. (In the Appendix, we present more details about the samples, experiment, and determination of the SDW gap values.)

In order to quantify the first observable, a reduction of the Drude response compared to band theory, we use a truncated version of the f-sum rule (56). The experimental kinetic energy K_{exp} is proportional to the spectral weight of the Drude component of the optical response and is determined via an integral of the real part of the optical conductivity up to a cut-off value Ω:

$$K_{exp}(\Omega) = \frac{120}{\pi} \int_0^{\Omega} \sigma_1(\omega) d\omega. \tag{4.1}$$

Here we have formulated the equation for kinetic energy in units of cm^{-2}. The cut-off value Ω should be high enough so as to account for all of the Drude weight, yet not so high as to include significant contributions from interband transitions. The multi-band character of the pnictides presents a caveat for this procedure, due to the potential for low-lying interband transitions. We then normalize K_{exp} to K_{LDA}, the band theory estimate under the local density approximation (LDA). The same procedure was used to explore correlations in several different families of exotic superconductors including the pnictides (57; 58; 64). The ratio spans from the extremely correlated case of a fully localized Mott-insulator (eg. the cuprate parent compounds where $K_{exp}/K_{LDA} \approx 0$) to electronically uncorrelated materials such as a fully itinerant metal (eg. copper where $K_{exp}/K_{LDA} \approx 1$). The comparison is instructive because band theory with LDA does not take into account Coulomb repusion U or magnetic interactions that can renormalize the electronic bandwidth and consequently reduce the kinetic energy. Therefore, the ratio of K_{exp}/K_{LDA} emphasizes the significance of correlations due to processes beyond the band theory description.

In Figure 4.2a-c, we plot K_{exp}/K_{LDA} as a function of the cut-off frequency, Ω. The LDA kinetic energy values are given in the caption and were obtained as described in a recent work by Yin, *et. al.* (65). Using arrows, we point out the various cut-offs explained in the Appendix. Irrespective of the cut-off criteria, we find that for Ba122, $K_{exp}/K_{LDA} = 0.25$-0.29 in the PM and 0.2-0.34 in the SDW state. In Co-Ba122, we observe a similar value in the PM normal state: $K_{exp}/K_{LDA} = 0.15$-0.31. Our results demonstrate that correlations are present in

the PM state and remain unchanged at low temperature in the fully-developed SDW state and with doping into the superconducting state.

One recent attempt to theoretically explain the optical conductivity and magnetic moment in the PM state of Ba122 utilizes dynamical mean field theory in conjunction with the local density approximation (LDA+DMFT) (65). In Fig. 4.2 (panel d), we have also plotted the ratio K_{exp}/K_{DMFT}, where K_{DMFT} corresponds to the kinetic energy predicted using LDA+DMFT. This theory can be understood to describe a PM metal with a fluctuating magnetic moment. In Ba122, we find that in the PM state K_{exp}/K_{DMFT} = 0.67-0.77 while in Co-Ba122 the ratio is K_{exp}/K_{DMFT} = 0.68-0.83. We therefore confirm the ability of LDA+DMFT to more accurately describe the optical response in the PM state. However, this conclusion does not hold for the SDW state. In fact, LDA+DMFT underestimates the degree of correlations by an extra 30% over LDA alone, giving K_{exp}/K_{DMFT} = 0.15-0.25. This is surprising due to the qualitative agreement between our data and the theoretical specta. (We note that this discrepancy between K_{exp} and K_{DMFT} may be entirely explained by the excessively high background conductivity in the theoretical results (65).)

Comparison with theory allows us to determine that the strength of correlations in $BaFe_{2-x}Co_xAs_2$ is significant ($K_{exp}(\Omega)/K_{LDA} \approx 0.4$ is an upper bound. For a full description of the sources of error inherent within our technique, see the Appendix.) The strength is on par with what is known to produce the highest T_c in optimally doped cuprates (56; 57; 64). Such reduced kinetic energy from theoretical expectations implies that additional spectral weight (SW) is present at energies higher than the Drude response. In order to elucidate the mechanisms that drive correlations in the Ba122 pnictides, one must determine the energy scale associated with this SW. However, the higher energy SW contribution is not immediately evident in $\sigma_1(\omega)$ due to the obscuring presence of interband transitions. Similar complications arise with doped Mott insulators where the energy scale of U overlaps with the interband structure. Nevertheless, it is possible to gain direct information about the magnitude of U in doped Mott insulators by carefully monitoring the distribution of SW as it changes with doping and temperature (66; 67).

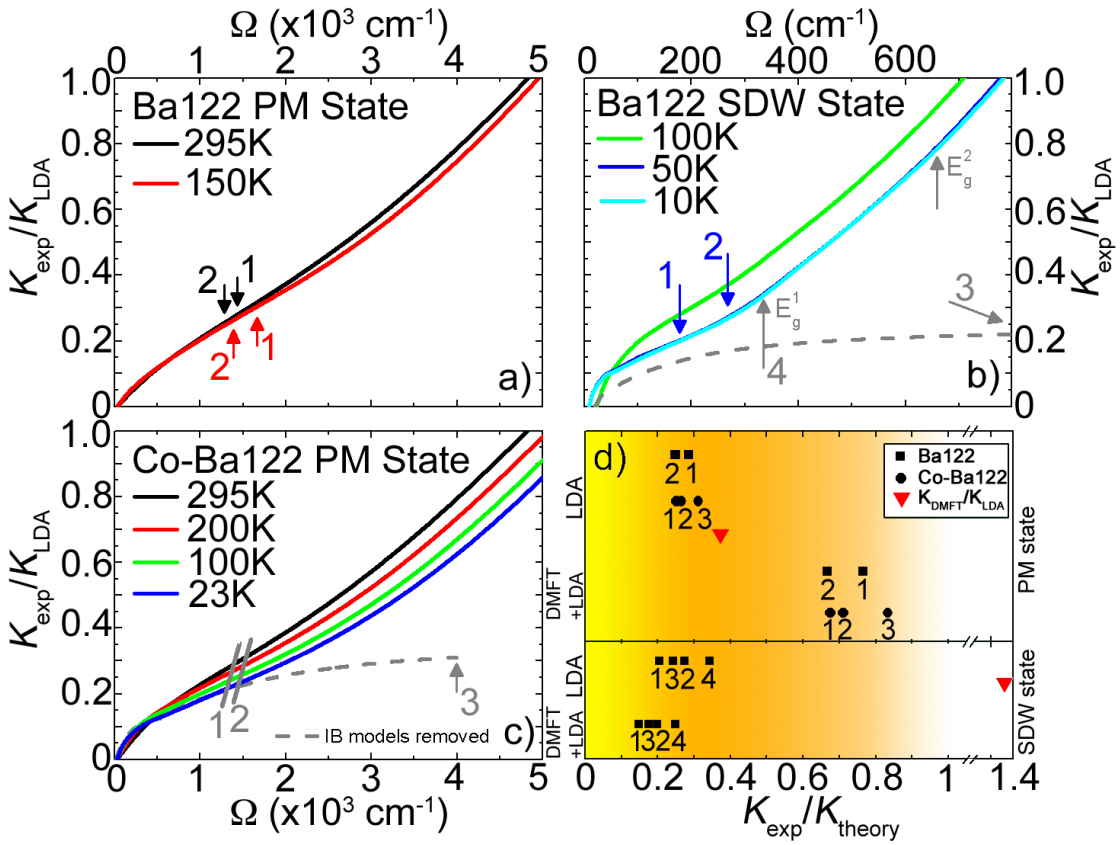

Figure 4.2: Panels A-C: The kinetic energy ratio $K_{exp}(\Omega)/K_{LDA}$ in Ba122 and Co-Ba122, as a function of integration cutoff value Ω (Eq. 1). The ratio for Ba122 in the PM (panel a) and SDW (panel b) states, and for Co-Ba122 in the normal PM state (panel c). The numbers and arrows indicate the results of the four methods for determining the kinetic energy integration cutoff, described in the Appendix. Panel D: The temperature averaged results of the kinetic energy ratio $K_{exp}(\Omega)/K_{theory}$ in the PM and SDW states, compared with both LDA and LDA+DMFT results, including the theoretical kinetic energy values. The triangles show the value of the ratio of the two theoretical kinetic energies determined via LDA and LDA+DMFT in the PM and SDW state. The values from theory are: K^{PM}_{LDA}= (21133 cm-1)^2, K^{SDW}_{LDA}= (6937 cm-1)^2, K^{PM}_{DMFT}= (12905 cm-1)^2, and K^{SDW}_{DMFT}= (8147 cm-1)^2.

We utilize this approach in the pnictides by monitoring the energy scale of SW transfer in $\sigma_1(\omega)$.

4.3 Spectral weight transfer

In Figure 4.3, we plot the ratio of the integrated SW at low temperature $K_{exp}(T, \Omega)$ to the room temperature value $K_{exp}(295K, \Omega)$, where the cut-off value Ω extends throughout the entire measured frequency range. This ratio emphasizes the relevant energy scale of SW transfer. If there is a transfer of SW from high to low energy, the SW ratio will exceed 1 at low energy and then smoothly approach 1 until the full energy scale of the Drude oscillator is reached. If there is a transfer of SW from low to high energy, the SW ratio will fall below 1 until the total energy scale of SW transfer is reached.

We now discuss the SW ratios in the PM state (Fig. 4.3). As temperature decreases, the Drude response narrows and some SW shifts lower in energy. This is in accordance with expectations for a metal and causes the SW ratio to exceed 1 below $\approx$ 600 cm^{-1}. Yet between $\approx$ 600 - 8000 cm^{-1}, the ratios decrease to well below 1. There is a minimum in the PM state ratios near 3000 cm^{-1}, indicating a turning point in SW transfer: below this value, SW is depleted while above this value, SW is amassed. By $\approx$8000 cm^{-1}, the ratios return to $\approx$ 1 as all of the SW is recovered. Therefore, SW is transferred from the Drude response into the region between 3000 - 8000 cm^{-1} in both Ba122 and Co-Ba122. The energy scale of SW transfer is determined by observing the energy range over which most of the spectral weight is recovered, marked in Fig. 4.3 with vertical dashed lines. By this criterion, the energy scale for correlations in the PM state is $\approx$8000 cm^{-1}.

In the SDW state in Ba122, we observe the superposition of two concomitant processes each with its own energy scale of SW transfer. The energy scale relevant for correlations in the PM state persists in the SDW state. In addition, there is SW transfer at lower energies, consistent with the formation of the SDW gaps. When the SDW state forms, a peak in $\sigma_1(\omega)$ emerges at finite frequency. Therefore, the SW in the remaining Drude response plus the SW in the SDW peak should

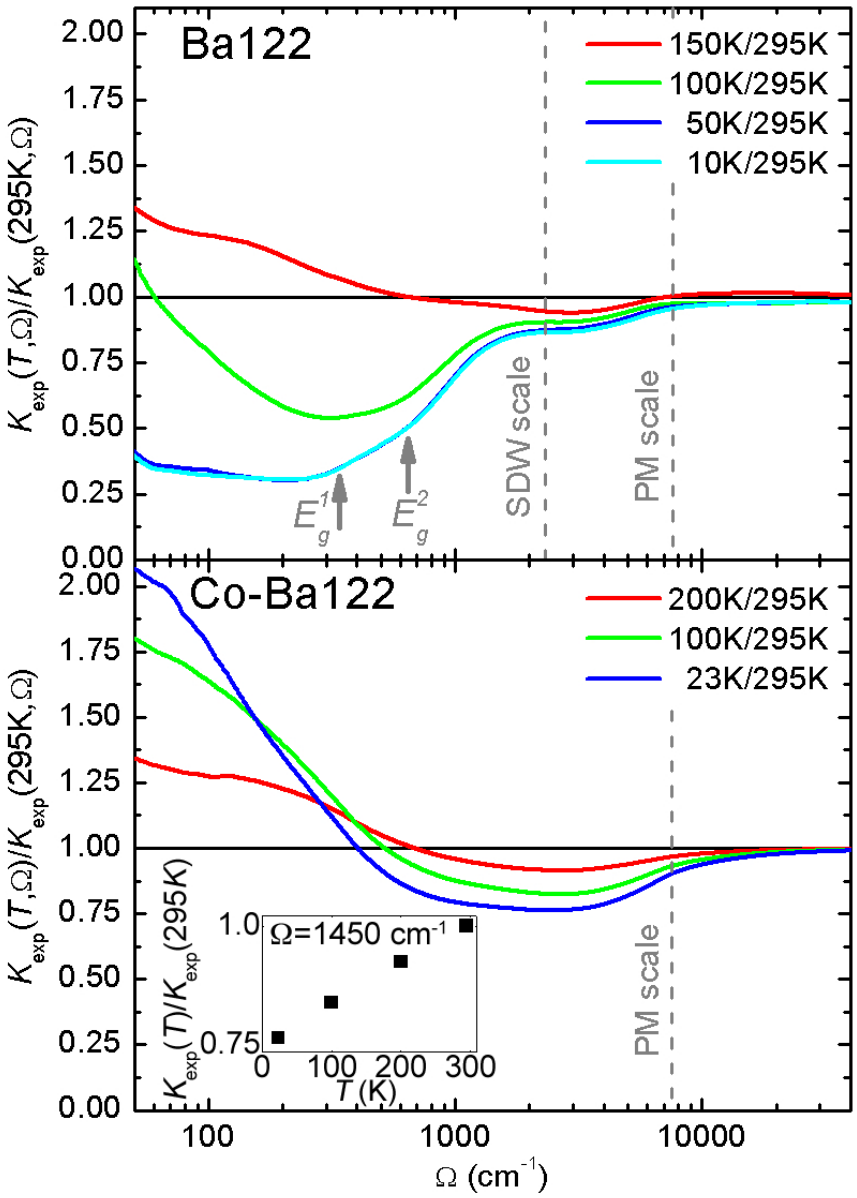

Figure 4.3: Ratio of the integrated conductivity $K_{exp}(T,\Omega)/K_{exp}(295K,\Omega)$ as a function of cutoff value Ω and temperature over the entire measured frequency range in Ba122 (top panel) and Co-Ba122 (bottom panel). The ratios are taken with respect to the $T = 295$K data in order to display the temperature evolution of the PM and SDW SW transfer. The two vertical dashed bars show the energy scale below which all of the SW transfer takes place, for both the PM and SDW states. The energy scale of SW transfer in the PM state is ≈ 8000 cm^{-1} and in the SDW state is ≈ 2000 cm^{-1}. Inset: Temperature dependence of the kinetic energy of the Drude response, normalized to the room temperature value, at a cut-off Ω=1450cm^{-1}.

be equal to the SW in the Drude response in the PM state. This is the case in Ba122, exemplified in Fig. 4.1 (top panel) where we show that in order to recover SW equal to the Drude response in the PM state, the integration cut-off must be equal to the frequency where the SDW peak returns to the PM state value ($\Omega \approx$ 2000 cm^{-1}). Therefore, we contend that the SW transfer in the SDW state can be understood as a superposition of two processes: the gapping of states due to SDW order, restricted to energies below $\approx$ 2000 cm^{-1}, and SW transfer from low to high energy over the same energy scale as in the PM state, extending to energies as high as $\approx$ 8000 cm^{-1}. This shows that the SDW state does not introduce additional electronic correlations in Ba122.

Having determined the energy scale of SW transfer, we are now in a position to compare our observations with the energy scales potentially relevant for correlations in the 122 materials: the Hubbard U and Hund's coupling J. Experimentally, x-ray absorption spectroscopy (XAS) can directly access the magnitude of U and J. A recent work determined that in Ba122, $U \leq$ 2eV $\approx$16000 cm^{-1} and $J \approx$ 0.8eV $\approx$6400 cm^{-1} (68) while other XAS experiments determined, for a broad class of pnictides, that U=3-4eV$\approx$24000-32000cm^{-1} and $J \approx$ 0.8eV $\approx$6400 cm^{-1}, in agreement with constrained DFT calculations ((69) and references therein). In LDA+DMFT calculations, including those that produce an optical conductivity closely resembling our data (65), the interaction strengths were U = 3 - 5 eV and J = 0.6 - 0.9 eV $\approx$ 3,600 - 7,200 cm^{-1} (69; 70; 71). On the other hand, mean field theory results suggest an intermediate value of U=2-4 eV (72), while a multiorbital Hubbard model under the mean field approximation gives $U\approx$1.5 eV and $J \approx$0.3-0.6 eV (73).

All of these results point to a picture where $U \approx$2-5eV while J is some fraction thereof: $J \approx$0.6-0.9 eV. Comparing the values of U and J with our SW data, it is clear that the Coulomb scale $U \approx$ 2-5 eV is larger than the observed SW transfer in our samples (74), especially considering the fact that the bulk of the literature we reviewed leans towards the larger value of U within the above interval. Moreover, as demonstrated, SW does not significantly change with doping, while in a Mott insulator the effective number density of carriers increases linearly with

doping.

Of additional importance is the *direction* of SW transfer. In most strongly correlated metals derived from Mott insulators, the Drude oscillator strength grows at lowered temperatures due to SW transfer from high to low energy, over an energy scale of the Hubbard $U/2$ (75). (An example of this behavior can be found in the electronic response of V_2O_3 in the high-temperature metallic state (66; 76).) SW transfer in the cuprates, while not universally true in the most underdoped compounds, is generally from high to low energy with decreasing temperature, over an energy scale associated with U (77; 78; 79; 80) (see the Appendix for more references and a detailed discussion of this point). Therefore, we find that for systems where the Coulomb repulsion U defines the correlation scale, SW transfer is from high to low energy as temperature is decreased, resulting in a larger Drude response at low temperature. The situation in the 122 pnictides is quite different, where the SW transfer at low temperature is from *low to high* energy. As can be readily observed in the Fig. 4.3 inset, SW in the Drude response *decreases* as temperature is lowered (81; 82). Such behavior is reminiscent of doped semiconductors and sets the pnictides apart from correlated metals derived from Mott insulators.

By studying both the direction and energy scale of SW transfer, the evidence weighs in favor of a correlation mechanism predominantly due to Hund's coupling: $J \approx 0.6$-0.9 eV, which is equal to the scale of SW transfer that we observe. These results are unexpected in light of doped Mott-insulators such as the cuprates, where electronic correlations decrease as the material is doped. On the contrary, our observation of a constant kinetic energy ratio as a function of doping is evidence against a Mott-like correlation mechanism (56). Moreover, unconventional SW transfer from low to high energy is also observed in P-doped and Co-overdoped Ba122, indicating that it may be a general phenomenon in the pnictides (83). In the future, a systematic study of detwinned samples may reveal important anisotropies (84; 85) of the SW transfer.

Note added in proof: After completion of this work, Wang, *et. al.* posted similar conclusions about the importance of Hund's coupling (86).

4.4 Appendix

4.4.1 Samples and Experiment

The samples in this study were square platelet single crystals of $BaFe_2As_2$ (Ba122) approximately 2 x 2 x 0.1 mm^3 in size, and $BaFe_{2-x}Co_xAs_2$ (Co-Ba122) approximately 4 x 4 x 0.1 mm^3 in size. The chemical composition was measured with a JEOL JAppendix-840 scanning electron microscope. Three spots were checked on the surface of each single crystal, and no impurity phases were detected. Energy-dispersive x-ray spectroscopy indicated that 8.0(5)% on the Fe is replaced by Co in $BaFe_2As_2$, thus the composition is presented as $BaFe_{1.84}Co_{0.16}As_2$. The phase purity of the crystals was characterized using a PANalytical X'Pert PRO MPD. This places the superconducting sample just beyond optimal doping, with a corresponding T_c= 22 K, measured by resistivity (87; 88; 89). In Ba122, two phase transitions have been observed as a function of temperature; a structural phase transition at T_{STR}=140K from the high temperature tetragonal (HTT) $TrCr_2Si_2$ type structure with paramagnetic (PM) order to a low temperature orthorhombic (LTO) lattice structure, and a magnetic phase transition with the onset of spin density wave (SDW) order at $T_{STR} \gtrsim T_{SDW} \approx 140$ K (62; 88; 89). In the Co-Ba122 sample, the Co-concentration is sufficient to eliminate both the structural and magnetic phase transitions observed in Ba122. Fabrication and characterization are described elsewhere (88).

We measured near-normal incidence reflectance $R(\omega)$ of the ab face, over a frequency range of $\omega \approx 20$ to 12,000 cm^{-1}. The reflectance measurements were performed for a variety of temperatures, ranging from $T = 10$ K to 295 K, normalized using an in-situ gold overcoating technique (90). Additionally, we performed variable-angle spectroscopic ellipsometry from $\omega \approx$ 5,500 to 45,000 cm^{-1}, ranging from $T = 20$ K to 295 K for Ba122 and at room temperature in Co-Ba122. In order to extract the optical constants, we performed a Kramers-Kronig constrained variational analysis using refFIT software, which utilizes a multi-oscillator fit of the reflectivity data anchored by the dielectric function measured through ellipsometry (91; 92). We also performed a Kramers-Kronig inversion of $R(\omega)$ to extract

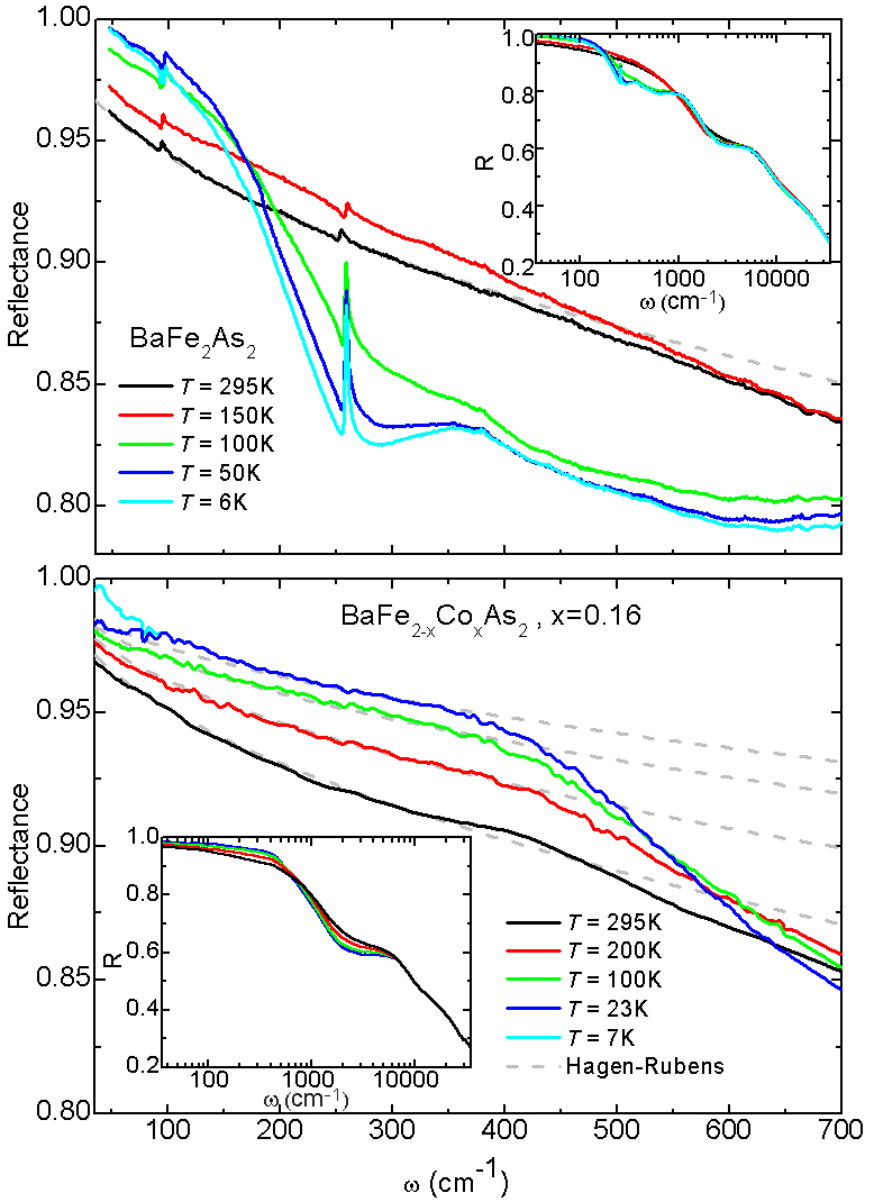

Figure 4.4: Temperature dependent reflectance of the parent compound $BaFe_2As_2$ (top panel) and the x=0.16 Co-doped superconducting compound $BaFe_{1.84}Co_{0.16}As_2$ (bottom panel). Also shown are fits to the data using the Hagen-Rubens relation for reflectivity in metals (Eq. 4.2). Insets: Reflectance extending to $\approx 45,000$ cm^{-1}, the form above $\approx 12,000$ cm^{-1} is calculated from ellipsometry.

the optical constants and obtained nearly identical results. In order to accomplish the Kramers-Kronig inversion, we included a low frequency extrapolation below $\approx$ 20 cm^{-1} of the Hagen-Rubens form (eq. 4.2). The results of the Kramers-Kronig analysis, anchored to the high-frequency optical constants determined via ellipsometry, are shown in the main text and the Appendix.

Figure 4.4 shows the reflectivity ($R(\omega)$) at various temperatures for both the parent and doped compounds. At temperatures above the T_{SDW}, $R(\omega)$ is similar between the two materials, resembling a metal with strong low-frequency magnitude ($R \geq 90\%$). For frequencies below 400 cm^{-1}, $R(\omega)$, both materials are well described by the Hagen-Rubens (HR) relation for infrared reflectivity in metals:

$$R(\omega) = 1 - (\frac{2\omega}{\pi\sigma_{DC}})^{1/2} = 1 - (\frac{8\omega}{\omega_p^2\tau})^{1/2}. \tag{4.2}$$

Here, σ_{DC} is the DC value of the real part of the optical conductivity, ω_p is the plasma frequency of the free electron response, and τ is the scattering time. The HR relation describes metals in which the dissipation of energy for electronic transport is frequency independent, based solely on the scattering rate and number density of the particles contributing to the Drude response.

As shown in Fig. 4.1, in Ba122 for temperatures $T < T_{SDW}$, a significant loss of conductivity below $\approx$ 700 cm^{-1} results in the development of a large mode at $\approx$ 1,000 cm^{-1} where $\sigma_1(\omega)$ is greater than the PM state value extending into the MIR region. Additionally, there is a smaller mode that develops near 350 cm^{-1}. As has been done previously (62; 63), we attribute these features and the increase in mid-infrared conductivity to the redistribution of spectral weight from the region of the SDW gap. We determined the two SDW gap values from the local minima in the imaginary part of the optical conductivity ($\sigma_2(\omega)$, Fig. 4.5) (93): $E_g^1 = 336 \pm 3$ cm^{-1} and $E_g^2 = 656 \pm 2$ cm^{-1}.

Values for the SDW gaps in the literature are generally determined based on the peak position in $\sigma_1(\omega)$. As compared with our method using the local minimum in σ_2, the peak in σ_1 will give a similar value for the smaller SDW gap but a very different value for the larger SDW gap. This is because, as can be seen in Fig. 4.5, the peak in σ_1 and local minimum in σ_2 correspond to nearly

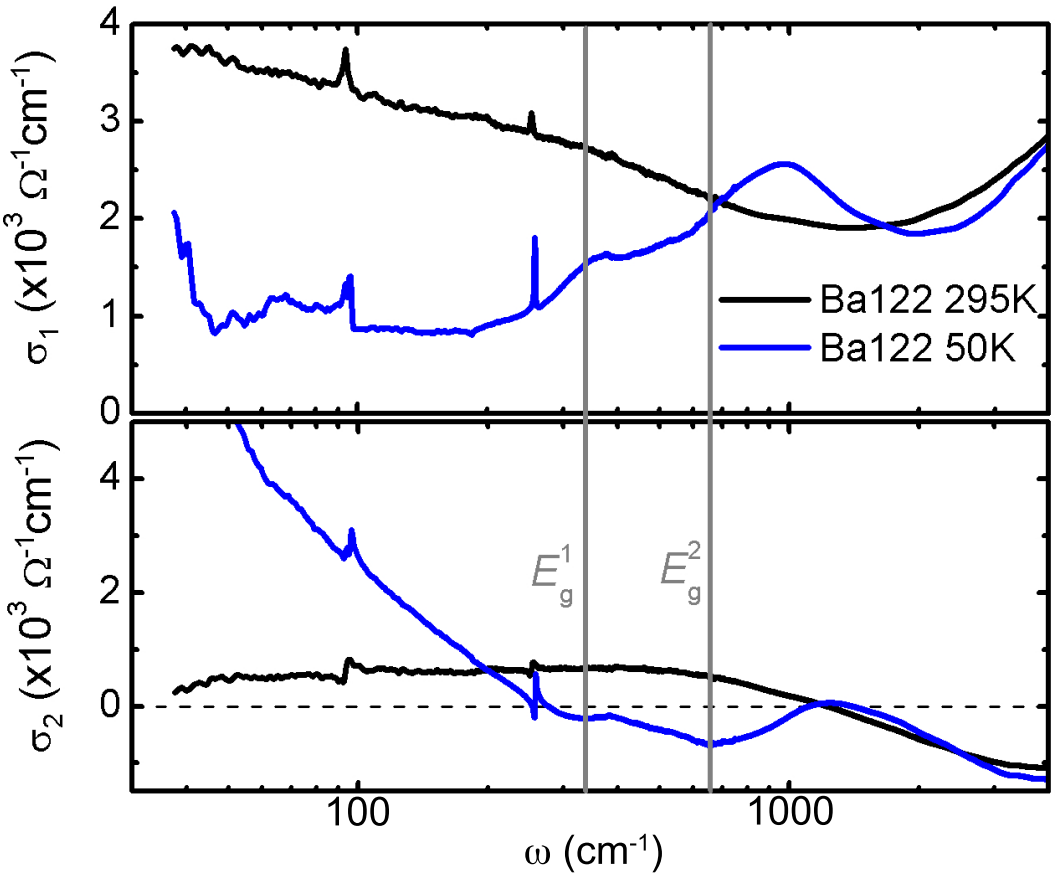

Figure 4.5: Real and imaginary parts of the optical conductivity $\sigma_1(\omega)$ (top panel) and $\sigma_2(\omega)$ (bottom panel), respectively. Two representative temperatures are shown in the parent compound Ba122 to exemplify the differences between the PM and SDW states. The SDW gaps were determined by measuring the local minima in $\sigma_2(\omega)$, shown here with vertical bars.

the same frequency for the smaller gap. On the other hand, these two features are located at very different frequencies for the larger gap. For instance, previous optical measurements (62) of the SDW gaps determined the smaller gap to be ≈ 335 cm^{-1}, in agreement with our study. However, the local maximum in σ_1 for the larger gap occurs between 860-1000 cm^{-1} (62), which is 50% larger than the gap value we determined from σ_2. Therefore, we contend that the larger SDW gap energy may have been overestimated in the literature.

4.4.2 Determination of kinetic energy

The experimental kinetic energy K_{exp} is equal to the integral of the Drude response of the real part of the optical conductivity ($\sigma_1(\omega)$) (Eq. 4.1). In practice, this integral can be performed in two ways. One can integrate up to a frequency cut-off Ω_D that is high enough to encompass most of the Drude conductivity without incorporating too much interband (IB) conductivity. Alternatively, one can model the IB contribution, subtract the model from the $\sigma_1(\omega)$ data, and integrate the remainder that is presumably only due to the Drude response. We determined K_{exp} using both methods.

Two reasonable places for the integration cut-off Ω_D are based on estimates of the upper bound of the Drude energy scale before $\sigma_1(\omega)$ becomes dominated by IB contributions. One place is the minimum value of the conductivity, $\sigma_1^{min}(\omega)$; the point between the roll-off of the Drude response and the initial increase due to IB processes and is the most common cut-off value. A second cut-off value is given by the crossover of the imaginary part of the conductivity $\sigma_2(\omega)$ from positive to negative values (this can also be thought of as the crossover of the real part of the dielectric function $\epsilon_1(\omega)$ from negative to positive values). $\sigma_2(\omega)$ will be driven negative only by IB-type processes once the majority of the Drude response is exhausted. Of course, the actual frequency position of $\sigma_1^{min}(\omega)$ and $\sigma_2(\omega)$ will be determined by the relative spectral weight and energy separation of the Drude and IB processes. In the SDW state, we used the additional criterion of the lower SDW gap E_g^1 as our best estimate for Ω_D.

As far as the IB model, for Co-Ba122 the presence of a large incoherent component of the conductivity in the PM state can be modeled as either a broad Drude or as a Lorentzian. We were guided by the spectral weight and kinetic energy analysis presented in our manuscript, as well as in the literature (94; 106; 107; 108), which demonstrate the majority, if not all of the incoherent spectral weight must be considered to be part of the Drude response. Therefore, the resultant IB model (Fig. 4.6) does not include the incoherent states that contribute to the broad Drude response. (We note that of all the methods, in the PM state there is the greatest agreement between the spectral weight found using the IB model for Co-

Table 4.1: ω_p values used for Figure 4.2 of the main text, with the corresponding method we employed. ω_p under labels 1, 2, and 4 were determined by integrating the optical conductivity up to listed cut-off value, while values under label 3 were determined by subtracting the IB model from the optical conductivity and integrating the remaining spectra.

ω_p in the PM State				
Label	1	2	3	4
Method	σ_1^{min}	$\sigma_2 = 0$	IB model	E_g^1
Ba122	11,297	10,544	-	-
Co-Ba122	10,600	10,881	11,788	-

ω_p in the SDW State				
Label	1	2	3	4
Method	σ_1^{min}	$\sigma_2 = 0$	IB model	E_g^1
Ba122	3,130	3,628	3,414	4,060

Ba122 and the LDA + DMFT approach, while in the SDW state our best estimate uses E_g^1 as the integration cut-off.)

In table 4.1, we show the values of the Drude plasma frequency ω_p, ($K_{exp}(\Omega = \Omega_D) = \omega_p^2$), and the corresponding number designation in Fig. 4.2. We note that in order to determine one value for ω_p for each method in both the PM and SDW state, we averaged the values across all temperatures corresponding with that state. (We did not, however, include the $T = 100$K value in the SDW average.) In table 4.2, we show the parameters of the dominant oscillators used to create the IB models. We do not show additional, small oscillators that were used to fit the minor features in the spectra.

Finally, we note that these results slightly underestimate K_{exp} for two reasons. First, our integrals begin at a small but finite frequency, integrating primarily from the low-energy cut-off of real data points. In our case, we began the integrals in the PM state at 30 cm^{-1} and in the SDW state at 10 cm^{-1}. This may underestimate ω_p by up to 10% in the SDW state and up to 6% in the PM state. The same error can be assumed to apply to ω_p determined from the IB models. Second, the cutoff points of our integrals in the PM state most likely do not completely account for the long decay of the incoherent Drude, which extends into the IB

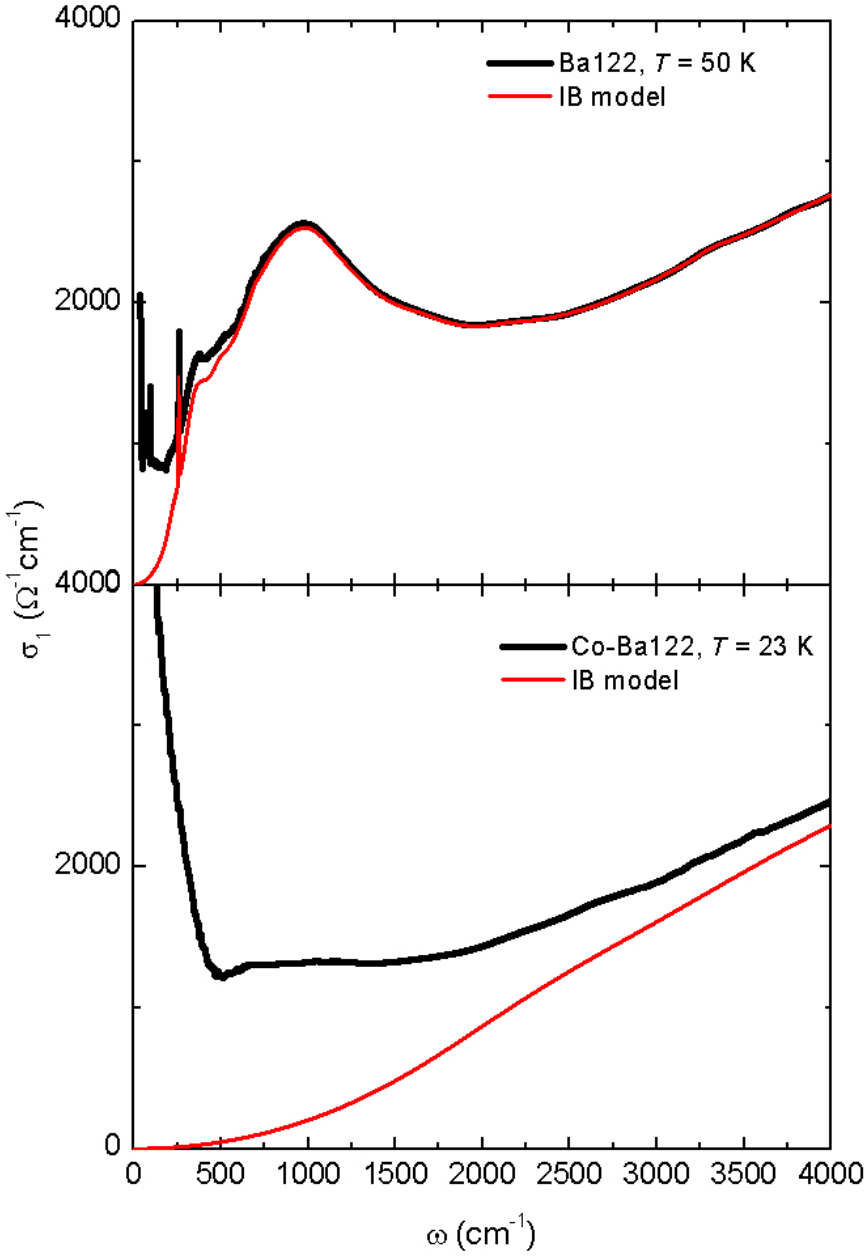

Figure 4.6: Real part of the optical conductivity σ_1 at $T = 23$K in Co-Ba122 with the modeled interband contribution. The IB model was subtracted from the σ_1 data in order to determine σ_1 due solely to the Drude response.

Table 4.2: Lorentzian oscillator parameters used to create the IB models shown in Fig. 4.6. All units in cm^{-1}.

IB parameters for Ba122			
	ω_0	ω_p	Γ
# 1	352	3000	200
# 2	921	12,700	1220
# 3	2260	6780	2000
# 4	5620	28,000	6770

IB parameters for Co-Ba122			
	ω_0	ω_p	Γ
# 1	2530	8230	2600
# 2	6200	34800	7700

region. Overall, the values of ω_p in table 4.1 likely underestimate the actual ω_p by about 10%. Therefore, we estimate the value of $K_{exp}/K_{LDA} \approx 0.4$ to be an upper bound of the kinetic energy ratio.

4.4.3 Spectral weight transfer in the cuprates

We briefly note the challenges with comparing spectral weight transfer observed in the pnictides with that of the cuprates. The direcitionality of spectral weight transfer in the cuprates is not universally from high to low energy. Indeed, the presence of the pseudogap (PG) can make it quite complicated to determine the nature of spectral weight transfer in the cuprates. It is in the underdoped cuprates that evidence is found for spectral weight transfer from low to high energy. For instance, the total spectral weight can be shown to transfer from lower to higher energy in the underdoped samples, but only below T*, and only for very specific cutoff values that emphasize the PG behavior (95; 96; 97).

On the other hand, the Bi and La based cuprates almost universally show spectral weight transfer from high to low energies. For examples of the Bi based cuprates, see (77; 79; 80; 97; 98; 99), while for La and Hg based cuprates see (78; 100; 101). We are therefore of the opinion that the bulk of the literature demonstrates spectral weight transfer in the curpates is from high to low energy,

while our present manuscript illustrates quite the opposite in the pnictides.

4.4.4 Comparison with *ARPES*

Results from angle resolved photoemission spectroscopy (ARPES) experiments also require renormalization of band theory values (102; 103; 104). The kinetic energy ratio defined for ARPES is then based on the band renormalization factor required to make band theory predictions match the measured dispersion near and at the Fermi level. (We note that this factor may be different for energies far from the Fermi level). In the PM state of Ba122 and Co-Ba122 (x = 0.06), bandwidth renormalization factors of 1.5 and 1.4, respectively, are necessary (103), corresponding to K_{ARPES}/K_{LDA} = 0.66-0.71. In the SDW state of Ba122, ARPES finds the LDA renormalization factor doubles to ≈3 (104), corresponding to K_{ARPES}/K_{LDA} = 0.33. In the SDW state, using the integration cut-off value equal to the lower SDW gap energy $E_g^1 = 336$ cm^{-1}, we find $K_{exp}/K_{LDA} = 0.34$, in agreement with the ARPES results. However, in order for optics to reproduce the ARPES results in the PM state, the integral would need to extend well into the interband region (Ω= 3500 cm^{-1}) and would no longer represent an accurate estimate of the kinetic energy. Therefore, we are faced with a disagreement between ARPES and optics in the PM state.

The discrepancy between the two probes may be due to the difference in single-particle (ARPES) and two-particle (optical) dynamics, similar to conclusions recently drawn to explain discrepancies between infrared Raman spectroscopy and ARPES in a series of overdoped cuprates (105). A second possibility is that in the PM state, the incoherent quasiparticles cause the bands measured by APRES to be very broad and diffuse. This could make an accurate estimate of the renormalization value via ARPES difficult because it is based upon a second derivative of the raw energy spectra. Indeed, the importance of an incoherent quasiparticle contribution in the PM state and the disappearance of incoherent quasiparticles in the SDW state is clear from our kinetic energy analysis as well as from results in the literature (94; 106; 107; 108). In yet a third possibility, the discrepancy may stem from the fact that twinning of crystals complicates the Fermi surface, and

may increase the Fermi surface area as measured by ARPES, subsequently leading to the underestimation of correlations in the PM state (109). What is clear from both spectroscopic probes, however, is that there is a substantial renormalization of bands in the pnictides.

4.5 Acknowledgements

This work was supported by the NSF 1005493 and the AFOSR. D. Mandrus was supported by the U.S. DOE. G. Kotliar was supported by NSF grant DMR-0906943.

Chapter 4, in full, has been submitted for publication of the material as it may appear in A. A. Schafgans, B. C. Pursley, S. V. Dordevic, S. J. Moon, A. D. LaForge, M. M. Qazilbash, A. S. Sefat, D. Mandrus, K. Haule, G. Kotliar, and D. N. Basov, "Electronic correlations and unconventional spectral weight transfer in $BaFe_{2-x}Co_xAs_2$", Physical Review Letters. The dissertation author was the primary investigator and author of this paper.

Chapter 5

Phonon splitting and anomalous enhancement of infrared-active modes in $BaFe_2As_2$

Abstract

We present a comprehensive infrared spectroscopic study of lattice dynamics in the pnictide parent compound $BaFe_2As_2$. In the tetragonal structural phase, we observe the two degenerate symmetry-allowed in-plane infrared active phonon modes. Following the structural transition from the tetragonal to orthorhombic phase, we observe splitting into four non-degenerate phonon modes and a significant phonon strength enhancement. These detailed data allow us to provide a physical explanation for the anomalous phonon strength enhancement as the result of anisotropic conductivity due to Hund's coupling.

5.1 Introduction

The pnictide high temperature superconductors display a rich phase diagram including temperature and doping dependent structural and magnetic phase transitions in proximity to the superconducting phase (60; 64; 110). Such com-

plexity has myriad observational consequences. Phonon behavior provides a unique window into the phase diagram of the pnictides and as we will show, reveals a fascinating interplay between structure, charge and magnetism. Infrared (IR) spectroscopic studies consistently showed an anomalous phonon strength enhancement at low temperatures in the 122 and 1111 families (111; 112; 113; 114), yet these studies did not observe all of the phonon modes predicted by group theory. In order to understand the origin of the phonon strength enhancement, it is necessary to experimentally distinguish each phonon mode in the orthorhombic phase. In this work, by observing all of the predicted phonon modes at low temperature, we are able to comment on the origins of the phonon strength enhancement.

5.2 Experiment

The samples in this study were square platelet single crystals of $BaFe_2As_2$ (Ba122) approximately 2 x 2 x 0.1 mm in size (88). In Ba122, two phase transitions have been observed as a function of temperature; a structural phase transition from high temperature tetragonal (HTT, $TrCr_2Si_2$ type) to low temperature orthorhombic (LTO) at T_{STR} ≈140K, and a magnetic phase transition from paramagnetic (PM) order to spin density wave (SDW) order below $T_{SDW} \approx T_{STR} \approx 140$ K (62; 88; 89). Fabrication and characterization are described elsewhere (88).

We measured near-normal incidence reflectance $R(\omega)$ of the *ab* face, over a frequency range of $\omega \approx 20$ to 12,000 cm^{-1}. The reflectance measurements were performed for a variety of temperatures ranging from $T = 6.5$ K to 295 K. Additionally, we performed variable-angle spectroscopic ellipsometry from $\omega \approx$ 5,500 to 45,000 cm^{-1}. In order to extract the optical constants, we performed a Kramers-Kronig constrained variational analysis using refFIT software, as detailed in the references (91; 92).

The optical conductivity $\sigma_1(\omega)$ is plotted in Figure 5.1. At low energy, a conspicuous Drude response is present for $T > T_{SDW}$, becoming mostly gapped at low temperature. For temperatures $T < T_{SDW}$, a significant loss of conductivity below ≈ 700 cm^{-1} results in the development of a large optical transition centered

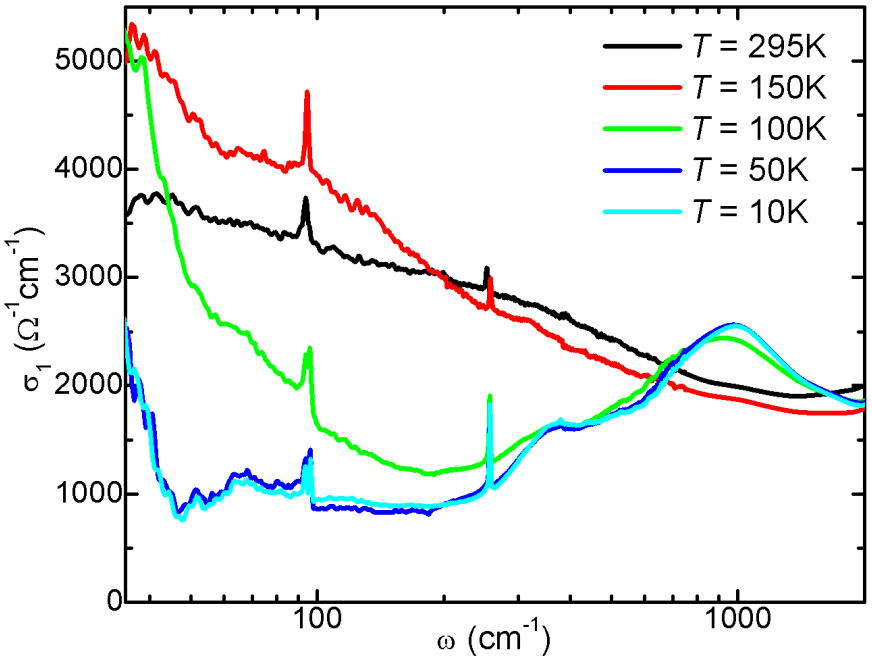

Figure 5.1: Temperature dependence of the real part of the optical conductivity $\sigma_1(\omega)$ in Ba122, focused on the far-infrared frequency range.

at $\approx$ 1,000 cm^{-1} where σ_1 is greater than the PM state value extending to 2000 cm^{-1}. Additionally, there is a smaller optical transition that develops near 350 cm^{-1}. As has been done previously (62**?**), we attribute the onset of these optical transitions to the redistribution of spectral weight from the region of the SDW gap. We determined the two SDW gap values in another work (125): $E_g^1 = 336 \pm 3$ cm^{-1} and $E_g^2 = 656 \pm 2$ cm^{-1}. Two phonon modes appear in the conductivity and are located below the lower gap energy. These phonons will be the focus of the remainder of this manuscript.

In the HTT phase, Ba122 is predicted to exhibit two symmetry-allowed *ab* plane IR-active E_u modes (115) (Figs. 5.2a and b). We observe both modes, almost identical to the recent report by Akrap, *et. al.* (111): one at 94.5 cm^{-1} due to Ba(*ab*) displacements and the other at 254.1 cm^{-1} due to Fe(*ab*) and As(-*ab*) displacements. The 254.1 cm^{-1} phonon has been observed in many of the AFe$_2$As$_2$ materials, including A = Ca, Sr, Eu, and Ba (115; 116; 117; 118), whereas the position of the phonon due to the alkali element A varies more widely. Upon the structural transition to the LTO phase below T_{STR}, the degeneracy of the two

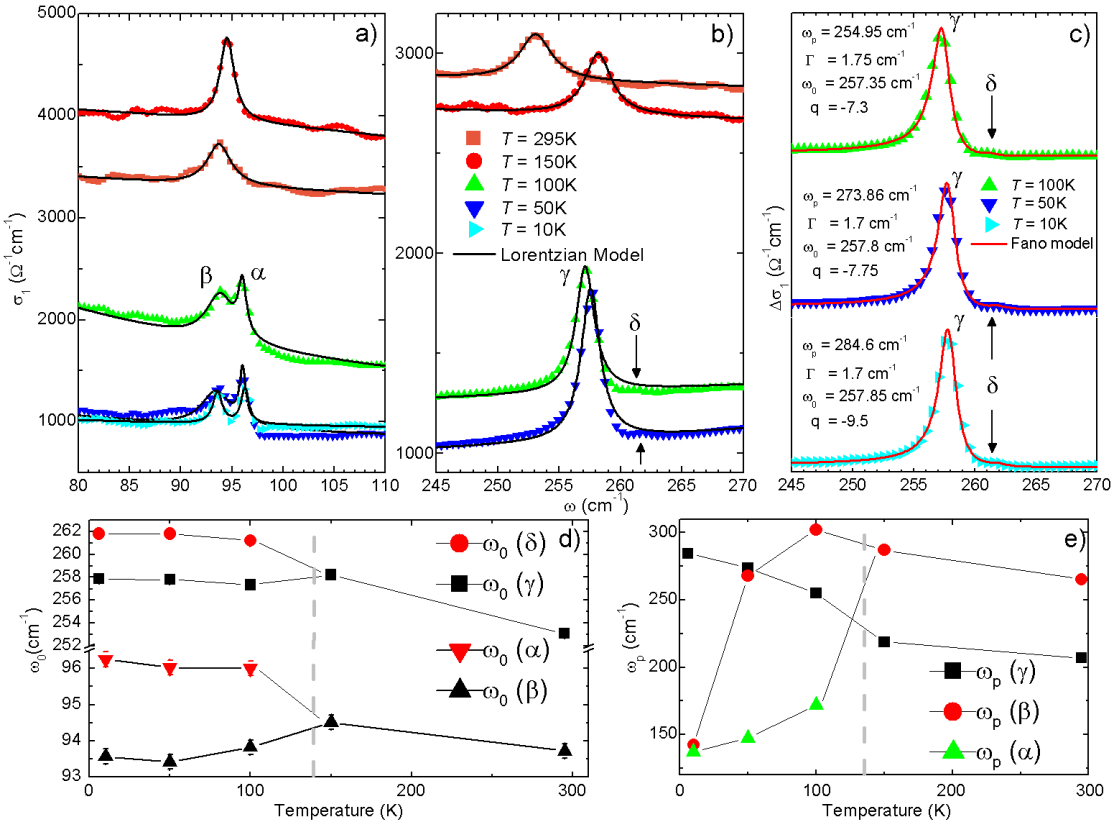

Figure 5.2: The real part of the optical conductivity $\sigma_1(\omega)$, focusing on the phonon modes in Ba122 near 95 cm^{-1} (Ba-Ba, panel a) and 257 cm^{-1} (Fe-As, panels b and c). We observe both phonon modes to split upon the transition from the HTT to LTO phases. Panels a and b show Lorenzian fits to the data, while panel c shows fits of the Fano form (Eq. 5.1) to the phonon at 257 cm^{-1}. The fit parameters are shown graphically in panel d (oscillator frequency position, ω_0) and panel e (oscillator strength, ω_p). Table 5.1 summarizes the results of our fits.

Table 5.1: The oscillator position ω_0, oscillator strength ω_p, and oscillator width Γ, based on the models used to fit the optical spectra. The error for each fit value is listed in parentheses. For the Fano oscillators, the Fano parameter is listed in Figure 5.2c.

	Ba modes					
	HTT		LTO			
	295K	150K	100K	50K	10K	
ω_0	93.7(0.3)	94.5(0.3)	93.8(0.3)	93.4(0.3)	93.6(0.3)	α
			96.0(0.2)	96.0(0.2)	96.3(0.2)	β
ω_p	265.3(10)	287.0(10)	302.3(10)	267.9(10)	142.3(10)	α
			171.7(10)	147.52(10)	137.3(10)	β
Γ	2.9(0.2)	1.7(0.1)	3.4(0.2)	3.5(0.2)	1.1(0.1)	α
			0.9(0.1)	0.7(0.1)	0.9(0.1)	β

	Fe-As modes					
	HTT		LTO			
	295K	150K	100K	50K	10K	
ω_0	253.1(0.3)	258.2(0.3)	257.4(0.3)	257.8(0.3)	257.9(0.3)	γ
			261.2(0.2)	261.8(0.2)	261.8(0.2)	δ
ω_p	207.0(10)	218.8(10)	255.0(10)	273.9(10)	284.6(10)	γ
			31.6(7)	38.7(7)	38.7(7)	δ
Γ	3.1(0.4)	2.6(0.4)	1.8(0.2)	1.7(0.2)	1.7(0.1)	γ
			1.5(0.5)	1.5(0.5)	1.5(0.5)	δ

E_u modes is broken because of the unequal a and b-axis bond lengths, becoming $B_{2u} + B_{3u}$ along the b and a axes, respectively (111). Therefore, phonon splitting is expected to occur (115), and four IR-active modes should become evident. In Figure 5.2, we show the unambiguous observation of phonon splitting using IR optics. We fit the phonons using Lorentzian oscillators, the results of which are given in Table 5.1 and plotted in Fig. 5.2. (We note that phonon splitting has been observed using Raman spectroscopy (119).)

Figure 5.2a shows the temperature dependence of the conductivity, focusing on the lower energy phonon at $\omega_0 \approx 94.5$ cm^{-1}. The mode hardens by 1 cm^{-1} upon cooling to T_{STR}, and then it splits into two distinguishable peaks. The two modes are separated by 2.9 cm^{-1}, with the lower phonon (β) centered at the original room temperature position of $\omega_0 = 94.5$ cm^{-1}. Identifying the Ba-Ba distance

with the a=5.6146$\mathring{A}$ and b=5.5742$\mathring{A}$ lattice constants in the LTO phase (120), we can use a simple equation to estimate the expected splitting of the phonon frequency $\omega_0^\alpha/\omega_0^\beta = (l_\beta/l_\alpha)^{(3/2)}$, where l is the bond length (121). This yields an expected splitting of 1.1% (1 cm^{-1}); much smaller than the observed value of 2.9 cm^{-1}. We do not observe any temperature dependence of the position (ω_0) of these two modes below T_{STR}. In the LTO phase, just below T_{STR}, the combined oscillator strength of the α and β modes (ω_p) is almost twice the HTT value. After the initial increase, the combined spectral weight is greatly reduced by T = 10K. This strange behavior of the combined spectral weight may be due to the width of the modes becoming resolution limited at low temperature. However, to our knowledge, no previous report has found any change in the spectral weight of the Ba-Ba mode across the structural phase transition. This may be due to the fact that splitting of this mode has not previously been reported.

Below T_{STR}, the Fe-As mode (Fig. 5.2b) gains substantial strength. Our observations indicate that both the 94.5 cm^{-1} and 254.1 cm^{-1} modes experience significantly enhanced total oscillator strength in the LTO phase. We observe evidence of the Fe-As phonon splitting, with a weak higher energy phonon (δ mode) at 261.8 cm^{-1}. Identifying the Fe-Fe bond length as 2.808 and 2.787 $\mathring{A}$ (120), the expected orthorhombic splitting of 1.13% is close to the observed splitting of 1.5% $\pm$ 0.2% (3.9 cm^{-1}). The fact that the γ-mode moves downward in energy below T_{STR} while the δ-mode remains at higher energy naïvely implies that the γ-mode corresponds to the longer of the two bond lengths. As we will discuss later, the γ-mode is in fact observed to result from the shorter b-axis bond length. Additionally, we performed similar measurements in the Co-doped superconducting compound $BaFe_{1.84}Co_{0.16}As_2$. There is no phonon strength enhancement at low temperatures in the doped compound (Figure 5.3), supporting the notion that the particular properties of the LTO and SDW phases are required to produce the phonon strength enhancement.

5.3 Phonon asymmetry and the Fano model

Lattice phonon modes generally result in a Lorentzian lineshape, symmetric about a central frequency. Coupling of the phonon to a continuum of charge and spin excitations produces an asymmetric lineshape. The theoretical foundation for describing such coupling was developed initially by Fano (123). Written in terms of the optical conductivity (124), the Fano oscillator is a modified form of the standard Lorentz oscillator:

$$\sigma_1(\omega) = \frac{\omega_p^2}{60\Gamma} \frac{q^2 + \frac{2q(\omega-\omega_0)}{\Gamma} - 1}{q^2(1 + \frac{4(\omega-\omega_0)^2}{\Gamma^2})}, \tag{5.1}$$

where q is the Fano parameter which provides asymmetry, ω_p is the oscillator stength, ω_0 the central frequency, and Γ is the broadening of the oscillator. We determined that a Lorentzian oscillator was insufficient to accurately describe the lineshape of the 258 cm^{-1} phonon in the SDW state and instead modeled this mode using the Fano oscillator (Fig. 5.2c). We find a small but measurable asymmetry, resulting in a modest Fano parameter value, which decreases as the temperature is lowered. The decrease in asymmetry can be understood by considering that in the gapped state, the coherent electronic states are continuously reduced as the temperature is lowered. Such depletion of the coherent quasiparticles results in a smaller coupling of the phonon mode to the coherent electronic states. Yet, as q grows in magnitude and the lineshape becomes more symmetric, we do not see a corresponding decrease in the mode intensity. After considering many scenarios for both phonon strength enhancement and coupling with the electronic background that decreases at the lowest temperatures, we have identified only one possible explanation.

5.4 Phonon enhancement due to Hund's coupling

Hund's rule coupling has been shown to be very important for understanding the strong correlations in the pnictides (65; 125; 126). In addition to correlations, Hund's coupling results in very anisotropic electronic conductivity (Drude response) (65; 85). Recent polarized infrared studies of detwinned Ba122 crystals

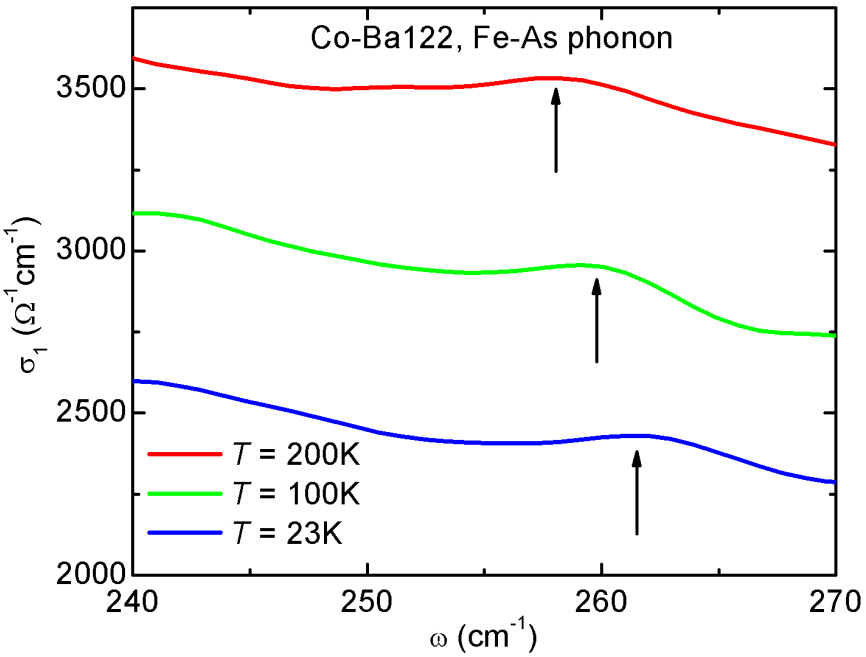

Figure 5.3: Temperature evolution of the 257 cm^{-1} phonon mode in Ba122. We find this mode to evolve monotonically with temperature and to be just above the noise floor of our measurement for temperatures at 200K and below.

(84; 127; 128) have observed drastically anisotropic optical conductivity between the a and b axes. The Drude response is significantly reduced and the Fe-As phonon enhanced for b-axis polarization while for a-axis polarization, the Drude response remains much stronger and the Fe-As phonon is diminished (128). It has been shown (122) that both the magnetic moment and the anitferromagnetic wavevector are along the a-axis while the ferromagnetic wavevector aligns with the b-axis. The Pauli exclusion principle favors conductance along the antiferromagnetic direction, and therefore the primary conductance channel is aligned with the a-axis while conductance along the b-axis is suppressed (65; 85; 128).

For a phonon coupled to the free electron response in an orthorhombic crystal such as Ba122, anisotropic conductivity will result in additional screening of the mode in the direction of preferred conductance, leading to a reduction in the oscillator strength. Along the suppressed conductivity direction, one would expect an enhancement in the phonon strength due to the lower electronic screening. Furthermore, the phonon should become more symmetric at the lowest temperatures

as the continuum of Drude states are progressively gapped by the SDW order. This is precisely the situation we observe. Therefore, we conclude that the anomalies of the spectral weight of the γ- and δ-modes is caused by anisotropic conductivity due to Hund's rule coupling. Our results uncover yet another anomaly: since the enhanced phonon is polarized along the shorter b-axis, one would expect its resonant frequency to be higher than the phonon polarized along the longer a-axis. The observed frequency dependence of the phonon modes is a reversal from expectations. Theoretical studies are necessary to directly address the consequences of Hund's coupling on lattice dynamics. Finally, we note that with small amounts of substitutional Co-doping, the DC conductivity anisotropy becomes enhanced (85), but the effect upon the phonon strength enhancement is unclear. We have observed that the Fe-As phonon is almost completely washed out with x=0.16 Co-doping, but an IR study of the intermediate doping regime where the LTO, SDW, and superconducting phases coexist will be crucial to address this open question.

5.5 Acknowledgements

This work was supported by the NSF 1005493 and the AFOSR. D. Mandrus was supported by the U.S. Department of Energy, Basic Energy Sciences, Materials Sciences and Engineering.

Chapter 5, in full, is a reprint of the material as it appears in A. A. Schafgans, B. C. Pursley, A. D. LaForge, A. S. Sefat, D. Mandrus, and D. N. Basov, "Phonon splitting and anomalous enhancement of infrared-active modes in $BaFe_2As_2$", Physical Review B 84, 052501 (2011). The dissertation author was the primary investigator and author of this paper.

Chapter 6

Landau levels in the three dimensional topological insulator $Bi_{1-x}Sb_x$

Abstract

We have performed broad-band zero-field and magneto-infrared spectroscopy of the three dimensional topological insulator $Bi_{0.91}Sb_{0.09}$. The zero-field results allow us to measure the value of the direct band gap between the conducting L_a and valence L_s bands. Under applied field in the Faraday geometry ($k \parallel H \parallel$ C1), we measured the presence of a multitude of Landau level (LL) transitions, all with frequency dependence $\omega \propto \sqrt{H}$. We discuss the ramification of this observation for the surface and bulk properties of topological insulators.

6.1 Introduction

$Bi_{1-x}Sb_x$ (129; 130; 131; 132) was among the first materials predicted to be a three-dimensional (3D) topological insulator (TI) (133; 134; 135; 136; 137): a material with bulk insulating properties that supports conducting two-dimensional (2D) surface states. The appearance of nontrivial topological order is intimately

tied to the band inversion that takes place as Bi is alloyed with Sb. Among the theoretical predictions now verified by experiment (138; 139; 140; 141) was for a free electron gas composed of spin-polarized quasiparticles existing at the 2D surface of the bulk 3D material, called surface states (SSs), formed when linear Dirac bands cross the Fermi energy (E_f). When a magnetic field is applied to the system, the SSs are thought to be gapped and spin-polarization destroyed due to the time-reversal breaking field.

The sample in this study was a large (≈ 1 cm^2) single crystal of $Bi_{0.91}Sb_{0.09}$ cut along the bisectrix plane (144). This is the same plane (perpendicular to the [1,1,1] plane) in which quantum oscillations due to a 2D Fermi surface (FS) were observed in magneto-transport (144; 146; 147), implying the presence of topological SSs. We measured near-normal incidence reflectance in the far-infrared (30-700 cm^{-1}) as a function of temperature and applied field. In order to determine the zero-field optical constants, we measured reflectance between 30-8000 cm^{-1} and variable angle spectroscopic ellipsometry between 4500 - 45000 cm^{-1}. We extracted the optical constants by performing a Kramers-Kronig constrained variational analysis using refFIT software, based on a multi-oscillator fit of the reflectivity data anchored by the dielectric function measured through ellipsometry (91; 57). These results were quantitatively similar to a full Kramers-Kronig inversion of the reflectivity data, which we show in the following figures.

6.2 Zero-field results

The zero-field data is given in figure 6.1 and shows reflectance at four temperatures from room temperature to 10K (top panel). Unlike Bi_2Se_3 (148), the plasma edge formed by the free electron response in $Bi_{0.91}Sb_{0.09}$ demonstrates substantial temperature dependence. At low temperatures, the lineshape of the plasma edge contains structure that indicates the presence of multiple plasma frequencies. This is partly due to anisotropic optical properties along the C2 and C3 axes, but more important is the fact that $Bi_{1-x}Sb_x$ alloys are composed of an inhomogenous Sb concentration throughout the bulk of the crystal. With an Sb concentration of

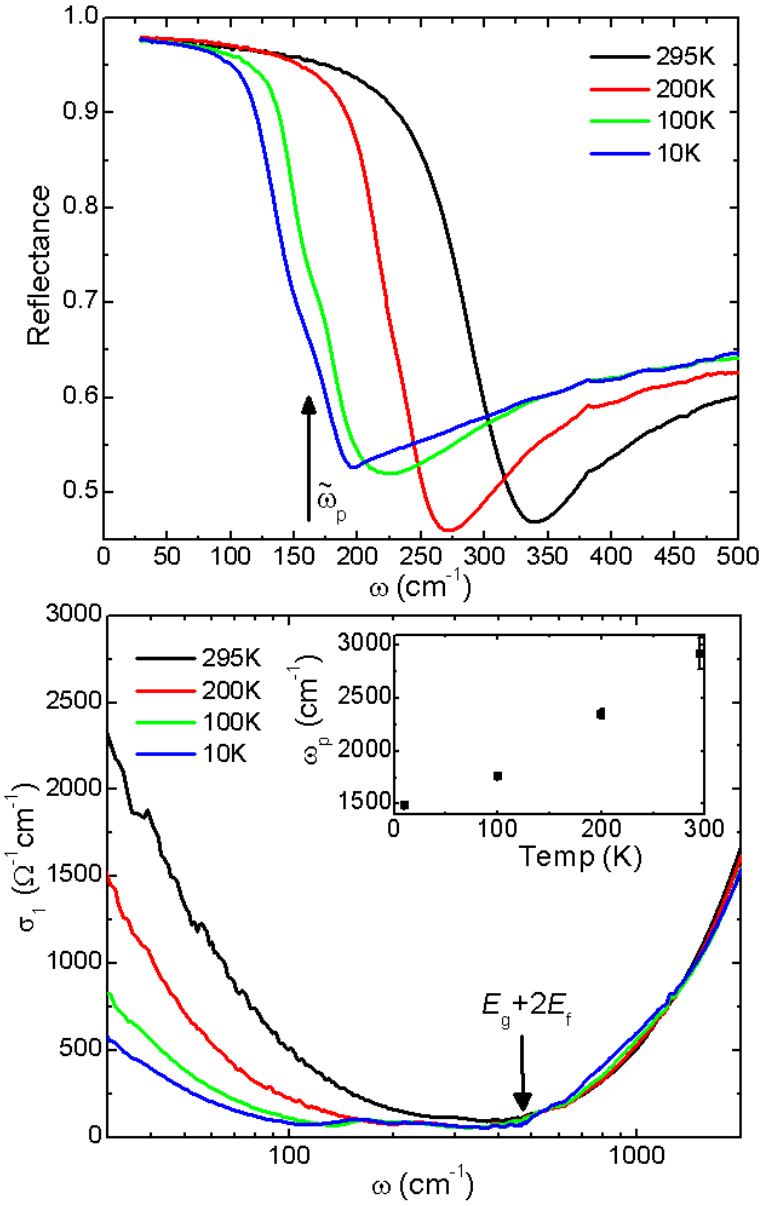

Figure 6.1: **Top**. Reflectance vs. wavenumber in the far-infrared as a function of temperature, showing the Drude plasma frequency. The screened plasma frequency $\tilde{\omega_p}(10K)$ is shown with an arrow. **Bottom**. The real part of the optical conductivity $\sigma_1(\omega)$ as a function of temperature, illustrating the decreasing Drude response at lowered temperature. The optical gap $E_g + 2E_f$ is shown with an arrow, and the conductivity rapidly increases at frequencies above the optical gap. **Bottom, inset**. The Drude plasma frequency $\omega_p(T)$ obtained from modeling the Drude response (see SM). The strong temperature dependence of $\omega_p(T)$ is likely the consequence of thermal activation.

$x = 0.09$, the alloy is a direct-gap semiconductor between the bulk L_a conduction band and the bulk L_s valence band (131). The direct band gap between the bulk L bands is measured to be E_g=48meV=387cm^{-1} and the Fermi energy is located E_f=5.37 $\pm$0.07 meV = 42.5 cm^{-1} above the bottom of the L_a conduction band (see the following discussion). This corresponds to an optical gap of $E_g + 2E_f$ = 470 $\pm$10 cm^{-1}, illustrated by the optical conductivity in Fig. 6.1 (bottom panel). Therefore, substantial thermal activation is expected, which explains the strong temperature dependence of the Drude plasma frequency ω_p, shown in Fig. 6.1 inset. (E_g is very sensitive to Sb content and above x=0.04, E_g grows with increasing Sb content (131). In slightly higher doped $Bi_{0.9}Sb_{0.1}$, a lower bound of E_g=50meV was found using ARPES (138).)

6.2.1 Loss function and inhomogeneity

Figure 6.2 shows the loss function Im$[1/\tilde{\epsilon}(\omega)]$ as a function of temperature. In simple metals with a homogenous FS, the loss function will be peaked at $\tilde{\omega_p}$ and should have a Gaussian lineshape. We find that, in spite of the intrinsic electronic anisotropy due to the crystalline structure in the bisectrix plane, the loss function is rather symmetric and is well modeled by a simple Drude at T=200K and above. Furthermore, the peak in the loss function is centered almost exactly at the screened plasma frequency $\tilde{\omega_p}$, indicating that any inhomogeneity of the plasma frequency throughout the crystal is small. As low temperature, however, the loss function strongly deviates from what a simple Drude predicts, and the peak of the loss function moves above $\tilde{\omega_p}$. The lineshape of the low temperature loss function is indicative of a distribution of plasma frequencies (5). The origin of the inhomogeneity is likely not due to anisotropic electronic properties or one would expect to observe a similarly strange lineshape at room temperature. Fully explaining the origin of this interesting behavior is currently beyond the scope of this work.

The screened plasma frequency $\tilde{\omega}_p$ is the value of the Drude plasma frequency ω_p once it is damped due to the dielectric constant at frequencies much greater than ω_p: $\tilde{\omega}_p = \omega_p/\sqrt{\epsilon_\infty}$. The value of $\tilde{\omega}_p$ is empirically determined by

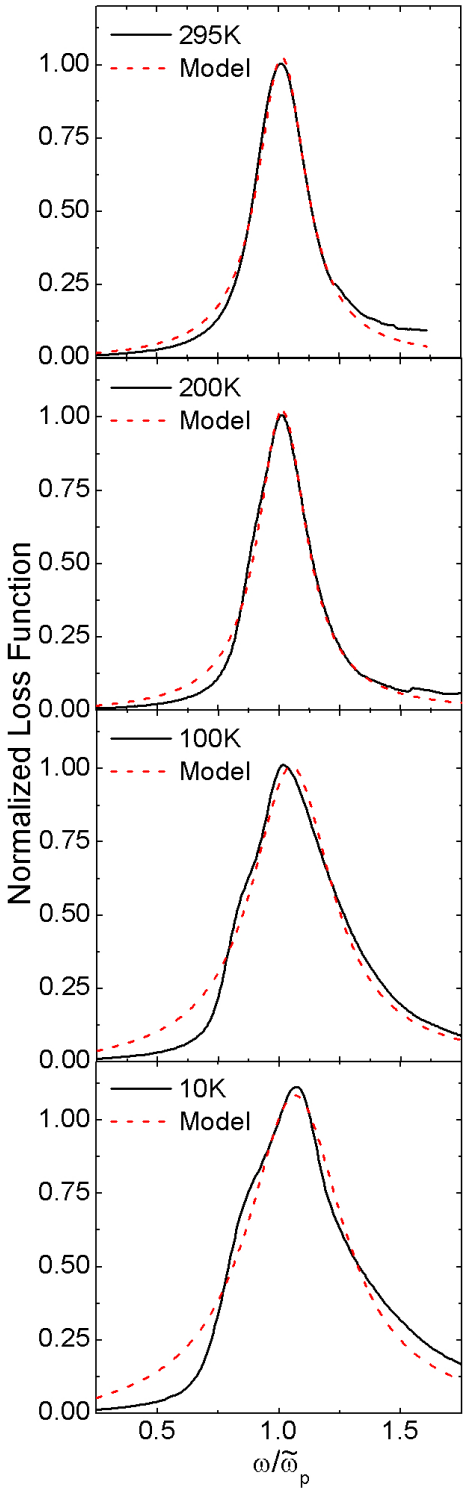

Figure 6.2: The loss function $\mathrm{Im}[1/\tilde{\epsilon}(\omega)]$ normalized to the value at the screened plasma frequency $\tilde{\omega}_p$.

observing the the frequency where $\epsilon_1 = 1$. This is complicated somewhat by the unconventional lineshape of the plasma edge at low temperature, but we find $\tilde{\omega}_p(10K) = 161$ cm^{-1}. Importantly, in order to properly account for screening effects, ω_p must be normalized by ϵ_∞ in the absence of interband transitions. In $Bi_{0.91}Sb_{0.09}$, ϵ_∞ is drastically impacted by the presence of strong interband transitions. The value that ϵ_1 would take in the absence of interband transitions can be estimated by modeling the Drude response alone, or by taking the maximum value of ϵ_1 before interband effects force ϵ_1 to return to $\approx$1 at high frequency. We call this value ϵ_D, and find that $\epsilon_D = 85 \pm 5$, in agreement with expectations from the literature (162; 163).

6.2.2 Location and size of Fermi Surface

Taskin and Ando (161) measured the volume of the bulk Fermi surface (FS), formed by a set of three ellipsoids located at the L-points of the Briullioin zone, to be $n = 8.1 \pm 0.2$X10^{16}cm^{-3}. Hall measurements yielded a similar value of the bulk 3D FS charge density $n = 1.8$ x 10^{17} cm^{-3} (161). These data were obtained with samples from the same rod as the crystal used in this study and we therefore expect the properties to be similar, within a reasonable error. The Drude model of the lowest temperature conductivity should produce comparable values between optics and transport only if the Fermi energy is located at an equivalent location in the bulk conduction band. This is because the plasma frequency of the Drude response is related to the number density of free carriers as: $\omega_p^2 = 4\ \pi n e^2/m^*$. Using the plasma frequency as measured via optics, $\omega_p = 1485$ cm^{-1}, the resulting band mass is $m^* = 0.0073 m_e$. The approximate relationship $v_f = \hbar k_f / m^*$ should provide the band velocity of the linear bulk conduction band along the fastest direction. This is because the plasma edge seen in optics is dominated by the shortest of the semimajor axes of the FS ellipoid, measured to be k_f=2.3X10^{7}m^{-1}. Therefore, the Fermi velocity in the fast direction of the bulk FS is $v_f = 3.65$ x 10^5 m/s.

Next, we invoke $E_f = \hbar k_f v_f$ in order to determine the energy difference between the bottom of the conduction band and the Fermi energy. This gives E_f

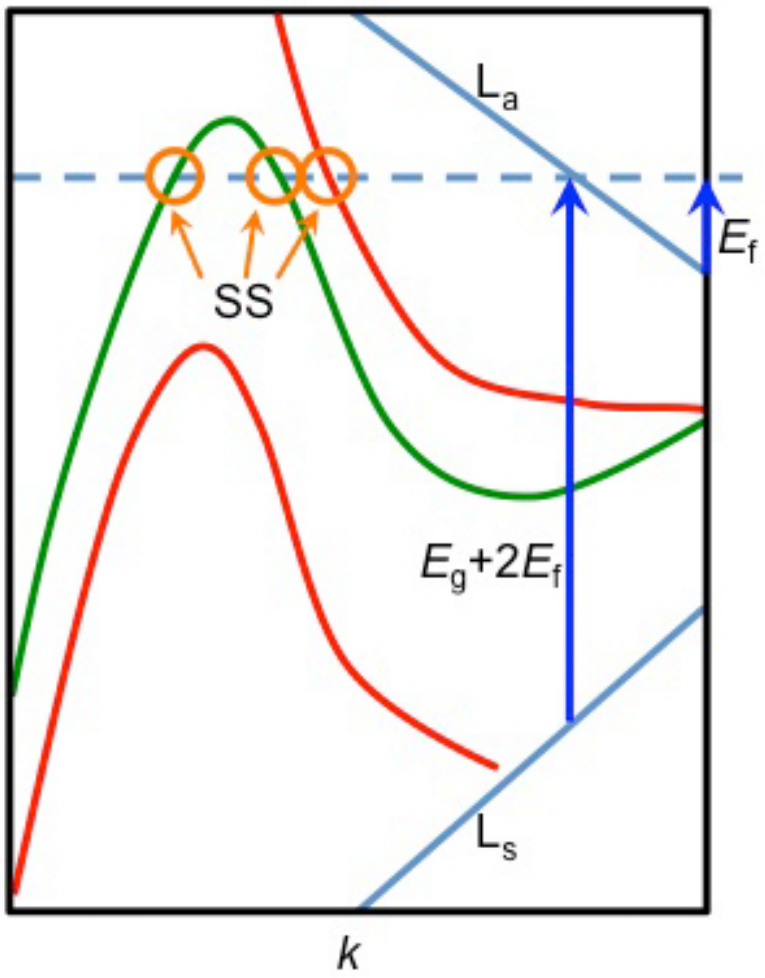

Figure 6.3: A cartoon showing the bulk L bands, the Fermi energy E_f defined from the bottom of the conduction band, the surface states formed when the surface Dirac bands cross E_f, and the necessary photon energy $E_g + 2E_f$ to create an interband transition.

$= 5.5\text{meV} = 44.5\ \text{cm}^{-1}$ above the bulk band gap, into the bulk conduction band. Based on the optical conductivity, since $E_g + 2E_f = 470 \pm 10\ \text{cm}^{-1}$, the magnitude of the bulk band gap between the L_a and L_s bands must be $E_g = 382 \pm 10\ \text{cm}^{-1}$. A cartoon of the bulk L bands and the surface states is plotted in Fig. 6.3, showing

6.3 In-field reflectance data and modeling

Turning to the in-field data, Fig. 6.4 shows reflectance in 0.1T increments at 10K (top) and 100K (bottom). The magnetic field was applied parallel to the bisectrix axis (C1), perpendicular to the bisectrix plane (C2-C3 plane), and parallel to the k-vector of the incident electric field (Faraday geometry) in order to access the previously observed 2D FS deduced from quantum oscillation (QO) measurements (144). The large LL absorptions become visible above ≈ 0.3T, which likely correspond to bulk states, as well as other smaller field-dependent features. Models of the 10K data were used to extract values of the cyclotron resonance (CR) (see below). Yet, extracting LLs from the raw reflectance is not possible for anything other than the largest LLs because the surface state charge density is very small and therefore produces exceedingly small features in reflectance. Instead, as we discuss later, differentiating the reflectance with respect to the applied field is a far more sensitive technique, allowing access the subtle features corresponding to the 2D FS that are otherwise dominated by the bulk properties in the raw reflectance.

In order to extract the cyclotron resonances from the raw reflectance, we modeled the reflectance using refFIT. The models of the 10K data are shown in Fig. 6.5, where we point out the value of the modeling result for the primary cyclotron resonance with an arrow. The models are unable to accurately track the CR as it moves through the plasma frequency, nor do they allow for the observation the much smaller LLs due to the SS bands. At fields closer to 3T, fitting converged on the presence of three CR modes. The results of the modeling are also shown in Fig. 6.7, overlaid on the data as circles.

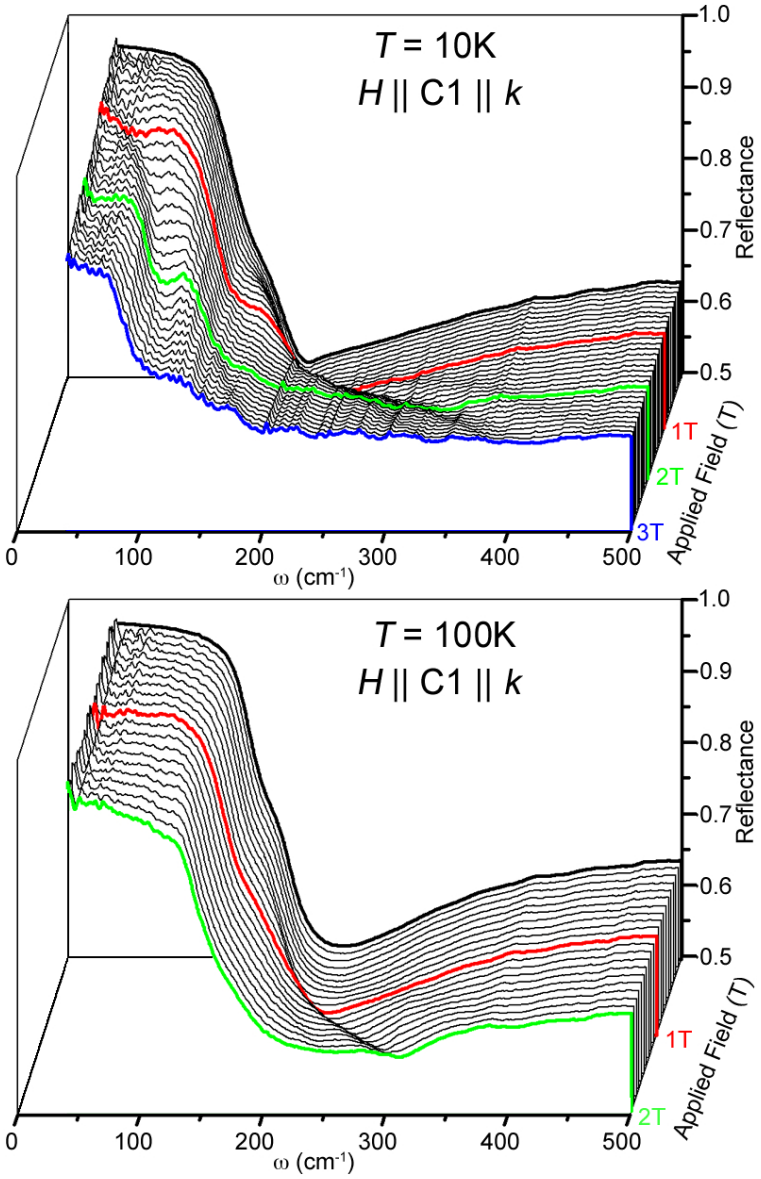

Figure 6.4: Reflectance vs. wavenumber and applied field H || C1 || k, at T = 10K (top) and 100K (bottom). Each curve represents 0.1T increment in applied field, going from 0-3T at 10K and 0-2T at 100K.

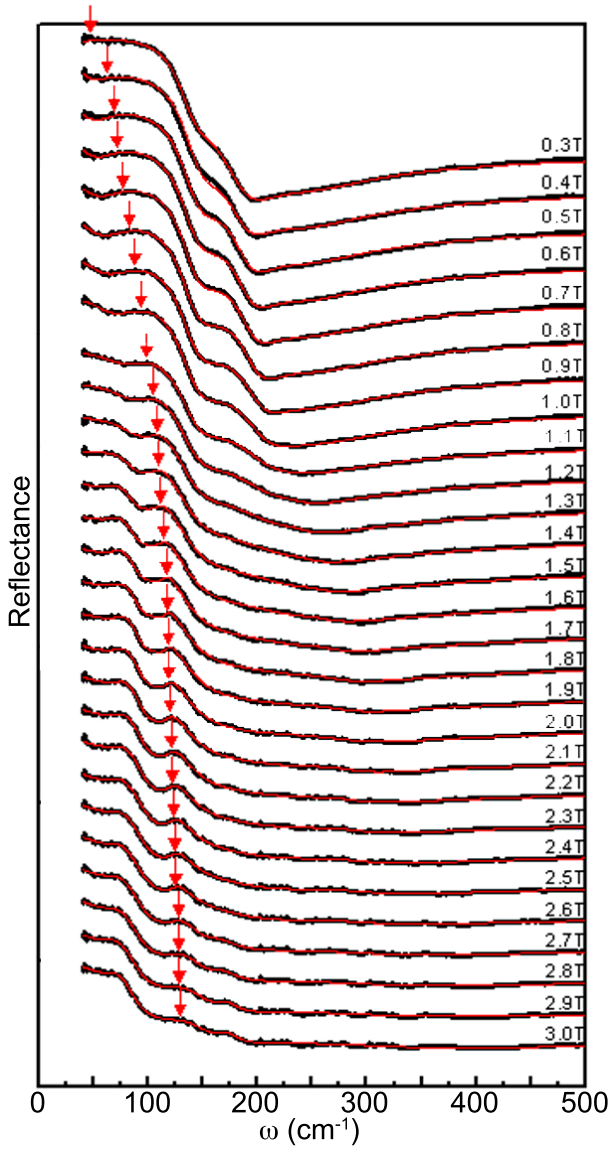

Figure 6.5: Reflectance at T=10K in 0.1T increments, overlaid with the corresponding model (red line) from RefFIT. The arrow illustrates the value of the largest resonance observed in the raw reflectance.

6.4 dR/dH contours and observed Landau levels

As previously mentioned, the most sensitive technique for extracting the LLs from the reflectance data is to perform a derivative of the reflectance with respect to the applied field: dR/dH. Indeed, these features are so small that they would have gone unobserved without utilizing this technique. Fig. 6.6 shows the dR/dH surface contour at T=10K, from ω= 40-680 cm^{-1} and H= 0-3T with 0.1T increments. The value of dR/dH corresponds to both the color and height. The intermediate field data are interpolated. As can be readily seen, there are multiple LLs, many of which are below detection in the raw reflectance data. As far as we are aware, this, and the figures that follow, are the first broadband spectroscopic maps of LLs produced in the literature.

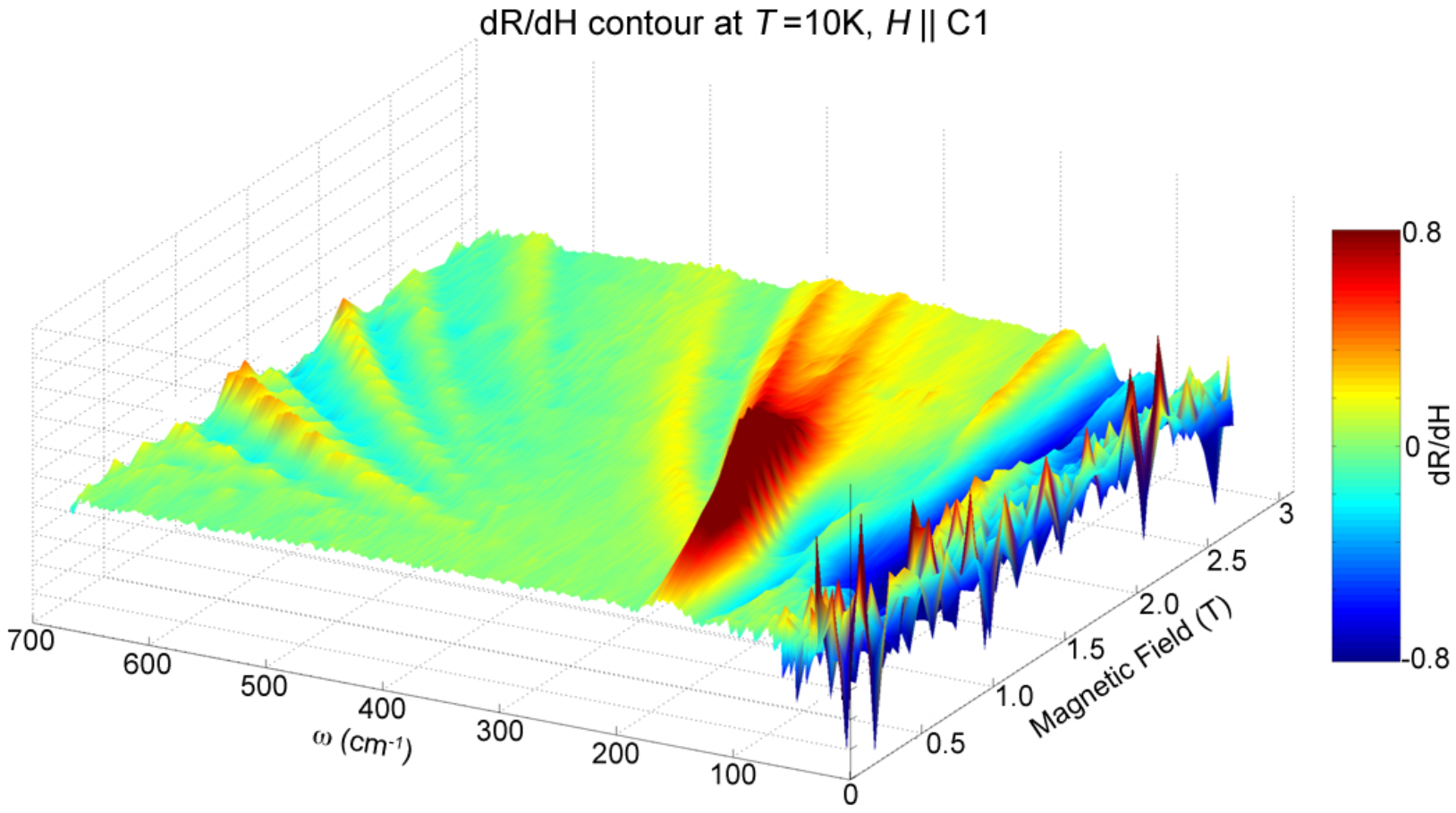

Figure 6.6: dR/dH surface contour showing the relative intensity of the LL transitions observed. The larger the feature in the dR/dH spectra, the larger the spectral weight involved in the LL.

First, we focus on dR/dH below 200 cm^{-1}, shown in Fig. 6.7. The values of the CRs extracted from modeling the raw reflectance are plotted as open circles on the dR/dH contour. Near 1.3T, the functional form of the white open circles changes abruptly and appears to saturate with increasing field. The cause of this can be understood by considering that the middle of the reflectance rolloff of the plasma edge is located at ≈150 cm^{-1}. For energies below the plasma edge, the CR will produce a dip in dR/dH, while for energies above the plasma edge, the CR results in a peak (149; 145). As the CR approaches $\tilde{\omega_p}$, the resonance must change from a dip to a peak in dR/dH. As can be seen by the open circles, modeling the raw reflectance does not accurately follow the CR once it reaches frequencies near $\tilde{\omega_p}$. The lower energy black circles indicate the presence of an additional CR that, above 1.3T, appears to disperse negatively with field. It's quite likely that the reason for this is due to the negatively dispersive cyclotron inactive mode of the plasma frequency. The low energy LL behavior is complex and can benefit from further study.

Extending the frequency range of the dR/dH plot to 700 cm^{-1}, Fig. 6.8 shows the dR/dH contour at both T= 10K (top) and 100K (bottom). A multitude of LLs are immediately apparent, as well as features (dark red) that seem to correspond to the field-dependent behavior of the bulk Drude plasma edge. All of the observed LLs at 10K, and most of the LLs at 100K, display $\omega \propto \sqrt{H}$ dependence.

6.5 Landau levels in magnetic field

Magnetic fields applied to metals will bind charged particles in orbits around the field lines, provided the mean-free path is sufficiently long. Such bound charged particles create a cyclotron resonance (CR) in optical reflectance. Since the band dispersion near E_f is quadratic in most materials, the cyclotron frequency and resultant LL transitions are $\omega_c \propto H$. As was noted early on, LLs in elemental bismuth have a non-linear field dependence due to the linear band dispersion of the L_s and L_a bands (150; 151; 152; 130). Recently, the bulk L_s valence band has

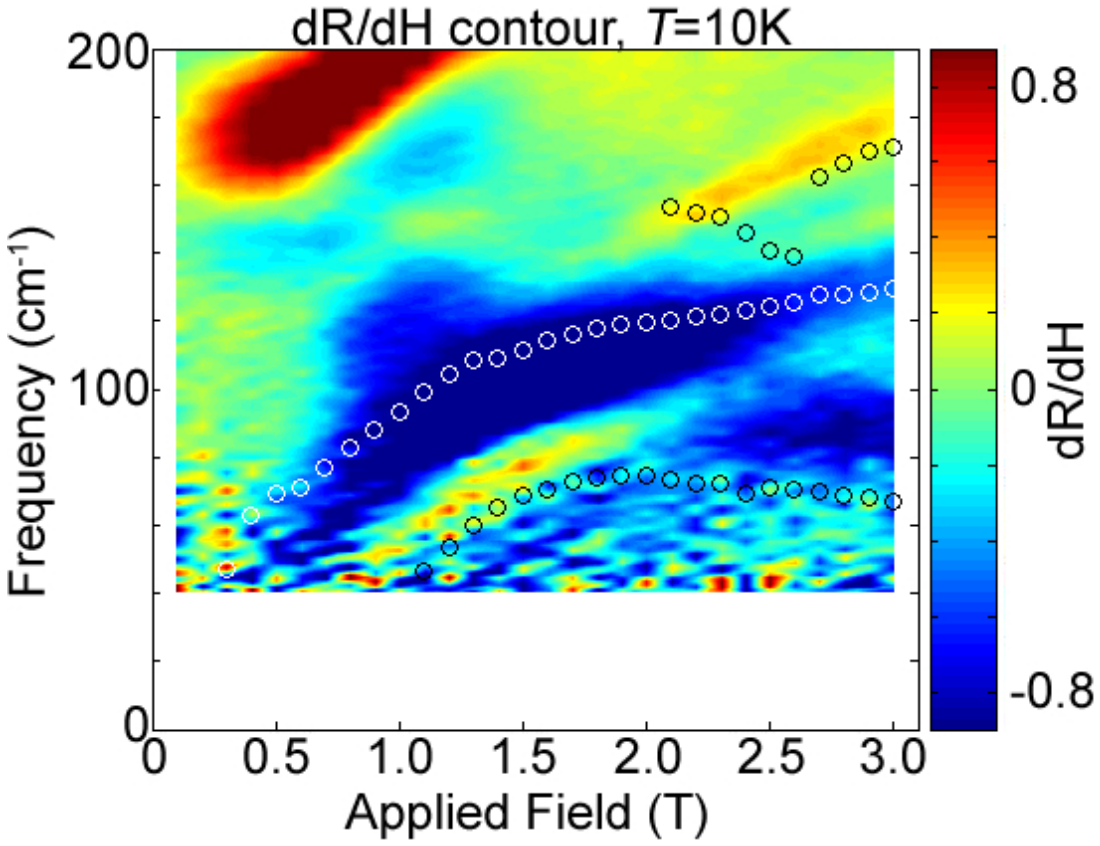

Figure 6.7: dR/dH contour illustrating the three CR modes extracted from fitting the field dependent reflectivity. The white circles correspond to the largest CR mode (as illustrated by the arrow in Fig. 6.5). The black circles show two additional modes that were converged upon by the fitting routine. The one higher in frequency likely also corresponds to the bulk CR mode, while the one lowest in energy behaves anomalously.

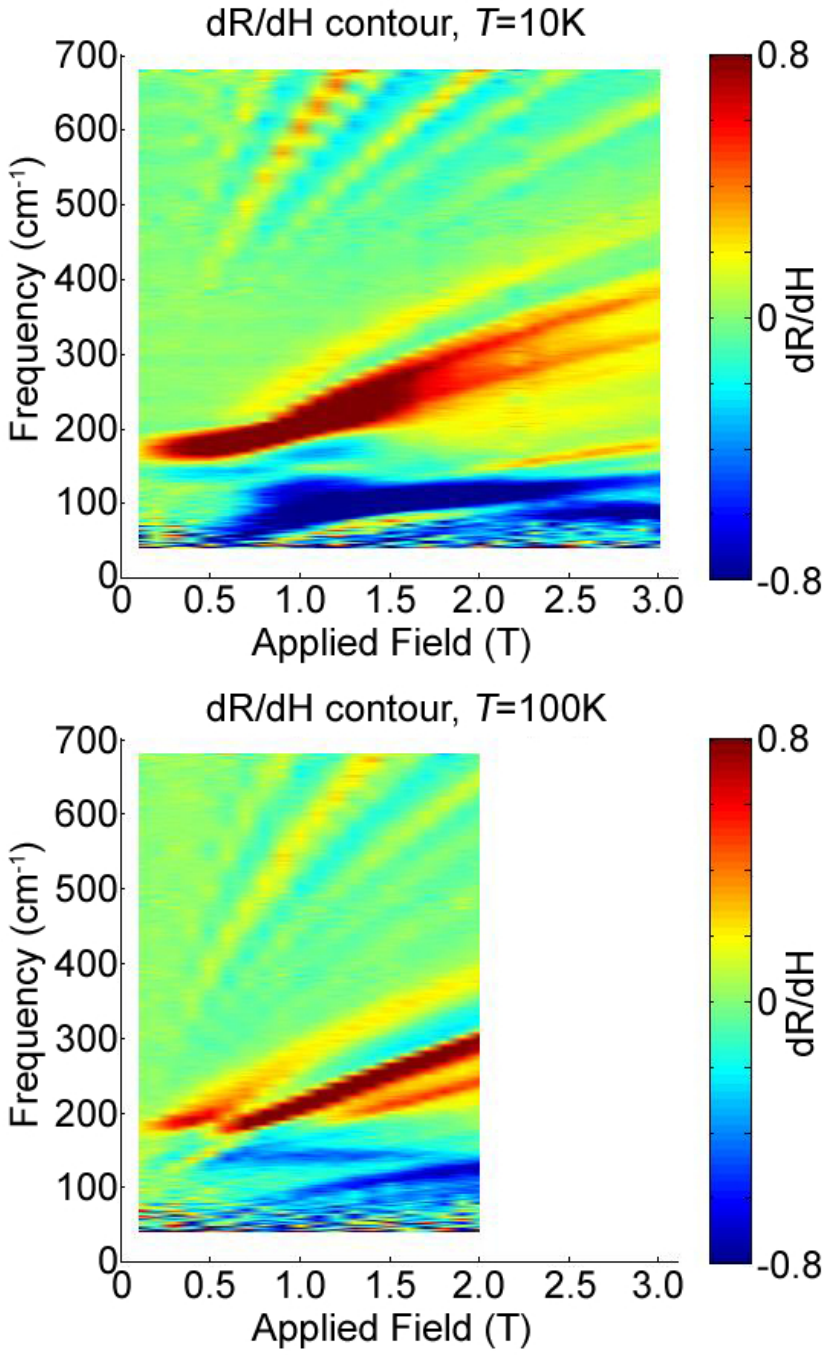

Figure 6.8: Contour plots showing the derivative of the reflectance with respect to magnetic field, dR/dH, at $T = 10$K (top) and 100K (bottom). LLs show up as peaks that disperse to higher wavenumber with applied field.

been demonstrated to be linear using ARPES (138), in addition to the observation of linear Dirac bands that form the SSs.

In order to describe the energy spectrum of the LLs due to linearly dispersive bands, one must use a model derived from Dirac theory (150; 153). For the bulk bands, the allowed energy states disperse as:

$$E = \pm(\frac{E_g^2}{4} + E_g(\frac{eH}{2m_c}(n + \frac{1}{2}) \pm \frac{g_0\mu_B H}{2\hbar}))^{1/2} \tag{6.1}$$

where μ_B is the Bohr magneton, m_c is the experimental cyclotron mass, n is the LL index of the bulk states, g_0 is the experimental g-factor, and the first $\pm$ selects a LL in the conduction (+) or valence (-) band while the $\pm$ on the last term selects the spin state. This is different from the SSs in a three dimension topological insulator, where the expression for the surface state LLs in $Bi_{0.91}Sb_{0.09}$ is:

$$E = \frac{eHN}{m} \pm \sqrt{(-\frac{eB}{2m} + \frac{\mu_B g_s H}{2\hbar})^2 + \frac{2eNHv_f^2}{\hbar}} \tag{6.2}$$

Here, g_s is the effective magnetic factor of the surface electrons, m is a correction to the effective Drude mass, N is the LL index of the SSs, and $\pm$ selects a LL above (+) or below (-) the Dirac point (158). At low fields, the LLs disperse $\propto \sqrt{H}$, but as the field increases the linear terms will dominate.

In Fig. 6.9 we plot the single particle LLs for both the bulk (Fig. 6.9, top) and SSs (Fig. 6.9, bottom). There are several important features to be learned from these figures, as far as allowed optical LL transitions. First, as can be seen in the top panel, any interband LL transitions of the bulk states will extrapolate to a value $E_g + 2E_f$ at zero-field, while bulk intraband transitions will extrapolate to zero-frequency at zero-field. Second, bulk intraband transitions are not allowed once all of the bulk conduction LLs rise above E_f. (Using the parameters mentioned in the figure caption, this takes place near 1T. Of course, using a larger effective mass means bulk intraband transitions are allowed to higher fields, and vice-versa.) Third, all of the LL transitions due to the SSs (Fig. 6.9, bottom) will extrapolate to zero-frequency at zero-field, the 0th level is almost field independent for these parameters, and there is no spin-splitting. Fourth, LL transitions will not become allowed until the LLs cross E_f, and therefore the onset

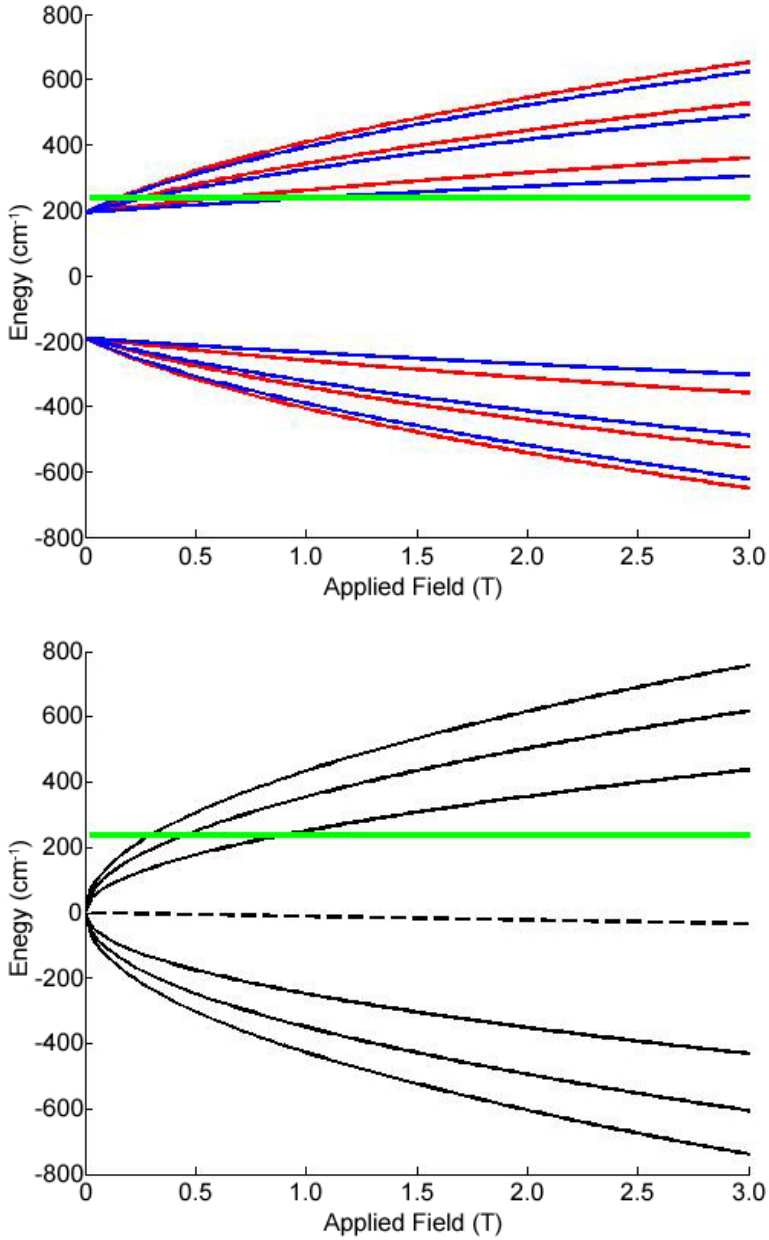

Figure 6.9: Single particle LLs as a function of frequency for the bulk (top) and SSs (bottom). The green horizontal line illustrates the location of the Fermi energy with respect to the single particle LLs (E_f= 45 cm^{-1}). The bulk LLs are spin-split, with the size of splitting determined primarily by the strength of spin-orbit coupling, which bears on the value of g_0. The red (blue) lines are spin up (down) LLs. Values used to determine the LLs are, for the bulk states: m_c=0.0073m_e, E_g=385 cm^{-1}, g_0=0.5/m_c. For the SSs, we used: m=1, g_s=80, v_f=8.5x10^5 m/s.

of optical transitions should be evident in the data. We note that the bulk band gap E_g and E_f may not be field-independent, but any field dependence should be a higher-order correction and will not significantly impact the results we show here. Also, the placement of the Dirac point, from where the surface state LLs disperse in field, may not be located in the center of the bulk band gap.

6.6 Discussion

Based on the information gained from the single particle LLs, we can make several immediate conclusions about the optical LL transitions in $Bi_{0.91}Sb_{0.09}$ presented in Figs. 6.6 and 6.8. First, none of the observed LLs extrapolate to a zero-field value equal to the bulk band gap E_g. Therefore, based on eq. 6.1, none of the LLs are due to bulk interband transitions between LLs in the L_a and L_s bands. Second, as illustrated in Fig. 6.9, if there were any intraband LL transitions due to the bulk conduction bands present, these transitions should disappear by $\approx$ 1T. Therefore, none of the LLs can be understood to be due to the bulk bands within the paradigm presented by eq. 6.1. Third, the six highest energy LLs are observed to "turn on" at finite field, consistent with the notion of LL transitions due to SS bands, once the LLs cross above E_f and transitions become allowed. The frequency at which these transitions begin provides a clue as to the separation between the upper (+) and lower (-) LLs and ultimately provides a measure of the location of the Dirac point (E_{Dirac}) with respect to E_f: the optical LL transitions will begin at $2(E_g + E_{Dirac})$, and will extrapolate to zero-frequency at zero-field. At T=10K, the transitions begin between 425-500 cm^{-1} while at T=100K the transitions begin at 350-450 cm^{-1}. At the same time, the 0-1 LL transition is seen to begin at an energy equal to 1/2 of the higher order transitions: $(E_g + E_{Dirac})$.

This somewhat conceptual understanding, however, does not yield a simple quantitative picture. For instance, applying eq.6.2 turns out to be somewhat difficult because the number of LLs is greater than what can be explained with only one Dirac band, as expected from theory. That is, while there are at least three surface state band crossings at E_f (138), only the band closest to the L-point is

thought to be a linear band while the others verge on parabolic. Therefore, such expectations dictate that only one Dirac band is giving rise to LLs with $\omega \propto \sqrt{H}$. The data, however, seem to directly contradict this notion because the total number and spacing of the LLs presented in Fig.6.8 cannot be explained by a single Dirac band.

A logical place to begin to understand the LLs is to assume that the same surface state observed in quantum oscillation measurements on nearly identical samples is also in our data. Results from QO measurements determined the presence of a 2D FS with v_f = 8.5x10^{5}m/s for very low fields (<1T) and at low temperature (144). In Fig. 6.10 we show the predicted LL transitions from SSs due to a Dirac band with a Fermi velocity of v_f^1 = 8.5x10^{5}m/s for the 0-1 (blue lines), 1-2:2-1 (black lines), and 2-3:3-2 (red lines) transitions. Additionally, we include the transitions that would exist in the presence of two additional Dirac SSs with Fermi velocities determined by fitting the LLs: v_f^2 = 6x10^{5}m/s and v_f^3 = 5x10^{5}m/s. This presents one possible physical interpretation of the origin of the weakest LLs observed. In this scenario, it's interesting that the 0-1 transitions from v_f^2 and v_f^3 are either not present or completely overwhelmed by the behavior of the plasma edge.

Finally we show that a simple model of the magnetic field dependence of the Drude plasma edge in metals (153) can reproduce the behavior of the most prominent LLs. Figure 6.11 demonstrates how the cyclotron active and inactive modes in magnetic field lead to a splitting of the plasma edge, where the cyclotron active mode moves the plasma edge higher in energy while the inactive mode suppresses the plasma edge. Qualitatively, such behavior is present in the data we present here. However, more detailed analysis is needed in order to made definitive quantitative conclusions. Furthermore, temperature and doping dependent LL studies as well as gated structures where the chemical potential can be tuned into various energy regimes of the band structure will help to further elucidate the origins of the observed phenomena we present.

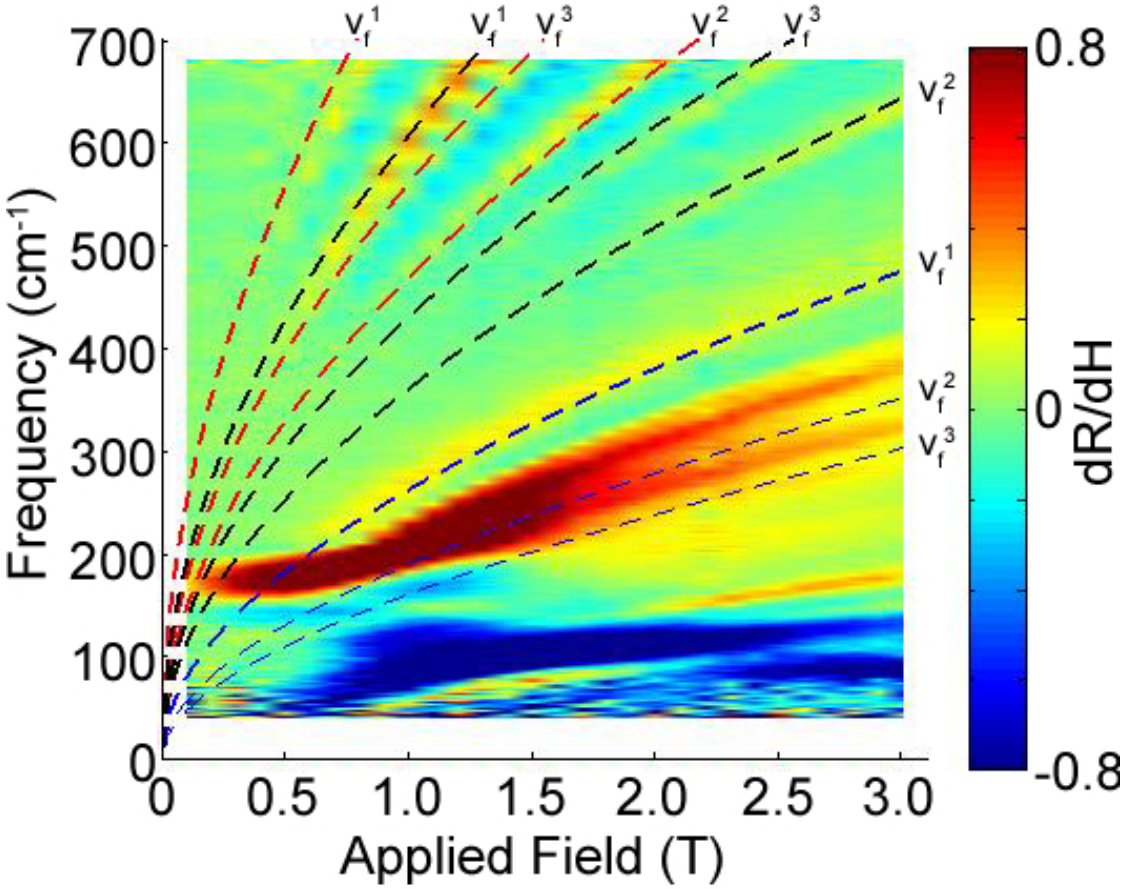

Figure 6.10: Theoretical LL transitions of the form in eq.6.2 overlaid on the data at 10K. We have included three different Fermi velocities in order to explain all of the observed LLs. As labeled, $v_f^1 = 8.5\text{x}10^5\text{m/s}$, $v_f^2 = 6\text{x}10^5\text{m/s}$ and $v_f^3 = 5\text{x}10^5\text{m/s}$ and the 0-1 (blue lines), 1-2:2-1 (black lines), and 2-3:3-2 (red lines) transitions are given. We did not correct for the Drude effective mass (m=1) and used a very moderate g-factor of the surface states (g_s=120).

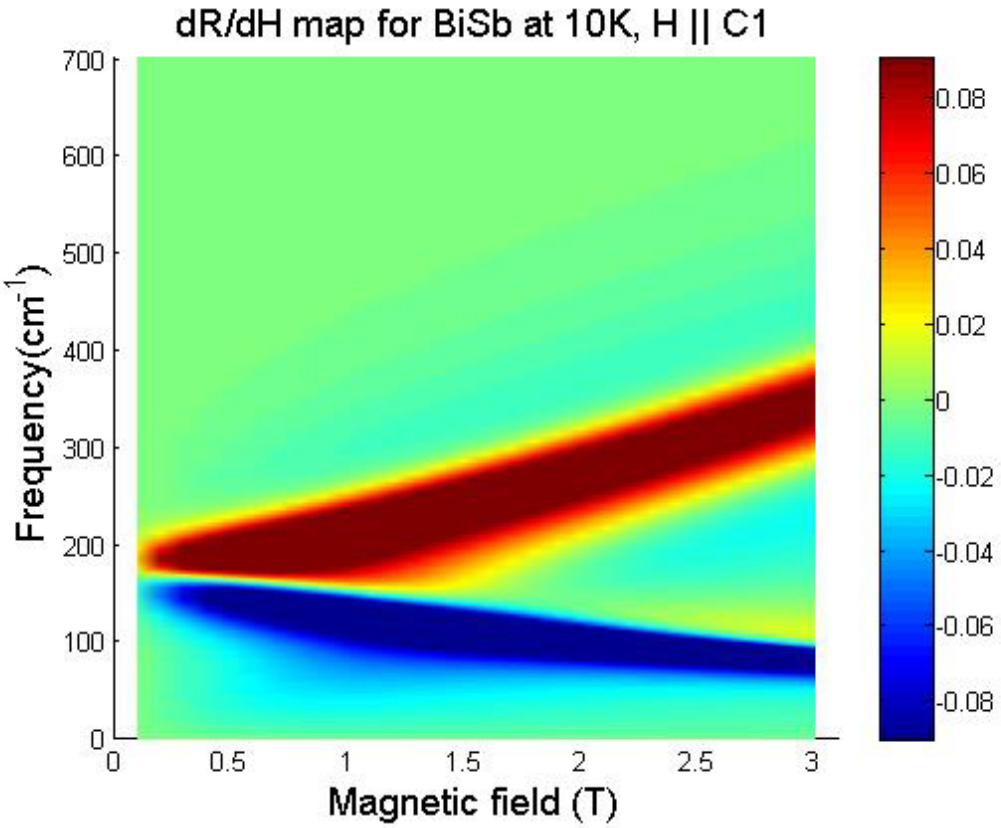

Figure 6.11: The theoretical magnetic field dependence, plotted as a dR/dH contour, of a plasma edge of a metallic semi-conductor similar to what we observe in $Bi_{1-x}Sb_x$. The quantitative similarity with the data is suggestive.

6.7 Acknowledgements

Chapter 6, in part, is currently being prepared for submission for publication of the material, A. A. Schafgans, A. A. Taskin, Yoichi Ando, B. C. Chapler, K. W. Post, and D. N. Basov, "Landau levels due to massless Dirac fermions in the topological insulator $Bi_{0.91}Sb_{0.09}$ via magneto-optics". We thank Xiao-Liang Qi, Gil Refael and Doron Bergman for enlightening discussions. Funding was provided by FENA.

Bibliography

[1] S. Sachdev and S.-C. Zhang, Science **295**, 452 (2002).

[2] Q. Li, M. Hücker, G. D. Gu, A. M. Tsvelik, and J. M. Tranquada, Phys. Rev. Lett. **99**, 067001 (2007).

[3] J. M. Tranquada, *et. al.*, Phys. Rev. B **78**, 174529 (2008).

[4] S. Tajima, T. Noda, H. Eisaki, and S. Uchida, Phys. Rev. Lett. **86**, 500 (2001).

[5] S. V. Dordevic, Seiki Komiya, Yoichi Ando, and D. N. Basov, Phys. Rev. Lett. **91**, 167401 (2003).

[6] Y. Matsuda and M. B. Gaifullin, Physica (Amsterdam) **362C**, 64 (2001).

[7] L. N. Bulaevskii, D. Domínguez, M. P. Maley, Ophelia K. C. Tsui, N. P. Ong, and A. R. Bishop, Phys. Rev. B **54**, 7521 (1996).

[8] D. N. Basov and T. Timusk, Rev. Mod. Phys. **77**, 721 (2005).

[9] Seiki Komiya, Yoichi Ando, X. F. Sun, and A. N. Lavrov, Phys. Rev. B **65**, 214535 (2002).

[10] W. J. Padilla, Z. Q. Li, K. S. Burch, Y. S. Lee, K. J. Mikolaitis, and D. N. Basov, Rev. Sci. Instrum. **75**, 4710 (2001).

[11] S. V. Dordevic, Seiki Komiya, Yoichi Ando, Y. J. Wang, and D. N. Basov, Phys. Rev. B **71**, 054503 (2005).

[12] B. Lake, *et. al.*, Nature (London) **415**, 299 (2002).

[13] Y. Ando, *et. al.*, Phys. Rev. B **60**, 12475 (1999).

[14] Y. Wang, L. Li, and N. P. Ong, *et. at.*, Phys. Rev. B **73**, 024510 (2006).

[15] Y. Wang and H.-H. Wen, Europhys. Lett. **81**, 57007 (2008).

[16] T. Suzuki, Y. Oshima, K. Chiba, T. Fukase, T. Goto, H. Kimura, and K. Yamada, Phys. Rev. B **60**, 10500 (1999).

[17] A. T. Savici, *et. al.*, Phys. Rev. Lett. **95**, 157001 (2005).

[18] S. V. Dordevic, E. J. Singley, Seiki Komiya, Yoichi Ando, E. Bucher, C. C. Homes, M. Strongin, and D. N. Basov, Phys. Rev. B **65**, 134511 (2002).

[19] A. E. Koshelev, L. I. Glazman, and A. I. Larkin *et. al.*, Phys. Rev. B **53**, 2786 (1996).

[20] L. N. Bulaevskii, A. E. Koshelev, V. M. Vinkur, and M. P. Maley, Phys. Rev. B **61**, R3819 (2000).

[21] D. Dulic, S. J. Hak, D. van der Marel, W. N. Hardy, A. E. Koshelev, Ruixing Liang, D. A. Bonn, and B. A. Willemsen, Phys. Rev. Lett. **86**, 4660 (2001).

[22] I.-J. Hwang and D. Stroud, Phys. Rev. B **59**, 3896 (1999).

[23] B. Khaykovich, S. Wakimoto, R. J. Birgeneau, M. A. Kastner, Y. S. Lee, P. Smeibidl, P. Vorderwisch, and K. Yamada, Phys. Rev. B. **71**, 220508(R) (2005).

[24] J. E. Sonier, *et. al.*, Phys. Rev. B. **76**, 064522 (2007).

[25] J. Chang, *et. al.*, Phys. Rev. B **78**, 104525 (2008).

[26] L. H. Machtoub, B. Keimer, and K. Yamada, *et. al.*, Phys. Rev. Lett. **94**, 107009 (2005).

[27] E. Demler, S. Sachdev, and Y. Zhang, *et. al.*, Phys. Rev. Lett. **87**, 067202 (2001).

[28] E. Berg, E. Fradkin, and S. A. Kivelson, Nat. Phys. **5**, 830 (2009).

[29] C. C. Homes, S. V. Dordevic, G. D. Gu, Q. Li, T. Valla, and J. M. Tranquada, Phys. Rev. Lett. **96**, 257002 (2006).

[30] A. Wollny and M. Vojta, Phys. Rev. B **80**, 132504 (2009).

[31] T. Valla, A. V. Fedorov, Jinho Lee, J. C. Davis, and G. D. Gu, Science **314**, 1914 (2006).

[32] Lu Li, Yayu Wang, M. J. Naughton, S. Ono, Yoichi Ando, and N. P. Ong, Europhys. Lett. **72**, 451 (2005).

[33] J. Corson, R. Mallozzi, J. Orenstein, J. N. Eckstein, and I. Bozovic, Nature **398**, 221 (1999).

[34] Y. J. Uemura, *et. al.*, Phys. Rev. Lett. **62**, 2317 (1989).

[35] K. Yamada, *et. al.*, Phys. Rev. B **57**, 6165 (1998).

[36] C. C. Homes, *et. al.*, Nature **430**, 539 (2004).

[37] D. N. Basov, B. Dabrowski, J. D. Jorgensen, and T. Timusk, Phys. Rev. B **50**, 3511 (1994).

[38] G. Yu, Y. Li, E. M. Motoyama, and M. Greven, Nat. Phys. **5**, 873 (2009).

[39] P. J. M. van Bentum, A. Wittlin, M. E. J. Boonman, M. Gross, S. Uchida, and K. Tamasaku, Physica C **293**, 136 (1997).

[40] A. M. Gerrits, M. E. J. Boonman, A. Wittlin, V. H. M Duijn, A. A. Menovsky, and P. J. M. Bentum, Phys. Rev. B **51**, 12049(R) (1995).

[41] A. A. Schafgans, A. D. LaForge, S. V. Dordevic, M. M. Qazilbash, W. J. Padilla, K. S. Burch, Z. Q. Li, Seiki Komiya, Yoichi Ando, and D. N. Basov, Phys. Rev. Lett. **104**, 157002 (2010).

[42] N. Ichikawa, S. Uchida, J. M. Tranquada, T. Niemöller, P. M. Gehring, S.-H. Lee, and J. R. Schneider, Phys. Rev. Lett. **85**, 1738 (2000).

[43] S. Wakimoto, *et. al.*, Phys. Rev. B **67**, 184419 (2003).

[44] A.R. Moodenbaugh, Youwen Xu, T. J. Folkerts, R. N. Shelton, and M. Suenaga, Phys. Rev. B **38**, 4596 (1988).

[45] S. Tajima, N. L. Wang, N. Ichikawa, H. Eisaki, S. Uchida, H. Kitano, T. Hanaguri, and A. Maeda, Europhys. Lett. **47**, 715 (1999).

[46] S. Tajima, Y. Fudamoto, T. Kakeshita, B. Gorshunov, V. Železný, K. M. Kojima, M. Dressel, and S. Uchida, Phys. Rev. B **71**, 094508 (2005).

[47] K. Fujita, T. Noda, K. M. Kojima, H Eisaki, and S. Uchida, Phys. Rev. Lett. **95**, 097006 (2005).

[48] J. M. Tranquada, B. J. Sternlieb, J. D. Axe, Y. Nakamura, and S. Uchida, Nature **375**, 561 (1995).

[49] A. D. LaForge, W. J. Padilla, K. S. Burch, Z. Q. Li, A. A. Schafgans, Kouji Segawa, Yoichi Ando, and D. N. Basov, Phys. Rev. Lett. **101**, 097008 (2008).

[50] A. D. LaForge, W. J. Padilla, K. S. Burch, Z. Q. Li, S. V. Dordevic, Kouji Segawa, Yoichi Ando, and D. N. Basov, Phys. Rev. B **76**, 054524 (2007).

[51] R. Liang, D.A. Bonn, and W.N. Hardy, Phys. Rev. B **73**, 180505(R) (2006).

[52] R. Daou, *et. al.*, Nature **463**, 519 (2010).

[53] V. Hinkov, D. Haug, B. Fauqué, P. Bourges, Y. Sidis, A. Ivanov, C. Bernhard, C. T. Lin, and B. Keimer Science **319**, 597 (2008).

[54] E. Berg, E. Fradkin, E.-A. Kim, S. A. Kivelson, V. Oganesyan, J. M. Tranquada, and S. C. Zhang, Phys. Rev. Lett **99**, 127003 (2007).

[55] E. Berg, E. Fradkin, S. A. Kivelson, and J. M. Tranquada, New J. Phys **11**, 115004 (2004).

[56] A. J. Millis, A. Zimmers, R. P. S. M. Lobo, N. Bontemps, and C. C. Homes, Phys. Rev. B **72**, 224517 (2005).

[57] M. M. Qazilbash, J. J. Hamlin, R. E. Baumbach, Lijun Zhang, D. J. Singh, M. B. Maple, and D. N. Basov, Nature Physics **5**, 647 (2009).

[58] D. N. Basov, R. D. Averitt, D. van der Marel, M. Dressel, and K. Haule, Rev. Mod. Phys. **83**, 471 (2011).

[59] A. Comanac, L. De' Medici, M. Capone, and A. J. Millis, Nat. Phys. **4**, 287 (2008).

[60] J. Paglione and R. L. Greene, Nat. Phys. **6**, 645 (2010).

[61] Q. Si and E. Abrahams, Phys. Rev. Lett. **101**, 076401 (2008).

[62] W. Z. Hu, J. Dong, G. Li, Z. Li, P. Zheng, G. F. Chen, J. L. Luo, and N. L. Wang, Phys. Rev. Lett. **101**, 257005 (2008).

[63] S. J. Moon, *et. al.*, Phys. Rev. B **81**, 205114 (2010).

[64] D. N. Basov and A. V. Chubukov, Nat. Phys. **7**, 272 (2011).

[65] Z. P. Yin, K. Haule, and G. Kotliar, Nat. Phys. **7**, 294 (2011).

[66] M. M. Qazilbash, A. A. Schafgans, K. S. Burch, S. J. Yun, B. G. Chae, B. J. Kim, H. T. Kim, and D. N. Basov, Phys. Rev. B **77**, 115121 (2008).

[67] M. K. Stewart, *et. al.*, Phys. Rev. B **83**, 075125 (2011).

[68] W. L. Yang, *et. al.*, Phys. Rev. B **80**, 014508 (2009).

[69] V. I. Anisimov, E. Z. Kurmaev, A. Moewes, I. A. Izyumov, Physica C **469**, 442 (2009).

[70] S. Zhou and Z. Wang, Phys Rev. Lett. **105**, 096401 (2010).

[71] A. Kutepov, K. Haule, S. Y. Savrasov, and G. Kotliar, Phys. Rev. B **82**, 045105 (2010).

[72] Rong Yu, K. T. Trinh, A. Moreo, M. Daghofer, J. A. Riera, S. Haas, and E. Dagotto, Phys. Rev. B **79**, 104510 (2009).

[73] Q. Luo, G. Martins, D.-X. Yao. M. Daghofer, R. Yu, A. Moreo, and E. Dagotto, Phys. Rev. B **82**, 104508 (2010).

[74] The relevant energy scale for semimetals may be $U/2$ (see Ref. (75)), which is still greater than the observed energy scale of SW transfer.

[75] G. Kotliar and D. Vollhardt, Physics Today **57**, March, 53 (2004).

[76] As temperature is decreased in the high-temperature metallic phase of V_2O_3, SW moves from high to low energy into the Drude response, over an energy scale associated with the Hubbard U. Upon entrance into the insulating phase at low temperatures, the Drude response disappears and the associated SW moves from low to high energy.

[77] D. Nicoletti, P. Di Pietro, O. Limaj, P. Calvani, U. Schade, S. Ono, Yoichi Ando, and S. Lupi, Cond. Mat. arXiv:1101.0745.

[78] M. Ortolani, P. Calvani, and S. Lupi, Phys. Rev. Lett. **94**, 067002 (2005).

[79] H. J. A. Molegraaf, C. Presura, D. van der Marel, P. H. Kes, and M. Li, Science **295**, 2239 (2002).

[80] A. F. Santander-Syro, R. P. S. M. Lobo, N. Bontemps, Z. Konstantinovic, Z. Li, and H. Raffy, Phys. Rev. Lett. **88**, 097005 (2002).

[81] D. Wu, G. Chanda, H. S. Jeevan, P. Gegenwart, and M. Dressel, Phys. Rev. B **83**, 100503(R) (2011).

[82] N. Barišić, D. Wu, L. J. Li, G. H. Cao, Z. A. Xu, and M. Dressel, Phys. Rev. B **82**, 054518 (2010).

[83] S. J. Moon, A. A. Schafgans, S. Kasahara, Y. Matsuda, M. A. Tanatar, R. Prozorov, A. Sefat, D. Mandrus, and D. N. Basov, Unpublished.

[84] A. Dusza, A. Lucarelli, F. Pfuner, J.-H. Chu, I. R. Fisher, and L. Digiorgi, Cond. Mat. arXiv:1007.2543

[85] J.-H. Chu, J. G. Analytis, K. De Greve, P. L. McMahon, Z. Islam, Y. Yamamoto, and I. R. Fisher, Science **329**, 824 (2010).

[86] N. L. Wang, W. Z. Hu, Z. G. Chen, R. H. Yuan, G. Li, G. F. Chen, and T. Xiang, Cond. Mat. arXiv:1105.3939.

[87] F. Ning, K. Anilan, T. Imai, A. S. Sefat, R. Jin, M. A. McGuire, B. C. Sales, and D. Mandrus, J. Phys. Soc. Jpn. **78**, 013711 (2009).

[88] A. S. Sefat, R. Jin, M. A. McMguire, B. C. Sales, D. J. Singh, and D. Mandrus, Phys. Rev. Lett. **101**, 117004 (2008).

[89] A. S. Sefat, M. A. McGuire, R. Jin, B. C. Sales, D. Mandrus, F. Ronning, E. D. Bauer, and Y. Mozharivskyj, Phys. Rev. B **79**, 094508 (2009).

[90] C.C. Homes, M. Reedyk, D. A. Cradles, and T. Timusk, Appl. Opt. **32**, 2976 (1993).

[91] A.B. Kuzmenko, Rev. Sci. Instrum. **76**, 093108 (2005).

[92] M. M. Qazilbash, J. J. Hamlin, R. E. Baumbach, Lijun Zhang, D. J. Singh, M. B. Maple, and D. N. Basov, Nature Physics **5**, 647 (2009).

[93] Z. Q. Li, E. A. Henriksen, Z. Jiang, Z. Hao, M. C. Martin, P. Kim, H. L. Stormer, and D. N. Basov, Nat. Phys. **4**, 532 (2008).

[94] M. Nakajima, *et. al.*, Phys. Rev. B **81**, 104528 (2010).

[95] Y. Onose, Y. Taguchi, K. Ishizaka, and Y. Tokura, Phys. Rev. B **69**, 024504 (2004).

[96] A. Zimmers, *et. al.*, Europhys. Lett. **70**, 225 (2005).

[97] N. Bontemps, R. P. S. M. Lobo, A. F. Santander-Syro, and A. Zimmers, Annals of Physics **321**, 1547 (2006).

[98] F. Carbone, A. B. Kuzmenko, H. J. A. Molegraaf, E. van Heumen, E. Giannini, and D. van der Marel, Phys. Rev. B **74**, 024502 (2006).

[99] F. Carbone, *et. al.*, Phys. Rev. B **74**, 064510 (2006).

[100] K. Takenaka, J. Nohara, R. Shiozaki, and S. Sugai, Phys. Rev. B **68**, 134501 (2003).

[101] E. van Heumen, *et. al.*, Phys. Rev. B **75**, 054522 (2007).

[102] H. Ding, *et. al.*, J. Phys.: Condens. Matter **23**, 135701 (2011).

[103] M. Yi., *et. al.*, Phys. Rev. B **80**, 024515 (2009).

[104] M. Yi, *et. al.*, Phys. Rev. B **80**, 174510 (2009).

[105] W. Prestel, *et. al.*, Eur. Phys. J. Special Topics **188**, 163 (2010).

[106] J. J. Tu, J. Li, W. Liu, A. Punnoose, Y. Gong, Y. H. Ren, L. J. Li, G. H. Cao, Z. A. Xu, and C. C. Homes, Phys. Rev. B **82**, 174509 (2010).

[107] L. Fang, *et. al.*, Phys. Rev. B **80**, 140508(R) (2009).

[108] D. Wu, *et. al.*, Phys. Rev. B **81**, 100512R (2010).

[109] Taichi Terashima, *et. al.*, Cond-Mat arXiv:1103.3329

[110] D. N. Basov, Richard D. Averitt, Dirk van der Marel, Martin Dressel, and Kristjan Haule, Rev. Mod. Phys. **83**, 471 (2011).

[111] A. Akrap, J. J. Tu, L. J. Li, G. H. Cau, Z. A. Xu, and C. C. Homes, Phys. Rev. B **80**, 180502(R) (2009).

[112] T. Dong, Z. G. Chen, R. H. Yuan, B. F. Hu, B. Cheng, and N. L. Wang, Phys. Rev. B **82**, 054522 (2010).

[113] C. Martini, C. Mirri, G. Profeta, S. Lupi, D. Di Castro, R. Sopracase, P. Postorino, P. Calvani, A. Perucchi, S. Massidda, G. M. Tropeano, M. Putti, A. Martinelli, A. Palenzona, and P. Dore, Europhys. Lett. **84**, 67013 (2008).

[114] D. Wu, N. Barišić, N. Drichko, S. Kaiser, A. Faridian, M. Dressel, S. Jiang, Z. Ren, L. J. Li, G. H. Cao, Z. A. Xu, H. S. Jeevan, and P. Gegenwart, Phys. Rev. B **79**, 155103 (2009).

[115] A.P. Litvinchuk, V. G. Hadjiev, M. N. Iliev, Bing Lv, A. M. Guloy, and C. W. Chu, Phys. Rev. B **78**, 060503(R) (2008).

[116] R. Mittal, S. Rols, M. Zbiri, Y. Su, H. Schober, S. L. Chaplot, M. Johnson, M. Tegel, T. Chatterji, S. Matsuishi, H. Hosono, D. Johrendt, and Th. Brueckel, Phys. Rev. B **79**, 144516 (2009).

[117] W. Z. Hu, Q. M. Zhang, and N. L. Wang, Physica C **469**, 545 (2009).

[118] R. Mittal, Y. Su, S. Rols T. Chatterji, S. L. Chaplot, H. Schober, M. Rotter, D. Johrendt, and Th. Brueckel, Phys. Rev. B **78**, 104514 (2008).

[119] L. Chauvière, Y. Gallais, M. Cazayous, A. Sacuto, and M. A. Méasson, Phys. Rev. B **80**, 094504 (2009).

[120] Marianne Rotter, Marcus Tegel, and Dirk Johrendt, Phys. Rev. B **78**, 020503(R) (2008).

[121] V.G. Hadjiev, M. N. Iliev, K. Sasmal, Y.-Y. Sun, and C. W. Chu, Phys. Rev. B **77**, 220505 (2008).

[122] M. Kofu, Y. Qiu, Wei Bao, S.-H. Lee, S. Chang, T. Wu, G. Wu, and X. H. Chen, New J. Phys. **11**, 055001 (2009).

[123] U. Fano, Phys. Rev. **124**, 1866 (1961).

[124] A. B. Kuzmenko, L. Benfatto, E. Cappelluti, I. Crassee, D. van der Marel, P. Blake, K. S. Novoselov, and A. K. Geim, Phys. Rev. Lett. **103**, 116804 (2009).

[125] A. A. Schafgans, S. J. Moon, B. C. Pursley, A. D. LaForge, M. M. Qazilbash, A. S. Sefat, D. Mandrus, K. Haule, G. Kotliar, and D. N. Basov, Cond. Mat. arXiv:1106.3114

[126] N. L. Wang, W. Z. Hu, Z. G. Chen, R. H. Yuan, G. Li, G. F. Chen, and T. Xiang, Cond. Mat. arXiv:1105.3939

[127] A. Dusza, A. Lucarelli, F. Pfuner, J.-H. Chu, I. R. Fisher, L. Degiorgi, Cond. Mat. arXiv:1007.2543

[128] M. Nakajima, T. Liang, S. Ishida, Y. Tomioka, K. Kihou, C. H. Lee, A. Iyo, H. Eisaki, T. Kakeshita, T. Ito, and S. Uchida, Cond. Mat. arXiv:1106.4967

[129] J. K. Galt, W. A. Yager, F. R. Merritt, B. B. Cetlin, and A. D. Brailsford, Phys. Rev. **114**, 1396 (1959).

[130] J. Heremans, D. L. Partin, C. M. Thrush, G. Karczewski, M. S. Richardson, and J. K. Furdyna, Phys. Rev. B **48**, 11329 (1993).

[131] B. Lenoir, M. Cassart, J.-P. Michenaud, H. Scherrer, and S. Scherrer, J. Phys. Chem. Solids **57**, 89 (1996).

[132] D. Hsieh, Y. Xia, L. Wray, D. Qian, J. H. Dil, F. Meier, L. Patthey, J. Osterwalder, G. Bihlmayer, Y. S. Hor, R. J. Cava, and M. Z. Hasan, Cond. Mat. arXiv:1103.3413

[133] L. Fu, and C. L. Kane, Phys. Rev. B **76**, 045302 (2007).

[134] M. Z. Hasan and C. L. Kane, Rev. Mod. Phys. **82**, 3045 (2010).

[135] Liang Fu, C. L. Kane, and E. J. Mele, Phys. Rev. Lett. **98**, 106803 (2007).

[136] Jeffrey C. Y. Teo, Liang Fu, and C. L. Kane, Phys. Rev. B. **78**, 045426 (2008).

[137] Xiao-Liang Qi, T. L. Hughes, and Shou-Cheng Zhang, Phys. Rev. B **78**, 195424 (2008).

[138] D. Hsieh, D. Qian, L. Wray, Y. Xia, Y. S. Hor, R. J. Cava, and M. Z. Hasan, Nature **452**, 970 (2008).

[139] D. Hsieh, Y. Xia, L. Wray, D. Qian, A. Pal, J. H. Dil, J. Osterwalder, F. Meier, G. Bihlmayer, C. L. Kane, Y. S. Hor, R. J. Cava, and M. Z. Hasan, Science **323**, 919 (2009).

[140] A. Nishide, A. A. Taskin, Y. Takeichi, T. Okuda, A. Kakizaki, T. Hirahara, K. Nakatsuji, F. Komori, Yoichi Ando, and I. Matsuda, Phys. Rev. B **81**, 041309(R) (2010).

[141] P. Roushan, J. Seo, C. V. Parker, Y. S. Hor, D. Hsieh, D. Qian, A. Richardella, M. Z. Hasan, R. J. Cava, and A. Yazdani, Nature **460**, 1106 (2009).

[142] Guohong Li and Eva Y. Andrei, Nat. Phys **3**, 623 (2007).

[143] I. Crassee, J. Levallois, A. L. Walter, M. Ostler, A. Bostwick, E. Rotenberg, T. Seyller, D. van der Marel, and A. B. Kuzmenko, Nat. Phys. **7**, 48 (2010).

[144] A. A. Taskin and Yoichi Ando, Phys. Rev. B **80**, 085303 (2009).

[145] Martin Maltz and M. S. Dresselhaus, Phys. Rev. B **2**, 2877 (1970).

[146] A. A. Taskin, Kouji Segawa, and Yoichi Ando, Phys. Rev. B **82**, 121302(R) (2010).

[147] A. A. Taskin, Kouji Segawa, and Yoichi Ando, arXiv:1009.4005

[148] A. D. LaForge, A. Frenzel, B. C. Pursley, Tao Lin, Xinfei Liu, Jing Shi, and D. N. Basov, Phys. Rev. B **81**, 125120 (2010).

[149] M. Wanner, R. E. Doezema, and U. Strom, Phys. Rev. B **12**, 2883 (1975).

[150] P. A. Wolff, J. Phys. Chem. Solids **25**, 1057 (1964).

[151] R. N. Brown, J. G. Mavroides, M. S. Dresselhaus, and B. Lax, Phys. Rev. Lett. **5**, 243 (1960).

[152] M. P. Vecchi, J. R. Pereira, and M. S. Dresselhaus, Phys. Rev. B **14**, 298 (1976).

[153] E. D. Palik and J. K. Furdyna, Rep. Prog. Phys. **33**, 1193 (1970).

[154] L. C. Hebel and G. E. Smith, Phys. Lett **10**, 273 (1964).

[155] Z. Jiang, E. A. Henriksen, L. C. Tung, Y.-J. Wang, M. E. Schwartz, M. Y. Han, P. Kim, H. L. Stormer, Phys. Rev. Lett. **98**, 197403 (2007).

[156] V. P. Gusynin, S. G. Sharapov, J. P. Carbotte, Phys. Rev. Lett. **98**, 157402 (2007).

[157] Haijun Zhang, Chao-Xing Liu, Xiao-Liang Qi, Xi Dai, Zhong Fang, and Shou-Cheng Zhang, Nat. Phys. **5**, 438 (2009).

[158] Chao-Xign Liu, Xiao-Liang Qi, HaiJun Zhang, Xi Dai, Zhong Fang, and Shou-Cheng Zhang, Phys. Rev. B 82, 045122 (2010)

[159] T. Hanaguri, K. Igarashi, M. Kawamura, H. Takagi, and T. Sasagawa, Phys. Rev. B **82**, 081305(R) (2010).

[160] Yi-Han Kao, Phys. Rev. **129**, 122 (1963).

[161] A. A. Taskin and Yoichi Ando, Phys. Rev. B **80**, 085303 (2009).

[162] Xiao-Liang Qi, Rundong Li, Jiadong Zang, and Shou-Cheng Zhang, Science **323**, 1184 (2009).

[163] Wang-Kong Tse and A. H. MacDonald, Phys. Rev. Lett. **105**, 057401 (2010).